Study on semiconductor material silicon for photovoltaic application using hot wire chemical vapor deposition techniques

Ph. D. Thesis by

Md Abul Hossion

(Registration No 08/2011-2012)

In Partial Fulfilment of the Requirement

for the Degree of

Doctor of Philosophy

Under the supervision of

Professor Dr Zahid Hasan Mahmood

Electrical and Electronic Engineering
University of Dhaka, Dhaka, Bangladesh
2017

Originality Statement

I hereby declare that this submission is the own work of Md Abul Hossion and to the best of my knowledge it contains no materials previously published or written by another person, or substantial proportions of material which have been accepted for the award of any other degree or diploma at the University of Dhaka or any educational institution, except where due acknowledgement is made in the thesis. Any contribution made to the research by others, with whom Mr Hossion has worked at University of Dhaka or elsewhere, is explicitly acknowledged in the thesis. I also declare that intellectual content of this thesis is the product of Mr Hossion's research work, except to the extent that assistance from others is acknowledged.

Professor Dr. Zahid Hasan Mahmood
MPhil (Nottingham), PhD (Dhaka), AMIEE, GradInstP
Department of Electrical and Electronic Engineering
Director
Center for Research on Semiconductor Technology
Adjunct Faculty
Department of Nuclear Engineering
University of Dhaka, Bangladesh.
Former Visiting Professor and Visiting Scientist
Department of Condensed Matter Physics and Material Science
Tata Institute of Fundamental Research, Mumbai, India.

Course Work

Course work completed by Md Abul Hossion, offered by the Department of Electrical and Electronic Engineering for the partial fulfilment of the Ph.D. degree.

Course code	Course name	Total Marks Offered	Total Marks Obtained	Result
EEE-503	Biomedical signal analysis and imaging	200	210	Passed
EEE-504	Electronic material			
EEE-510	Semiconductor characterization			
Viva-voce		100		

Professor Dr. Zahid Hasan Mahmood
MPhil (Nottingham), PhD (Dhaka), AMIEE, GradInstP
Department of Electrical and Electronic Engineering
Director
Center for Research on Semiconductor Technology
Adjunct Faculty
Department of Nuclear Engineering
University of Dhaka, Bangladesh.
Former Visiting Professor and Visiting Scientist
Department of Condensed Matter Physics and Material Science
Tata Institute of Fundamental Research, Mumbai, India.

Acknowledgements

This entire research work has been carried out in the Department of Electrical Engineering, Indian Institute of Technology Bombay (IITB), Mumbai, India, during the period of January 2013 to January 2015 as a 'Visiting International Ph.D. Student'. I would like to thank Emeritus Fellow, Professor Juzer M. Vasi and Dean International Relation, Professor Subhasis Chaudhuri for their direct effort in my admission at IITB.

I wish to express my deepest gratitude towards my guide, Prof Dr Zahid Hasan Mahmood. I thank him for giving me the opportunity to work under his supervision. He has been a wonderful and a caring supervisor. He helped me keep my perspective and focus over those years. He has been a constant source of ideas and technical guidance during the entire time of my research work. I still remember those early days when we travelled together to IIT Guwahati, IIT Bombay, Calcutta University, Jadavpur University, Tata institute of Fundamental Research as a visitor. This was his vision that today I became a scientist. He has been always kind to me in writing recommendation letters regarding my admission in IITB, Mumbai, India as a visiting international student. Without support from Prof Zahid, my venture into the world of research would not have been possible.

This research work would not have been possible without the financial support. I would like to thank Ministry of Science and Technology, Bangladesh, for their fellowship through the project 'Bangabandhu fellowship on science and information communication technology'.

Acknowledgements

Finally I have made myself worthy enough to become a real scientist. My success in this endeavour is largely a result of being lucky enough to meet the right people. I hope I have made their contributions to a success.

For direct contribution to the content of this thesis, I am thankful to Prof K.L. Narasiman for discussions and suggestions during the entire work. I thank Dr Sudip Dev for his valuable suggestion in explaining Raman spectrum and image analysis. I thank Prof. Dr Harindranath, who allowed me to use TOF-SIMS for a greater extended period, not only this but he also allowed me to present the findings in a weekly meeting. My gratitude is also to Prof. P. Apte, who taught me the finer aspects of a PhD program. I also thank Prof. R.O. Dusane for allowing me to use Hotwire CVD tool for fabrication of n-type silicon film. Let me also thank Prof. I. Samajdar for allowing me to use X-ray diffraction tool for the characterization of thin silicon film which took 12 hours for a single operation. We usually load four samples at a time and continue the scan at 0.5° grazing angle. Prof Samajdar was really kind to allow such longer occupation of the XRD tool. I would like to thank Prof Arnab for allowing me to use Raman imaging tool. I am thankful to Ranga Rao Arnepalli from AMAT lab. He was really kind enough to allow me to use general purpose glove box for spin-on phosphorous dopant.

I am grateful to a number of PhD students who assisted me in several phases of the work. In particular, thanks to Sanchit Khatavkar for introducing me with the HWCVD cluster tool at CEN, Rajib Mahmood, who helped me get trained on AFM for 2D/3D imaging during nucleation stage of my work, Sanchar Acharya, Kalaivani S and Karthick Murukesan for SEM imaging, Som Mandal who performed all the optical characterization using UV-VIS-NIR spectrometer not only that he trained me with the laser doping tool for annealing of silicon film, thanks to Priyanka Das and Hites Kamble for training me on RTP furnace. I am grateful to Dharmendra who have taken X-TEM imaging with great care and expertise, thanks to Vishnu Kant Bajpai and Punam Murkute, a model of true kindness and patience with great experience for their help during long and complex X-TEM sample preparation. I am grateful to Subhash Lokhre and Nilesh Marle for their active participation during TOF-SIMS calibration and measurement process. I am also grateful to Carina Malikkal for her patient during Raman images. It took a whole day to complete those imaging and she was really kind to me for the whole time.

I am also thankful to all lab staff In particular, thanks to Anjum Ahmed, Raorane and Poonam Katkar for their active participation during HWCVD growth, Sunil Kale for his assistance during wet oxidation using oxidation furnace, Thankamani Nair for substrate cleaning, and chemical etching, Hemlata Tiwari for HRXRD measurement, Darshan Thakare for spin phosphorous dopant inside glove box, Thirumala Narukuti for FEGSEM imaging, Kulasekaran Muniappan for Photoluminescence and photocurrent spectral response measurement, Gurappa Burkul for optical measurement using UV-VIS-NIR spectrometer.

We are thankful to a numbers of labs where we have performed the research work. We are grateful to the Department of metallurgical engineering & material science for XRD imaging and HWCVD tool. We are thankful to centre of excellence in nanofabrication (CEN), national centre of photovoltaic research and education (NCPRE), sophisticated analytical instrument facility (SAIF), centre for research in nanotechnology & science (CRNTS), and Tata institute of fundamental research (TIFR) for allowing us to use their research facility.

Even before my visit to IITB, I was fortunate to have a great number of fantastic mentors. Mahbubul Hoq, Anzan-Uz-Zaman, and Nasrul Hoque at Institute of Electronics, Atomic Energy Research Establishment, first introduced me to their VLSI clean room facility. I am incredibly glad that I had the luxury to spend more than a year in that facility with them around. They served as great source of advice and inspiration. I must acknowledge the effort of Nahid Akhter, Ph.D. student of my supervisor. She was always available to assist me during my work at VLSI lab. I am also grateful to Centre for Research on Semiconductor Technology.

Finally and most importantly, I would like to thank my entire extended family. My parents, Abul Quashem and Akhter Jahan, have always been a source of encouragement, support and love. My brothers, Delowar Hossain and Kamrul Hasan, have always been a source of encouragement, not to mention borrowing money from them for years during my staying at IITB. My wife, Kaysari Afroz, she fostered my sense of social responsibility for the first time in my life. When I left for IITB just after six month of our marriage leaving her behind in my home, she was strong enough to bear that lonely time without my presence. I have enjoyed the evening online video chat on Skype with her along with my parents during my stay at IITB. They definitely help me remember what is important in life. Thanks.

Abstract

Large grain polycrystalline silicon thin film on low cost and robust substrate is an interesting area of research for photovoltaic devices. This film can be used to fabricate solar cell which has a potential to achieve 20% efficiency like multi crystalline silicon solar cell with the advantage of thin film fabrication techniques. In this thesis we have investigated the possibility of growing large grain (220) oriented poly crystalline silicon films, 2 to 3 micron thick, from silane-hydrogen mixture, by hot wire chemical vapour deposition (HWCVD). Several substrates i) Si/SiO_2, ii) TiO_2 layer on glass, iii) textured nickel-5% tungsten metal strip, iv) crystalline sapphire and v) alkali free borosilicate glass have been used in this work.

The growth of intrinsic poly crystalline silicon film was performed starting with a thin nucleation layer at 400°C followed by the thickening stage at 600°C with higher silane concentration. We have optimized the growth conditions and one micron of well passivated hydrogenated (220) oriented polycrystalline film were grown successfully. We have used several characterization techniques for the evaluation of the optical, topographical and electrical properties of the film.

The growth of boron doped poly crystalline and amorphous silicon film was also performed following by process similar to that used for intrinsic poly silicon film using HWCVD with the addition of diborane to the gas mixture for boron doping the silicon.

The HWCVD system used for the synthesis of intrinsic and p-type polycrystalline silicon films did not have provision for n-type doping. For synthesis of phosphorous doped n-type silicon film, we initially explored doping intrinsic polycrystalline silicon film by using two different sources of phosphorous followed by Laser annealing. One approach used i) spin-on phosphorous dopant film about one micron thick and the other approach used ii) phosphorous ion implantation.

For both these approaches, we have investigated the possibility of dopant activation by irradiation with infrared continuous wave laser which can uniformly scan the sample along X-Y directions. Laser annealing is performed varying the laser power and scan speed to ensure suitable laser annealing condition. Sheet resistivity measurement was carried out to verify the laser annealing process. In this case the several characterization techniques were also followed for the evaluation of the optical, topographical and electrical properties of the

film. However, the n-type silicon films synthesised in this manner were not device quality. At this stage, we got access to another HWCVD reactor equipped with synthesis of n-type silicon using phosphine as the dopant gas.

After the above growth experiments, we took initiative to stack all these silicon layers in order to apply them in photovoltaic application. In this case we have fabricated an n-i-p structure on glass using two different HWCVD systems, starting with synthesis n-type silicon on glass in one reactor. This was transferred to the second HWCVD reactor for the synthesis of intrinsic polycrystalline silicon film. After this, a combination of a thin layer of amorphous intrinsic silicon followed by p-type amorphous silicon film was deposited to form a hetero junction between the intrinsic polycrystalline silicon and p-type amorphous silicon layer. The structure is well known as heterojunction with intrinsic thin layer (HIT). In our case the intrinsic polycrystalline silicon layer acts as the light absorber layer, the top p-type amorphous silicon acts as emitter layer, while the bottom n-type silicon acts as back surface field. The performance of the device was evaluated from dark and illuminated I-V characterization. It was observed that the light response was very weak. Further work is necessary to improve the photovoltaic action. For this, we have to increase the thickness and material quality of the light absorbing layer, and improve the quality of junctions.

Contents

List of Journal publication:

1. Abu Kowsar, **Md Abul Hossion**, Md Sofikul Islam and Zahid Hasan Mahmood, Analysis of theoretical efficiencies of $GaInP_2$/GaAs/Ge multijunction solar cell, Dhaka Univ. J. App. Sci. Eng. July 2012.

2. M. A. Zaman, **M. A. Hossion**, M. Hoq and M. N. H. Mia, Wet etching on GaAs wafer at institute of electronics clean room facility, Int. j. eng. technol. (Online) Volume 2 Issue 1, 01-03, January 2014.
Onlinelink: http://gscience.gurpukur.com/our-journal/ijet-online/volume-2-2014/volume-2-issue-1-january-014/page-01-03-wet-etching-on-gaas-wafer-at-institute-of-electronics-clean-room-facility.html

3. Nahid Akter, **Md. Abul Hossion**, Mahbubul Hoq , Sardar Masud Rana, Md Anzan-Uz-Zaman, Md. Nasrul Haque Mia, Md. Alamgir Kabir, Zahid Hasan mahmood, Electrical Characterization and Doping Uniformity Measurement during Crystalline Silicon Solar Cell Fabrication Using Hot Probe Method, Engineering International (Multidisciplinary International Referred Journal), Vol 2, No 1/2014 (3^{rd} issue)
Online Link: http://www.j-ei.us/current-issue.html

4. Nahid Akter, Sajia Afrin, **Md Abul Hossion**, Md. Alamgir Kabir, Shirin Akter, Zahid Hasan Mahmood, Evaluation of majority charge carrier and impurity concentration using hot probe method for mono crystalline silicon (100) wafer, Int. J. Advances in Materials Science and Engineering (IJAMSE), Vol.4, No.4, October 2015.

List of paper published on IEEE Digital Library (Online):

1. **Md Abul Hossion**, Brij Mohan Arora, Optical characterization of Intrinsic Poly Silicon Film for Photovoltaic Application on Sapphire and TiO_2 Substrate by HWCVD, 1st International Conference on Electrical Engineering & Information Technology , Military Institute of Science and Technology, 2014, Dhaka, Bangladesh.

Online Link: http://ieeexplore.ieee.org/xpl/articleDetails.jsp?arnumber=6919055

2. **Md Abul Hossion**, B. M. Arora, Structural characterization of oriented crystalline silicon film grown on SiO_2, Sapphire, TiO_2 and Nickel Substrate by Hot Wire Chemical Vapour Deposition, 40th Photovoltaic Specialists Conference, June 7 -13, 2014, Denver, Colorado, USA.

Online link: http://ieeexplore.ieee.org/xpl/articleDetails.jsp?arnumber=6925153

3. Gurleen Kaur, **Md Abul Hossion**, Kulasekaran M, Brij Mohan Arora, Synthesis of oriented and passivated polycrystalline silicon films on glass by hot wire chemical vapor deposition, 40th Photovoltaic Specialists Conference, June 7 -13, 2014, Denver, Colorado, USA.

Online Link: http://ieeexplore.ieee.org/xpl/articleDetails.jsp?arnumber=6925162

List of paper published on conference proceeding:

1. **Md Abul Hossion**, Abu Kowsar , Chandan Qumar Howlader, Zahid Hasan Mahmood, Performance analysis of super high efficiency three junction series connected tandem solar cell, International Conference on Fiber Optics & Photonics, 2011, IIT Guwahati, India.

2. **Md Abul Hossion**, Md Anzan-Uz-Zaman, Mahbubul Hoq, Md Al-Mamun, Zahid Hasan Mahmood, Study of wet etching on GaAs wafer at Institute of Electronics Clean Room facility, National Conference on Advances in Physics, 2012, SUST, Sylhet, Bangladesh.

3. Md.Anzan-Uz-Zaman, Md.Aliuzzaman, **Md. Abul Hossion**, Md. Nasrul Haque Mia, Md. Shah Alam, Himangshu Kumar Ghos, Calibration of Spectroscopic Reflectometer for Thin Film Characterization, International Conference on Electrical, Computer and Telecommunication Engineering, RUET, Rajshahi, 2012, Bangladesh.

List of manuscripts under preparation:

1. **Md Abul Hossion**, Zahid Hasan Mahmood, B. M. Arora 'Cross sectional TEM characterization of poly-silicon grown using hot wire chemical vapor deposition for photovoltaic application'.

2**. Md Abul Hossion**, Som Mondol, Zahid Hasan Mahmood, B. M. Arora, 'Phosphorus dopant diffusion and activation using continuous wave infrared laser for synthesis of n-type silicon thin film'.

3. **Md Abul Hossion**, Zahid Hasan Mahmood, Brij Mohan Arora, 'Phosphorous and boron concentration analysis of silicon film for photovoltaic application using time of flight secondary ion mass spectroscopy'.

4. **Md Abul Hossion**, Carina B Maliakkal, Zahid Hasan Mahmood, Brij Mohan Arora, 'Contact less characterization of laser annealed n-type silicon film on glass using confocal Raman imaging'.

List of Figures

Chapter 4 **(Page 75-108)**

Figure 5.3: SEM image of sample 99_FTO/Glass boron doped p-type amorphous silicon film grown on polycrystalline on glass substrate. Magnification a) 100 KX b) 200 KX.

Figure 5.4: Stylus surface profiler step height measurement of p-type polycrystalline silicon thick film on Glass/TiO_2 substrate.

Figure 5.5 Cross section transmission electron microscope image of 39_Si/SiO_2 i) complete structure ii) Top amorphous layers.

Figure 5.6 Cross section transmission electron microscope image of 96_Si/SiO_2 i) complete structure ii) Top amorphous layers.

Figure 5.7: Reflectance spectrum under UV-VIS-NIR range using integrating sphere method of boron doped p-type silicon thin film on a) 26_ Ni-W b) 25_ Glass/TiO_2 c) 24_ Al_2O_3 (d) 18_Si/SiO_2 substrates

Figure 5.8: Reflectance spectrum of boron doped p-type silicon thick film under UV-VIS-NIR range using integrating sphere method on a) 30_ Al_2O_3 b) 29_ Ni-W c) 27_ Glass/TiO_2 (d) 2_Si/SiO_2 substrates.

Figure 5.9: Transmission spectrum of boron doped p-type silicon thin film on b) 25_ Glass/TiO_2 and d) 24_ Al_2O_3 substrate; thick film on a) 27_ Glass/TiO_2 and c) 30_ Al_2O_3 substrates under UV-VIS-NIR range using integrating sphere method.

Figure 5.10: X-ray diffraction spectrum of boron doped p-type silicon thin poly crystalline film on a) 26_Ni-W b) 25_ Glass/TiO_2 c) 20_Sapphire (Al_2O_3) and d) 18_SiO_2 substrate

Figure 5.11: X-ray diffraction spectrum of thick poly crystalline silicon film on a) 29_Ni-W b) 27_ Glass/TiO_2 c) 30_Sapphire (Al_2O_3) and d) 2_Si/SiO_2 substrate

Figure 5.12: Concentration – depth curve of a) boron doped amorphous silicon film on intrinsic poly silicon film, b) standard boron doped p-type silicon sample prepared by boron diffusion furnace at 1000°C for 20 min.

Figure 5.13: FTIR absorption spectrum of boron doped p-type silicon film on a) 2_Si/SiO_2 b) 30_Al_2O_3 c) 24_Al_2O_3 substrates. FTIR transmission spectrum of boron doped poly silicon film on d) SiO_2 substrate.

Figure 5.14: 20keV EDX spectrum of boron doped p-type amorphous silicon on FTO coated glass. Inset SEM image of area where EDX was performed.

Chapter 6 **(Page 129-157)**

List of Tables

List of instrument

Fabrication Tool		
Name of instrument	**Purpose**	**Name of lab***
2 inch wet oxidation furnace	Deposition of silicon dioxide layer	Micro 1, CEN, IITB
Hot wire chemical vapour deposition tool 1	Growth of intrinsic and p-type doped silicon film.	Micro 2, CEN, IITB
Hot wire chemical vapour deposition tool 2	Deposition of n-type silicon film	Semiconductor Thin Films and Plasma Processing Lab, MEMS, IITB
Thermal evaporator 1	Deposition of aluminium thin film	Micro 1, CEN, IITB
Thermal evaporator 2	Deposition of gold chromium thin film	Micro 1, CEN, IITB
Laser annealing tool	Laser annealing of silicon film	NCPRE Char Lab, IITB
Characterization Tool		
Ambios XP2 stylus surface profiler	Thickness measurement	2.1 PLD Clean room, CEN, IITB
DektakXT stylus surface profiler	Thickness measurement	Micro 2, CEN, IITB
Reflectometer	Thickness measurement	Micro 2, CEN, IITB
Atomic force microscope	Surface morphology	Micro 2, CEN, IITB
Scanning electron microscope & EDX	Surface morphology	NCPRE, IITB
Transmission electron microscope	Surface and structural analysis	SAIF, IITB
Zeta 3D optical microscope	Surface morphology after laser irradiation	NCPRE Char Lab, IITB
Olympus 2D optical microscope	Surface morphology after laser irradiation	Nano clean room, CEN, IITB
X-ray diffraction 1	Crystalline orientation of thin silicon film	National Facility, MME, IITB
X-ray diffraction 2	Crystalline orientation of thick silicon film	Solid state lab, TIFR,
High resolution X-ray diffraction	Crystalline orientation of thick silicon film on glass	Micro 1, CEN, IITB
Raman spectroscopy	Crystallinity	CRNTS, IITB
Confocal Raman imaging	Crystallinity	Optoelectronics lab, TIFR
Photoluminescence	Band gap	Micro 2, CEN, IITB
Furrier transform infrared spectrum	Infrared spectrum of silicon film	Bio sensor lab, CEN, IITB
Time of flight secondary ion mass spectrometry	Majority carrier concentration	SAIF, IITB
UV-VIS-NIR spectrometer	Optical response	NCPRE Char. Lab, IITB

Name of instrument	Purpose	Name of lab*
Four point probe	Measurement of sheet resistivity	NCPRE Char Lab, IITB
Temperature dependant I-V measurement setup	I-V data	Organic electronics lab, CEN, IITB
One sun illumination I-V setup	Illuminated I-V data	NCPRE Char Lab, IITB
Capacitance measurement setup	Measurements of capacitance of n-i-p diode	Organic electronics lab, IITB
Photo current measurement setup	Measurement of photocurrent	Applied quantum mechanics lab, IITB
Other Related Tool		
RCA cleaning setup	Cleaning of silicon wafer	Chemistry room, CEN, IITB
TMAH etching setup	Etching of silicon film	TCE lab, CEN, IITB
General stainless steel mask cleaning setup	Device fabrication	Chemistry room, CEN, IITB
General purpose hot plate	Heating, baking	Chemistry room, CEN, IITB
Spin coater	Spin PPR coating and phosphorous dopant	AMAT Lab, IITB
General purpose glove box	phosphorous dopant	AMAT Lab, IITB
General purpose electrical oven	Drying	AMAT Lab, IITB
Mask aligner	UV expose	Micro 1 Yellow room, CEN, IITB

*IITB = Indian Institute of Technology Bombay

*NCPRE =National Centre of Photovoltaic Research and Education

*CEN = Centre of Excellence in Nano Technology

*TIFR = Tata Institute of Fundamental Research

*SAIF = Sophisticated Analytical Instrument Facility

*CRNTS = Centre for Research in Nanotechnology & Science

*AMAT = Applied Material and Technology

*MEMS = Metallurgical Engineering and Material Science

Chapter 1

Introduction

1.1 Photovoltaic (PV) technology

1.1.1 Past and present

The study of photovoltaic (PV) effect began in 1839 when Edmund Becquerel discovered an increment in current of an electrolyte cell when exposed to light [1]. Photovoltaic effect in solid state was discovered first in selenium while investigating photoconductivity and attributed to energy barrier to current flow at metal semiconductor junction. The modern PV era began in 1953 at Bell laboratories where scientists Gerald Pearson, Daryl Chapin and Calvin Fuller fabricated the first solar cell using p-n junction in silicon [2]. As the cost of commercial solar cell was as high as 300USD per watt, it was not practical for mass production; however it proved useful for powering satellites proposed by Gordon Raisbeck one of Daryl Chapin's colleague in 1955 [3]. Despite the initial concern of photovoltaic's future, research continued and cost reduced to 100USD per watt by the year 1970 which was mainly used for powering satellites [4]. At present the production cost has reduced to 1 USD per watt peak for solar modules (≥ 125W) made of multi crystalline silicon [5]. Thus the number of terrestrial solar power units has increased dramatically in various fields of necessity such as signalling, communication and remote sensing, and even powering the water pumps in agricultural fields to the use of solar PV as energy source alternative to fossil fuels. Now a days about large percentage of the terrestrial photovoltaic solar cells are made of silicon [5].

With the reduction in production cost, the conversion efficiency becomes a real concern to the scientist. Mono crystalline silicon solar cell reached an efficiency of 24.5 % by University of New South Wales [6], commercial mono crystalline manufactured by SunPower achieved an efficiency of 20.4% [7]. Large grain polycrystalline silicon produced cheaply compared to mono crystalline silicon can have the properties close to mono crystalline silicon [8]. Commercial thick film polycrystalline silicon solar cell reached 17.7% efficiency manufactured by Kyocera [9]. Details about the efficiency of solar cells and modules are discussed in this chapter in the section 1.1.4.

1.1.2 Materials for Photovoltaics

Since only photons with energies above the band gap of a semiconductor are absorbed, the band gap of the material used for a photovoltaic device must be engineered in order to produce the maximum power for a given illumination, given that the solar spectrum as a function of photon energy under one sun condition [10,11]. Semiconductors with larger band gaps produce higher photovoltages, but absorb and convert fewer of the incident photons, resulting in lower currents. Semiconductors with smaller band gaps absorb most of the solar radiation, but convert most of the energy to heat. A balanced condition for the solar cell with the best efficiency is to use material with band gap near the peak of the solar spectrum, between 1 and 2 eV [12]. Compound semiconductors GaAs, GaInP, InP, CdTe, and CIS (copper indium diselenide), and indirect band gap materials, like silicon, are used in the fabrication of solar cells. Both amorphous and crystalline (polycrystalline and monocrystalline) silicon are used in the manufacture of photovoltaic devices. However, amorphous silicon suffers from the Staebler-Wronski effect [13], in which dangling bonds are created under illumination, causing the efficiency to degrade. Research communities turn then to crystalline silicon technology, which is capable of providing efficiencies greater than 20% [14].

1.1.3 Poly crystalline silicon technology

One of the most promising technologies for reduced cost photovoltaic technology involves the growth of thin film polycrystalline silicon on foreign substrates. Although the efficiencies of thin-film polycrystalline solar cells are lower than those of crystalline silicon cells, production costs are significantly lower. In 1996 Astropower Corporation produced the first commercially available polycrystalline silicon thin-film modules using a high-

temperature process on a foreign substrate [15]. Laboratory solar cell with an active layer of 50 μm thick was fabricated on a foreign substrate achieved an efficiency of 16.6% [16]. Fabrication of the polycrystalline silicon thin film on glass for photovoltaic application could be an innovative technology that combines the robustness of crystalline silicon wafer based technology with the advantage of thin film [17].

1.1.4 Efficiency of silicon solar cell

Since January 1993, Progress in Photovoltaics has published six monthly listings of the highest confirmed efficiencies for a range of photovoltaic cell and module technologies [18,19,20]. Here we have mentioned the results up to 2014 published in the solar cell efficiency table (version 44) [21]. Crystalline silicon on glass (CSG) solar cell achieved an efficiency of 10.5 % shown in table 1.1.

Table 1.1 Highest confirmed terrestrial solar cell efficiency measured under AM1.5 spectrum [21]

Classification of solar cell	Efficiency (%)	Description	References
Silicon (Crystalline)	25.6±0.5	Panasonic (HIT structure)	[22]
Silicon (Multi crystalline)	20.4±0.5	FhG-ISE	[23]
Silicon (amorphous)	10.1±0.3	Oerlikon Solar Lab, Neuchatel	[24]
Silicon (Micro crystalline)	11.0±0.3	AIST	[25]
Si (large multi crystalline)	19.5 ± 0.4	Q-Cells, laser-fired contacts	[26]
III-V GaAs Thin film	28.8±0.9	Alta device	[27]
CIGS thin film cell	20.5±0.6	Solibro, on glass	[28]
Dye sensitised cell	11.9±0.4	Sharp	[29]
Silicon (mini module)	10.5±0.3	CSG solar (<2μm on glass, 20 cells)	[30]

1.1.5 Technology of growth of PV material

Growth technology of solar cell material has improved significantly. Several low-temperature deposition methods for polycrystalline silicon have been studied, including the most widely used plasma enhanced chemical vapour deposition (PECVD) [31], very high frequency glow discharge (VHF-GD) [32], Electron Cyclotron Resonance CVD (ECR-CVD) [33] and Hot-Wire CVD (HWCVD) [34] which is the focus of our study. Furthermore, these kind of materials can also be synthesized by other techniques like rapid thermal annealing (RTA) [35], laser melt re-crystallisation (LMR) [36] and aluminium induced crystallisation [37].

1.2 Future of Photovoltaics with silicon

1.2.1 Heterojunction with intrinsic thin (HIT) layer solar cell

Hetero junction with intrinsic thin layer (HIT) silicon solar cells have reached photovoltaic efficiencies in excess of 22% reported by Sanyo Corp. Japan whereas world highest efficiency 25.6% reported by Panasonic shown in table 1.1. The Sanyo solar cell consists of a mono crystalline silicon (c-Si) wafer with thin layers of doped and undoped hydrogenated amorphous silicon (aSi:H) to form the junction. In the Sanyo HIT solar cell [38], an intrinsic thin layer is deposited between the wafer and the doped amorphous layer as back-surface field (BSF). For many years, and still as ongoing research, the optimisation of these structures has concentrated on the properties of the interface between the front amorphous hydrogenated silicon (a-Si:H) layers and the crystalline silicon (c-Si) wafer by plasma enhanced chemical vapour deposition (PECVD).

In addition, the back-contact properties have been investigated and improved. Because of the effect of the interface defects on the device properties, characterisation techniques are required not only for the fully processed cells but for the wafer structures with various deposited amorphous silicon layers. Recent research activities have in common that the characterisation of the passivated wafers has contributed to the solar cell optimisation. A summary of the results of the German project on both n and p type wafers can be found in [39]. In the French network [40] alternative thin layers of polymorphous silicon have been deposited to optimise the hetero junction cells, also in view of industrial processes. The focus of the hetero junction research at National Renewable Energy Laboratory (NREL) [41] is on alternative deposition techniques like hot-wire chemical vapour

deposition for the amorphous layers. In Neuchatel, very-high frequency PECVD has been applied to process hetero junction solar cells with high open-circuit voltages [42].

1.2.2 Application of Lasers in polycrystalline solar cell fabrication

Fabrication of polycrystalline silicon thin-film involves high-temperature processing such as crystallization, dopant diffusion and activation, and defect annealing. These processes require temperatures of more than 1000°C [43,44]. Poly-Si material is thermally stable and its electronic quality benefits from high temperature treatments. However, choosing glass as a substrate as low cost material cannot withstand high temperature for sufficiently long period. In this case lasers can deliver power sufficient to heat silicon films up to melting point while laser scanning speeds allow control of the exposure duration in the milliseconds range (1–100ms). In this range, the heat transfer is mostly confined to a thin film of few microns [45,46]. As a result, we can apply higher temperatures to silicon film while keeping the glass at a far lower temperature [47,48].

During the past few years we have seen an extensive use of rapid thermal processing (RTP) by means of halogen lamps on polycrystalline silicon materials to reduce the point defects present in the poly-Si layers and to activate the dopant elements [49,50,51,52]. However this method fails to achieve temperatures above 950°C for long time (>1 min) while keeping the borosilicate glass substrate intact. Using laser thermal annealing (LTA), it is possible to achieve very high temperature very close to the melting point of crystalline silicon for few seconds with minimal or negligible deformation of borosilicate glass substrate [53].

Lasers are being used for fabricating passivated emitter rare cell (PERC) solar cells of silicon. In this structure, instead of the regular silicon Al BSF cell where Al paste is screen printed directly on the back of the cell, in PERC cell one first deposits silicon nitride (SiN), drills holes in SiN by using a laser and then deposits Al. This cell has reached 20% efficiency [54].

In our study, we have used infrared lasers for the following processes, i) damage annealing and dopant activation in poly crystalline silicon layer implanted with phosphorous, ii) dopant diffusion into undoped poly crystalline silicon layer using spin-on dopant film, and iii) laser-induced liquid-phase crystallization of 100nm thin n-type silicon films to be used as a back surface field of n-i-p structure device.

1.2.3 Glass substrate for polycrystalline silicon solar cell

Thin-film technologies allow one to separate the electrically active and mechanically supportive material by depositing the active silicon thin film onto a low-cost substrate by means of several deposition processes mentioned in section 1.1.5. With this technology, the greatest reduction in cost is due to the reduction in silicon. Half of the costs associated with the traditional crystalline silicon solar cells, is due to the silicon wafer itself [54]. Scrap silicon from the semiconductor industry, the main source of silicon for the photovoltaic industry up until a few years ago, was available for $25/kg in 2003. But with demand increasing, the photovoltaic industry now pays for non-scrap silicon at $50/kg [55]. By depositing a thin-film of silicon on a low-cost substrate, one can decrease the material cost even further, and perhaps even take advantage of this step by depositing on building materials, such as window glass, roof top steel shed, to decrease installation and material costs.

There are several strategies to pursuing crystalline Si thin-films on glass substrates. One involves the crystallization of the entire amorphous silicon device by metal induced crystallization. With this technique, the metal reduces the energy and temperature necessary to crystallize the film. This method has been commercialized by crystalline silicon on glass (CSG) Solar cell production shown in Table 1.1. They have achieved small module efficiencies of 10.4 % for a 95 cm^2 module.

1.3 Review of Literature: HWCVD

1.3.1 HWCVD deposited solar cell

The low hydrogen content of device-quality hot wire-deposited amorphous silicon films makes them useful for inclusion in photovoltaics. In 1998, Bauer et al. at the University of Kaiserslautern recorded an initial efficiency of 10.4% using a p-i-n structure on a glass substrate with the i-layer deposited by HWCVD at low-temperature, although these cells degraded by approximately 30% when exposed to light [56]. In 2000, Kaiserslautern reported 8.0% efficiency using hot wire deposited p and n type layers on ITO-coated glass [57]. Nelson et al. at NREL have reported initial efficiencies of 5.7% with i-layers deposited at growth rates of 130˚A/s [58]. Microcrystalline silicon deposited by HWCVD has also shown promise as a material for solar cells. Meier et al. [59] at the University of Neuchatel have obtained 12% efficiency from a “micromorph” cell using tandem μc-Si:H-a-Si:H cells on ITO-coated glass substrates. The total device thickness is only 1.1 μm. Nikura et al. at Ecole Poly

technique report a 4.6% efficient cell with an n-i-p structure and a 2µm thick i-layer grown at 300°C [60]. Rath et al. have fabricated an HWCVD n-i-p cell with 3% efficiency [61].

1.3.2 Recent work using HWCVD

Most recent results of scientific research and process developments as well as new applications in the field of hot-wire activated chemical vapour deposition (HWCVD) are presented in the international HWCVD conference, held in October, 2014, Germany hosted by Fraunhofer Institute for Surface Engineering and Thin Films (IST) [62]. The recent research using HWCVD techniques are summarised as below. Industrialization of HWCVD for thin film application [63], low temperature impurity doping [64], deposition of low temperature SiO_2 film [65], n-type crystalline silicon hetero junction solar cell [66], polycrystalline silicon thin film with hydrogen for photovoltaic application [67], material development in solar energy research [68] and single junction solar cell on nano imprinted paper [69] are the most recent research related to silicon film technology for photovoltaic applications. Thus HWCVD provides a huge opportunity for the researchers to develop low cost and robust material for thin film as well as photovoltaic applications.

1.4 Objectives

The objective of this work is to explore the possibilities of HWCVD process for the growth of polycrystalline silicon films for photovoltaic application on a cheap amorphous substrate such as glass. We therefore optimized a multi chamber HWCVD system for the growth process of intrinsic silicon film. Next, we investigate the possibilities of growing boron doped polycrystalline and amorphous silicon film along with phosphorous doped microcrystalline silicon film using HWCVD system for photovoltaic application. Further, the objective of this work is to establish a basic framework for a device quality n-i-p structure once the optimizations of individual layers are performed.

1.5 Outlook of the thesis

This thesis is organized first with a brief introduction into the photovoltaics history, its market potential, the route for thin-film silicon solar cells, and the current status of large-grained polycrystalline film in photovoltaic industry. Future of silicon solar cell technology using hetero junction with intrinsic thin layer, laser annealing for defect passivation and silicon on low cost substrate are also discussed in brief.

Chapter 2 is a summary of hot-wire chemical vapour deposition (HWCVD) instrument setup, including the growth condition optimization for the silicon film using HWCVD. Advantages and disadvantages of using this technique are also discussed. Chapter 3 is a summary of theory and instrumentation techniques of characterization tools.

We can divide the thesis into four main chapters, covering growth and characterization of i) Intrinsic film in chapter 4, ii) boron doped p-type silicon film in chapter 5, iii) n-type silicon film in chapter 6 and iv) n-i-p diode structure in chapter 7. Chapter 4 follows with the synthesis of intrinsic large grain poly crystalline silicon film under hydrogen dilution on different substrate such as glass, nickel, titanium dioxide coated glass etc.

The characterization of the silicon films are then discussed by looking at the unique surface morphology, structural evolution, optical spectral response, electrical analysis and crystalline orientation of these films. Chapter 5 covers the synthesis of p-type boron doped silicon film followed by morphological, structural, electrical and optical characterization. Chapter 6 covers the synthesis of n-type phosphorous doped silicon thin film on glass substrate. In this chapter we have introduced three different source of phosphorous. Laser irradiation for dopant activation and defect annealing also implemented including detailed characterization of these films. Chapter 7 discusses the fabrication of n-i-p device structure using HWCVD followed by electrical results analysis of the device. Future research directions that would take advantage of the unique film morphologies and structures, along with a brief conclusion of this thesis are in Chapter 8. In the appendix part we have given the necessary images of fabrication and characterization tool. Detail steps and procedure of substrate cleaning, chemical etching of silicon, mask plate cleaning are discussed. In an extended part we have also given the detail route for preparation of silicon sample for cross section transmission electron microscope imaging.

1.6 Reference

[1] E. Becquerel. Comptes Rendues, 9:561, 1839.

[2] D. M. Chapin, C. S. Fuller, and G. L. Pearson. J. Appl. Phys., 25:676, 1954

[3] G. Raisbeck. Scientific American, 193:102, 1955.

[4] John Perlin. From Space to Earth: The Story of Solar Electricity. Harvard University Press, 1999.

[5] www. solarbuzz.com /facts-and-figures/ retail-price-environment/module-prices

[6] J. Zhao, A. Wang, P. Altermatt, and M. A. Green. Appl. Phys. Lett., 66:3636, 1995

[7] www.sunpower . com

[8] Mary D. Archer and Robert Hill, editors.Clean Electricity from Photovoltaics. World Scientific, 2001.

[9] http://www.kyocerasolar.com/about-kyocera/kyocera-solar/news/?id=31

[10] M.P Thekaekara, 'Data on oncident solar energy', Suppl. Proc. 20th Annu. Meet. Inst. Environ Sci., P-21, 1974.

[11] C.H. Henry, 'Limiting efficiency of ideal signal and multiple energy gap terrestrial solar cell', J. Appl. Phys. 51, 4494, 1980.

[12] Principle conclusions of the American physical society study group on solar photovoltaic energy conversion, American physical society, New York, 1979.

[13] D. L. Staebler and C. R. Wronski. Appl. Phys. Lett., 31:292, 1977.

[14] Mary D. Archer and Robert Hill, editors. Clean Electricity from Photovoltaics. World Scientific, 2001.

[15] Y. Bai, D. H. Ford, J. A. Rand, R. B.Hall, and A. M. Barnett. In Conf. Record 26th IEEE Photovoltaic Specialists Conf., Anaheim, page 35, 1997.

[16] Robert B. Hall, Allen M. Barnett, Jeff E. Cotter, David H. Ford, Alan E. Ingram and James A. Rand. Advanced Thin Polycrystalline Silicon Film Solar Cells on Low-Cost Substrates. MRS Proceedings, 426, 117, 1996. doi:10.1557/PROC-426-117.

[17] A. G. Aberle and P. I. Widenborg, "Crystalline silicon thin-film solar cells via high-temperature and intermediate temperature approach," in Handbook of Photovoltaic Science and Engineering. Oxford, U.K: Wiley, pp. 452–486, 2011.

[18] Green MA, Emery K, Hishikawa Y, Warta W, Dunlop ED. Solar cell efficiency tables (version 39).Progress in Photovoltaics: Research and Applications; 20:12–20, 2012.

[19] Green MA, Emery K, Hishikawa Y, Warta W. Solar cell efficiency tables (version 33), Progress in Photovoltaics: Research and Applications; 17:85–94, 2009.

[20] Green MA, Emery K, Hishikawa Y, Warta W, Dunlop ED. Solar cell efficiency tables (version 43).Progress in Photovoltaics: Research and Applications; 22:1–9, 2014.

[21] Green MA, Emery K, Hishikawa Y, Warta W, Dunlop ED. Solar cell efficiency tables (version 44).Progress in Photovoltaics: Research and Applications, 2014.

[22] Panasonic Press Release, 10 April 2014. Panasonic HIT® solar cell achieves world's highest energy conversion efficiency of 25.6% at research level (http://panasonic.co.jp/corp/news/official.data/data.dir/2014/04/en140410-4/ en140410-4. html; accessed 24 April 2014).

[23] Schultz O, Glunz SW, Willeke GP. Multicrystalline silicon solar cells exceeding 20% efficiency. Progress in Photovoltaics: Research and Applications; 12: 553–558, 2004.

[24] S Benagli, D Borrello, E Vallat-Sauvain, J Meier, U Kroll, J Hötzel, Spitznagel J, Steinhauser J, Castens L, Djeridane Y. High-efficiency amorphous silicon devices on LPCVD-ZNO TCO prepared in industrial KAI-M R&D reactor.24th European Photovoltaic Solar Energy Conference, Hamburg, September 2009.

[25] Sai H, Koida T, Matsui T, Yoshida I, Saito K,Kondo M. Microcrystalline silicon solar cells with 10.5% efficiency realized by improved photon absorption via periodic textures and highly transparent conductive oxide. Applied Physics Express; 6: 104101-1–104101-6, 2013.

[26] Engelhart P, Wendt J, Schulze A, Klenke C, Mohr A,Petter K, Stenzel F, Hörnlein S, Kauert M, Junghänel M, Barkenfelt B, Schmidt S, Rychtarik D, Fischer M, Müller JW, Wawer P. R&D pilot line production of multi-crystalline Si solar cells exceeding cell efficiencies of 18%. 1st International Conference on Silicon Photovoltaics, Freiburg, 17–20 April, 2010. (www.elsevier.com/locate/procedia).

[27] Kayes BM, Nie H, Twist R, Spruytte SG, Reinhardt F, Kizilyalli IC, Higashi GS. 27.6% conversion efficiency, a new record for single-junction solar cells under 1 sun illumination. Proceedings of the 37th IEEE Photovoltaic Specialists Conference, 2011.

[28] Osborne, M. Hanergy's solibro has 20.5% CIGS solar cell verified by NREL, 8 April 2014 (http://www.pv-tech.org/ news/ hanergys solibro has 20.5 cigs solar cell verified by nrel; accessed 24 April 2014).

[29] Komiya R, Fukui A, Murofushi N, Koide N, Yamanaka R, Katayama H. Improvement of the conversion efficiency of a monolithic type dye-sensitized solar cell module.

Technical Digest, 21st International Photovoltaic Science and Engineering Conference, Fukuoka, November: 2C-5O-08, 2011.

[30] Keevers MJ, Young TL, Schubert U, Green MA. 10% Efficient CSG mini modules. 22nd European Photovoltaic Solar Energy Conference, Milan, September 2007.

[31] Nasuno Y., Kondo M., Matsuda A., Jpn. J. Appl. Phys. 41, 5912, 2002.

[32] Shah A., Meier J., Vallat-Sauvain E., Droz C., Kroll U., Wyrsch N., Guillet J., Graf U., Thin Solid Films 403-404, 179, 2002.

[33] Hsiao H.L., Hwang H.L., Yang A.B., Chen L.W., Yew T.R., Appl. Surf. Sci. 316, 1999.

[34] Matsumura H., Jpn. J. Appl. Phys. 30 1522, 1991.

[35] Cheng H.C., Huang C.Y., Wang F.S., Lin K.H., Tarntair F.G., Jpn. J. Appl. Phys. 39, L-19, 2000.

[36] Dyer T.E., Marshall J.M., Pickin W., Hepburn A.R., Davies J.F., J. Non-Cryst. Solids 164-166, 1001, 1993.

[37] Aberle A.G., Harden N.P., Oelting S., J. Cryst. Growth 226, 209, 2001.

[38] Y. Tsunomura M. Taguchia, T. Babaa, T. Kinoshitaa, H. Kannoa, H. Sakataa, E. Maruyamaa, M. Tanaka, Solar En. Mat. Solar Cells 2008. (doi:10.1016/j.solmat.2008.02. 037, in press.)

[39] K. V. Maydell, H. Windgassen, W. A. Nositschka, U. Rau, P. J. Rostan, J. Henze, J. Schmidt, M. Scherff, W. Fahrner, D. Borchert, S. Tardon, R. Brüggemann, H. Stiebig, M. Schmidt, Proc. 20th European Photovoltaic Solar Energy Conference, Barcelona, Spain, p. 822, September 2005.

[40] P.J. Ribeyron, A. Vandeneynde, J. Damon-Lacoste, D. Eon, P. Roca Cabarrocas, R. Chouffot, J.P. Kleider, R. Brüggemann, Proc. 22nd European Photovoltaic Solar Energy Conference, September 2007, Milan, Italy, p. 1197, 2007.

[41] H. M. Branz, C. W. Teplin, D. L. Young, M. R. Page, E. Iwaniczko, L. Roybal, R. Bauer, A. H. Mahan, Y. Xu, P. Stradins, T. Wang, Q. Wang, Thin Solid Films 516, 743, 2008.

[42] S. Olibet, E. Vallat-Sauvain, C. Ballif, L. Korte, L. Fesquet, Proceedings of the 17th Workshop on Crystalline Silicon Solar Cells and Modules: Materials and Processes, Vail, Colorado USA, p. 130, August, 2007.

[43] M. Keevers, T. Young, U. Schubert, and M. Green, 10% Efficient CSG minimodules, Proc. 22nd EUPVSEC, Milan, pp. 1783–1790, 2007.

[44] R. Egan, M. Keevers, U. Schubert, T. Young, R. Evans, et al., CSG minimodules using electron-beam evaporated silicon, Proc. 24th EUPVSEC, pp. 2279–2285, 2009.

[45] P. Timans, J. Gelpey, S. McCoy, W. Lerch, and S. Paul, Millisecond annealing: past, present and future, MRS Spring Meeting 2006 912, pp. 3–14, 2006.

[46] K. Ohdaira, T. Fujiwara, Y. Endo, S. Nishizaki, and H. Matsumura, Explosive crystallization of amorphous silicon films by flash lamp annealing, J. Appl. Phys. 106 (4), p. 044907, 2009.

[47] Sergey Varlamov, Bonne Eggleston, Jonathon Dore, Daniel Ong, and Rhett Evans, 'Diode-laser processed crystalline silicon solar cells', SPIE, News room, 10.1117/2.1201303.004744, 2013.

[48] S. Varlamova, J. Dorea, R. Evans, D. Ong, B. Eggleston, O. Kunz, U. Schubert, T. Young, J. Huang, T. Soderstrom, K. Omaki, K. Kim, A. Teal, M. Jung, J.Yun, Z.M. Pakhuruddin, R. Egan, M.A. Green, "Polycrystalline silicon on glass thin-film solar cells: A transition from solid-phase to liquid-phase crystallised silicon", Solar Energy Materials & Solar Cells 119, 246–255, 2013.

[49] D. Mathiot, A. Lachiq, A. Slaoui, S. Noel, J.C. Muller, C. Dubois, Mater. Sci. Semicond. Process.1, 231, 1998.

[50] M. L. Terry, A. Straub, D. Inns, D. Song, A. G. Aberle, Appl. Phys. Lett.86, 1, 2005.

[51] P. Doshi, A. Rohatgi, M. Ropp, Z. Chen, D. Ruby, D.L. Meier, Sol. Energy Mater. Sol. Cells, 41, 31, 1996.

[52] M.L. Terry, D. Inns, A.G. Aberle, Adv. Optoelectron. 83657, 2007.

[53] A. Chowdhury, A. Bahouka, S. Steffens, J. Schneider, J. Dore, F. Mermet, and A. Slaoui, 'Laser annealing of thin film polycrystalline silicon solar cell', EPJ Photovoltaics, 4, 45108, 2013. (DOI:10.1051/epjpv/2013019).

[54] http://www.pv-magazine.com/

[55] M. S. Keshner and R. Arya, Study of Potential Cost Reductions Resulting from Super Large-Scale Manufacturing of PV Modules, 2004.

[56] S. Bauer, B. Schr¨oder, W. Herbst, and M. Lill. In *Proceedings of the Second World Conference on Photovoltaic Solar Energy Conversion*, page 363, 1998.

[57] U. Weber, M. Koob, R. O. Dusane, C. Mukherjee, H. Seitz, and B. Schroder. In *Proceedings of the European Photovoltaic Solar Energy Conference, Glasgow*, page 286, 2000.

[58] B. Nelson, E. Iwaniczko, A. H. Mahan, Q. Wang, Y. Xu, and R. S. Crandall. In Extended abstract of First International Conference on Cat-CVD (Hot Wire CVD), page 291, 2000.

[59] J. Meier, E. Vallat-Sauvain, U. Kroll, S. Dubail, S. Golay, L. Feitknecht, P. Tores, S. Fay, D. Fischer, and A. Shah. Sol. Energy Mater. Sol. Cells, 66:73, 2001.

[60] C. Niikura, Y. Poissant, M. E. Gueunier, J. P. Kleider, and J. E. Bouree. J. Non-Cryst. Sol., 299:1179, 2002.

[61] J. K. Rath, A. Barbon, and R. E. I. Schropp. J. Non-Cryst. Sol., 227:1277, 1998.

[62] https://hwcvd.fraunhofer.de/en/welcome

[62] R. E. I. Schropp, 'Industrialization of HWCVD for thin film applications' Proceding of International Conference on HWCVD-8, Braunschweig, Germany, October 13—16, 2014.

[64] H. Matsumura, D. H. Chi, T. C. Thi, S. Tsuzaki, K. Koyama, K. Ohdaira, 'Cat-Doping A Novel Low Temperature Impurity Doping Technology Using Hot Catalyzing Wires' Proceding of International Conference on HWCVD-8, Braunschweig, Germany, October 13—16, 2014.

[65] R.O. Dusane, A. Kumbhar, N. Meshram, S. JK Sundar, 'Low temperature deposition of SiO_2 films by HWCVD', Proceding of International Conference on HWCVD-8, Braunschweig, Germany, October 13—16, 2014.

[66] D.S. Wuu, B.R. Wu, H.Y. Mao, J.Y. Yang, 'Hot wire chemical vapour deposition prepared p-type silicon carbide/n-type crystalline silicon hetero junction solar cells', Proceding of International Conference on HWCVD-8, Braunschweig, Germany, October 13—16, 2014.

[67] A.R. Middya, K. Ghosh, 'Advances in Hot Wire CVD Polycrystalline Silicon thin film with Hydrogen for PV Applications', Proceding of International Conference on HWCVD-8 , Braunschweig, Germany, October 13—16, 2014.

[68] F. Finger, R. Carius, T. Chen, K. Ding, A. Heid, F. Köhler, S. Muthmann, 'Application of HWCVD for material development in solar energy research', Proceding of International Conference on HWCVD-8, Braunschweig, Germany, October 13—16, 2014.

[69] C.H.M. van der Werf, T. Budel, M. S. Dorenkamper, D. Zhang, W. J. Soppe, R. E. I. Schropp, H. de Neve, 'a-Si:H single junction solar cells deposited by HWCVD on nano imprinted paper', Proceding of International Conference on HWCVD-8 , Braunschweig, Germany, October 13—16, 2014.

Chapter 2

Hot Wire Chemical Vapour Deposition

2.1 Introduction

In this chapter we have described the mechanism and operation of the catalytic hot wire chemical vapour deposition (HWCVD) cluster instrument used for the synthesis of polycrystalline, amorphous and microcrystalline silicon films. In our study we have used two separate HWCVD systems. For all samples, intrinsic poly crystalline silicon film and p-type amorphous silicon film synthesis is performed in a three chamber instrument. This system does not have provision for synthesis of n type doped silicon film. N-type microcrystalline silicon film synthesis performed in a separate four chamber instrument. Details of these two systems are discussed in Appendix I.

We have also conducted a brief study on substrate temperature using in situ thermocouple, contact with the top surface of the sample. Strategies against contaminations are well explained as the deposition chambers were gold contaminated.

2.2 The HWCVD for polycrystalline and amorphous material

Synthesis of poly crystalline and amorphous silicon films were performed using the three spherical chamber HWCVD apparatus placed in an arrangement of isosceles triangle shape with one common load lock chamber shown in figure 2.2. Sample can be transferred from one chamber to another without breaking the vacuum. During sample transfer vacuum pressure can be maintained 2×10^{-6} mbar.

This makes the instrument very useful for continuous growth of device fabrication shown in figure 2.1. The spherical shapes for reaction chamber are specially chosen to reduce the internal surface area for a given volume [1].

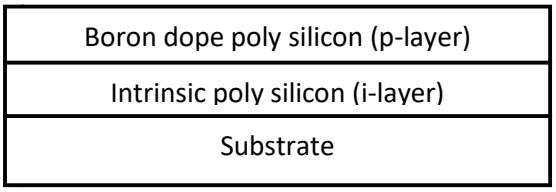

Figure 2.1 Block diagram of i-p device structure fabricated using HWCVD without breaking the vacuum with the help of sample transfer mechanism.

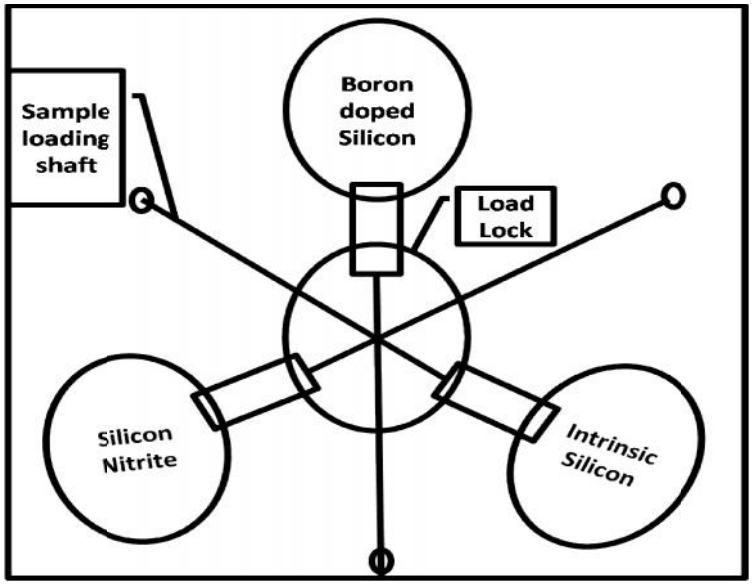

Figure 2.2 Block diagram of top view of three chamber HWCVD cluster tool for synthesis of polycrystalline and amorphous silicon film.

2.2.1 Growth condition

Silicon films are synthesized using silane (SiH_4) gas. SiH_4 is dissociated into SiH_3, SiH_2, SiH and related species using gas discharge (plasma enhanced chemical vapour deposition (PECVD)) or thermal excitation (hot wire chemical vapour deposition (HWCVD)). Atomic hydrogen is produced during the above process. Additional hydrogen is used to control the quality of growth. In addition to deposition, atomic hydrogen can react with silicon and

cause etching. Some hydrogen is also incorporated in the growing film depending on the temperature of the substrate. One can get a large variety of silicon films by controlling the growth parameters. These may vary from amorphous silicon using concentrated silane at substrate temperature 200°C, micro crystalline / nano crystalline silicon using hydrogen diluted silane at 200°C, to polycrystalline silicon using concentrated silane at higher substrate temperature about 600°C.

Synthesis of silicon films is done under optimal growth condition, which means adjusting the available parameters those are critical for the synthesis of the silicon film. In our case chamber pressure, substrate temperature, filament temperature, silane to hydrogen ratio, gas flow rate were taken into consideration. Few other parameters such as the distance between substrate and the filament, filament arrangement and gas flow shower were fixed during the design of the HWCVD instrument shown in figure 2.3.

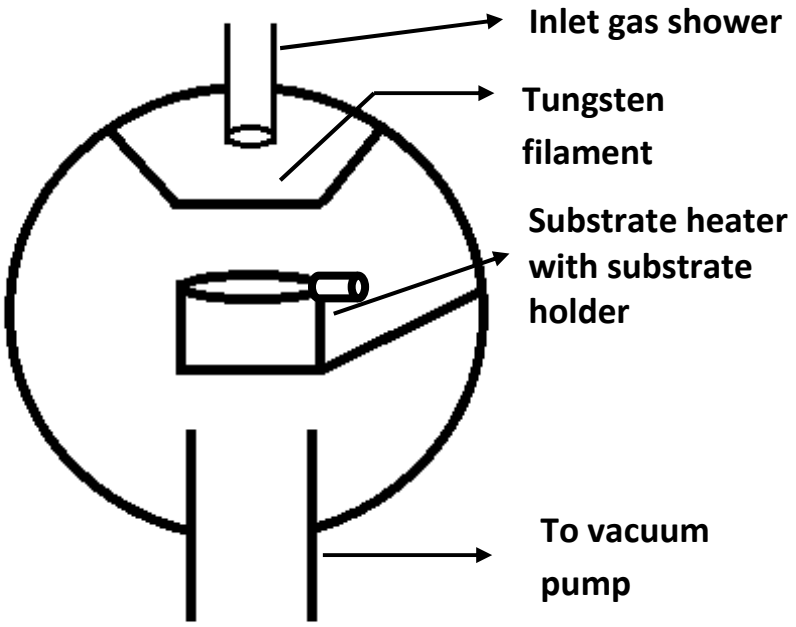

Figure 2.3 Schematic of HWCVD chamber used for growth of polycrystalline and amorphous silicon film.

All growth experiments for thin film synthesis were performed in the HWCVD system having base pressure of no higher than 1×10^{-6} mbar. Process pressure was maintained between 1×10^{-1} mbar to 6×10^{-2} mbar. A throttle valve at the exit controls the

reactor pressure by changing the volumetric flow rate of the gases leaving the reactor. A mixture of pure SiH_4 and pure H_2 was used as process gas for intrinsic silicon film. Diborane (5% diborane, 95% hydrogen) gas was introduced as a source of boron for p-type silicon film. Single filament of tungsten wire, 65 cm long and 0.5 mm diameter wound in a zigzag shape was resistively heated to 1900°C using a dc power supply. The filament is placed at about 5cm height from the substrate. The area covered by the filament is about 9 cm $\times$ 9 cm. The hot filament radiatively heats the substrate to 200°C as measured with a thermocouple placed below the substrate holder. Higher substrate temperature was achieved by a resistive heater placed in contact with the substrate holder from below. A moveable shutter between the wire and the substrate allows several growth steps to be performed under selected gas composition, substrate temperature and filament temperature. This also provides a definite starting and ending point for each step during the growth of the film.

2.2.2 Mechanism of growth of silicon film

The basic steps for silicon film deposition are: dissociation of the reaction gases into precursors on the surface of the hot wire, transportation of precursors to substrate, and diffusion / deposition of the dissociated useful particle species on the surface of the substrate to grow the film. The main factors of the first sub-processes are filament temperature, growth pressure, gas flow rates and substrate temperature. Reaction rate increases with an increase in these factors as evident in published papers [2]. The second sub-processes depend upon the silane to hydrogen ratio and pressure of the reaction gas. If the pressure is higher, the possibility of secondary reactions become higher, and the structure of the deposited film will be inferior. The distance between filament and substrate allows the substrate to be radiatively heated to about 200°C. The substrate temperature can be raised further by additional heating with substrate heater kept below the substrate holder. A closer arrangement will increase the substrate temperature additionally with the substrate heater from the bottom. This will affect the low temperature (below 200°C substrate temperature) growth condition. A higher substrate temperature results in higher mobility of the atoms (Si, H) and causes a relaxation of the structure; thereby resulting in a better quality film [3]. We have used glass substrates during several growth processes which limit the substrate temperature to 600°C though the system was designed to reach 800°C substrate temperature.

2.2.3 Challenges with Hotwire CVD

The main challenges that concern Hotwire CVD are i) uniform film deposition over large substrates (2-4 inch diameter wafer) ii) changes in the properties of the filament as it ages and spaced in a zigzag pattern iii) chamber pressure limits the possible hydrogen dilution. Uniformity has been addressed in commercial hotwire CVD equipment by modifying filament geometry, gas shower geometry and in some cases by rotating the substrate. Several researchers have found tantalum [4] to be a better filament material than tungsten [5] with lower temperature around 1650 °C. In our case we have kept filament temperature 1900°C.

Chamber pressure can be controlled with mechanical pump and throttle valve. Still maximum hydrogen dilution was 20 sccm which leads to 1.1×10^{-1} mbar of growth chamber pressure. In some stage of growth process we have to reduce the hydrogen dilution to keep the chamber pressure constant. Lower hydrogen dilution leads to more broken and dangling bonds. This will degrade the material quality of the film [6]. We have introduced a hydrogen passivation stage after the growth to overcome this problem.

2.2.4 Calibration of substrate temperature

The temperature of the substrate was determined in situ using a type K (Chromel-Alumel) thermocouple in contact with the top of substrate. Temperature profile of substrate is shown in figure 2.4 under various conditions.

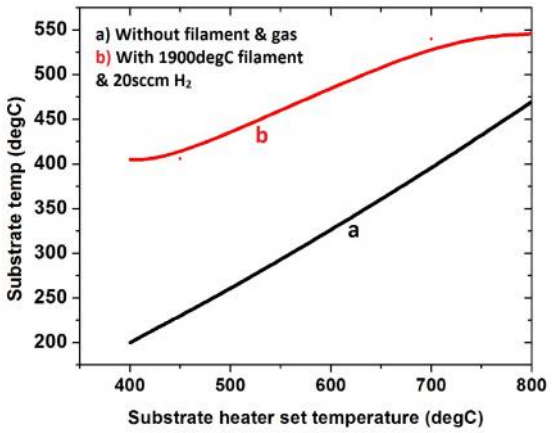

Figure 2.4: Measured substrate temperature versus set substrate heater temperature profile using K-type (Chromel-Alumel) thermocouple.

With filament cold and gas flowing, the substrate temperature increased linearly with the substrate heater setting (curve 'a' in Fig 2.4). With filament hot at ~ 1900°C and gas flow, the substrate temperature increased maximum 550°C. It is clear that the substrate heater set temperature is much higher than the actual temperature of substrate.

This may be because the thermocouple reading the substrate heater temperature is near the heater below the substrate holder and far from the substrate. During the above calibration, we keep the tip of a sheathed thermocouple tip touching a dummy 2 inch diameter silicon wafer, kept on the substrate holder, which is used to hold the smaller (1cm×2cm) glass substrate used for the growth. The calibration helps us to evaluate the actual substrate temperature which was crucial for our study as we have used glass as substrate.

2.2.5 Calibration of chamber pressure

We performed the calibration of chamber pressure keeping one sccm continuous silane flow with changing the hydrogen flow ranging from 1 to 75 sccm.

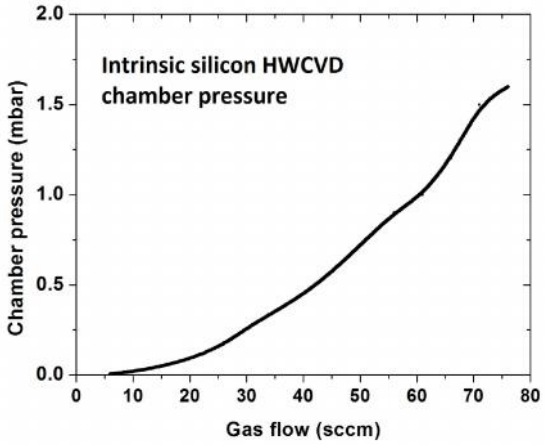

Figure 2.5: Intrinsic silicon growth chamber pressure versus gas (1sccm Silane with H_2) flow plot for the calibration of maximum possible hydrogen dilution.

The corresponding chamber pressure versus gas flow is plotted in figure 2.5. We have to maintain maximum 20 sccm hydrogen flow during growth to maintain the maximum growth pressure under 1.2×10^{-1} mbar.

In some stage of our growth we had to reduce the hydrogen flow to maintain the chamber pressure constant which affected the material quality.

2.3 The HWCVD system for n-type microcrystalline silicon

For phosphorous doped n-type silicon film we have used automated four chamber HWCVD cluster tool with one load lock chamber [7,8]. In this system, samples can be loaded and transferred between chambers using a computerized robotic hand without breaking the vacuum. The chambers were cylindrical and operated in a tantalum filament at lower temperature (1650°C). Microcrystalline n-type phosphorous doped silicon film was deposited on glass and FTO coated glass substrate using this system. A schematic diagram of the growth chamber is shown in Fig 2.6. Organization of the filament and substrate assembly is different than we explained in earlier three chamber HWCVD. Here the substrate was placed upside down on the top of the tantalum filament assembly where the gas flow shower was placed at the bottom of the chamber below the tantalum filament.

2.3.1 Growth conditions

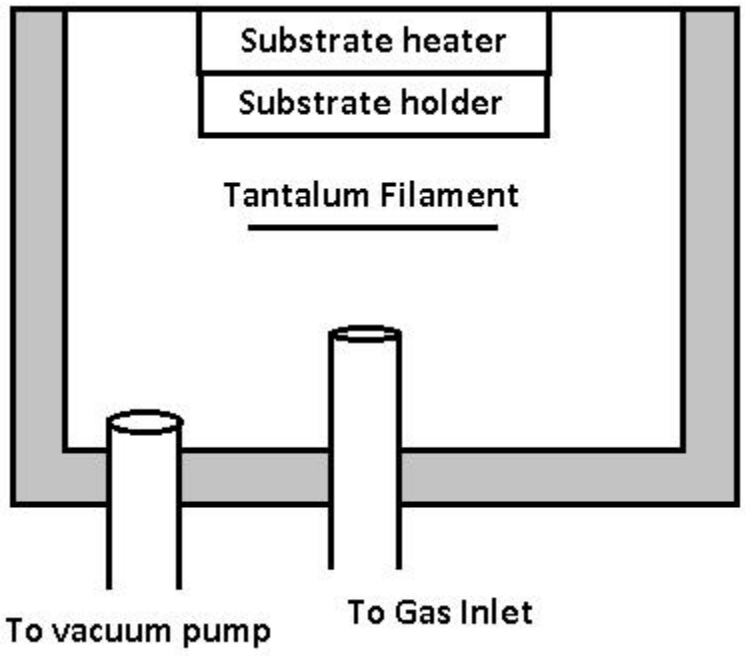

Figure 2.6 Schematic of HWCVD chamber used for deposition of microcrystalline phosphorous doped n-type silicon film.

Thin phosphorous doped microcrystalline silicon film deposited at 350°C substrate temperature with a filament temperature 1650°C for 45 minutes. Base pressure was 1×10^{-6} mbar while process pressure was maintained at 6.6×10^{-2} mbar. The microcrystalline silicon films were grown at a gas flow ratio of SiH_4:H_2:PH_3= 2:50:1 sccm.

2.4 Discussion

HWCVD is an interesting technique for the low-temperature growth of thin-film silicon. It offers efficient use of high deposition rates, and high hydrogen passivation of defects. The choice of filament and its temperature are critical to the determination of the deposition environment and appropriate precautions must be taken in order to achieve high quality, contamination-free films. For the deposition regime of interest, low-temperature epitaxial growth, tungsten was the most reliable catalyst filament. Tungsten offers a large process window for silicon films with high hydrogen dilution.

2.5 References

[1] Nitin S. Kale, PhD thesis, “Making HWCVD a viable technology alternative for BioMEMS application”, Indian Institute of Technology Bombay, Mumbai, India, 2007.

[2] J. Doyle, R. Robertson, G. H. Lin, M. Z. He, and A. Gallagher. J. Appl. Phys., 64:3215, 1988.

[3] Ruihua W, Zhiqiang L, Li L, Jahe L, “Study of HWCVD technique for silicon thin film”, Solar Energy Mat & Solar Cells 62 p. 193, 2000.

[4] Diehl F., Scheib M., Schröder B., Oechsner H., J. Non-Cryst. Solids 227-230, 973, 1998.

[5] Matsumura H., Jpn. J. Appl. Phys. 37, 3175, 1998.

[6] I.-W. Wu, W. B. Jackson, T.-Y. Huang, A. G. Lewis, and A. Chiang, IEEE Electron Devices Lett., Vol. 11,pp. 167-170, 1990.

[7] R. O. Dusane, Suvarna R. Dusane, V. G. Bhide and S. T. Kshirsagar, Hydrogenated microcrystalline silicon films produced at low temperature by the hot wire deposition method, Appl. Phys. Lett. 63, 2201, 1993. (doi.org /10.1063 /1.110801)

[8] http://www.met.iitb.ac.in/main.html?s=y&sec=research&content=facilities/labs /thin FilmsSC/ hwcvd.

Chapter 3

Characterization techniques

3.1 Introduction

This chapter briefly describes the characterization techniques used to study the properties of intrinsic as well as phosphorous and boron doped silicon films grown on multiple substrates using catalytic HWCVD technique. Methodology and theoretical aspects related to morphological, structural, optical, and electrical characterization techniques are discussed. Brief discussion on secondary ion mass spectrography, energy dispersive x-ray spectrography and infrared spectroscopy for compositional analysis is also presented. Brief description of each instrumentation setup is also given in this chapter. Images of instrument are given in Appendix III.

3.2 Measurement of thickness

3.2.1 Stylus surface profiler

The first measurement carried out for every sample after the film deposition is thickness measurement which was performed using stylus surface profiler. The DektakXT stylus profiler from Bruker, Billerica, MA, USA, was used for measuring thickness less than 300 nm and Ambios XP2 stylus profiler was used to measure thicker films [1]. From this measurement, knowing the deposition duration, the average deposition rate was calculated

for each growth process. Surface roughness, step height, crater depth were also estimated with a precession of 10 nm resolution.

The profiler incorporates an optical deflection height measurement mechanism and magneto static force control system which results in a low force (loads as small as .05 mg) and low inertia stylus assembly. This makes the surface profiler capable of measuring soft films and substrates without surface damage. In our case we allowed the stylus to exhibit a very low force on the sample surface as low as 3 mg, thus the film was left scratch free after the measurement.

3.2.2 Optical reflectance

Spectroscopic reflectance measures the amount of light reflected from the surface of a thin film over a range of wavelengths with the incident light perpendicular to the sample surface which one can use for measuring the thickness of a thin transparent and semi-transparent film [2]. We have used optical Reflectometer by Filmetrics, Inc. CA, USA for measuring the thickness of oxide layer deposited using atmospheric furnace [3]. The instrument uses optical techniques to determine thin film characteristics by measuring how the film interacts with white light. The reflectance spectrum from thin film on a non absorbing substrate exhibits oscillations in intensity with the maxima at the wavelengths

$$\lambda = \frac{2ndcos(\theta)}{m} \quad ----------(3.1)$$

Here n is refractive index of thin film, d is thickness of thin film, θ is incident angle at the substrate-thin film interface and m = 1,2,3,…

Taking the wavelength at two maxima and subtracting one from the other and using equation (3.1) we can calculate the thin film layer thickness [4].

$$d = \frac{i}{2n\left(\frac{1}{\lambda_o} - \frac{1}{\lambda_1}\right)\cos(\theta)} \quad ----------(3.2)$$

Here i, is number of complete cycle from wavelength range λ_0 to λ_1.

The instrument uses a microscope to shine light on a small area of the sample [5,6]. The reflected light from the sample passes through a spectrometer. The light detection is performed using photo diode array with the various wavelengths falling on different diodes

in the array for automatic data acquisition [7,8]. Optical techniques are usually preferred for measuring thin films because they are accurate, non-destructive and require little or no sample preparation. The optical wave length range of the light source is 300 nm to 1000 nm.

3.3 Surface Morphology

Surface morphology includes the quantitative evaluation of nucleation density, shape and features in the early stage of growth of silicon film. This also includes the topographical analysis of silicon film after laser irradiation. Following techniques were used for this purpose.

3.3.1 Atomic Force Microscopy (AFM)

For characterization of intrinsic polycrystalline silicon thin film nucleation stages tapping mode AFM surface profiling was done [9,10,11]. Scanning probe microscope Pico scan 210, from Pico SPM was used in this purpose [12].

In this instrument, Silicon or SiN_2 cantilever with tip radius of 4 nm is brought into proximity of sample surface. Force between the tip and the sample surface leads to a deflection of cantilever according to Hooke's law. The deflection of tip is measured using a laser spot reflected from the top surface of the cantilever to an array of position sensitive photo diode (PSD) as detector [13]. Feedback mechanism is connected to the piezoelectric tube which can move in z direction (up-down) maintaining a constant force between tip and the sample surface. Here we place the sample on a piezoelectric tube and the tube can be moved up and down.

In tapping mode, the cantilever is allowed to oscillate at a constant frequency slightly above its resonant frequency where the maximum amplitude is below 10 nm above the sample surface. Forces which extend above the surface act to decrease the resonant frequency of the beam type cantilever where the resonant frequency is given by [14]

$$f_o = \frac{1}{2\pi}\sqrt{\frac{k}{m}} \text{----------} (3.3)$$

Here k is spring constant and m is the mass of cantilever.

Combining the decrease in resonant frequency and feedback loop, system measures the tip to sample distance at each x-y data point. Scanning software constructs a topographical image of sample surface.

3.3.2 Scanning Electron Microscopy (SEM)

Topographical observation of silicon films was done using Field Emission Gun Scanning Electron Microscope (FEGSEM) from Zeiss Ultra 55 FE-SEM with Oxford EDX system [15]. In conventional SEM, thermionic emitter uses electrical current to heat up a tungsten or lanthanum hexa boride (LaB_6) filament. When the heat is enough to overcome the work function of the filament material, the electrons can escape from the material itself. Thermionic sources have relative low brightness; suffer from evaporation of cathode material and thermal drift during operation. Here Field Emission is one way of generating electrons that avoids these problems. A field emission gun (FEG) does not heat the filament. The emission is reached by placing the filament in a large electrical potential gradient. The FEG filament is usually a wire of Tungsten (W) fashioned into a sharp point. The image in an SEM is produced by scanning the sample with a focused electron beam and detecting the secondary or back-scattered electron using an Everhart-Thornley (ET) detector [16].

As the substrates were insulating material we have used silver paste and carbon tape to attach the sample with metal stub while taking images. All images were taken with 5kV electron beam, close working distance 3.5 mm and normal incident electron beam on the sample surface.

3.3.3 Cross section TEM imaging

The structural properties such as thickness, crystalline orientation, diffraction pattern of the i-p structure were evaluated by transmission electron microscope (TEM) model CM200 from PHILIPS [17], equipped with a field emission electron gun operated at 200 kV with a resolution of 0.2 nm. Accelerated electrons using this 200 kV high voltage are focused on the sample by condenser lenses. The sample is placed on a small copper grid of few mm in diameter. The sample needs to be thin enough for electron to pass through the sample. We have taken bright field image to observe material structure, dark field image to observe diffraction patterns and high resolution images for lattice imaging [18,19]. The resolution of image can be calculated from [20].

$$s = \frac{0.61\,\lambda}{NA} - - - - - - - - - (3.4)$$

$$\lambda = \frac{h}{mv} = \frac{h}{\sqrt{2qmV}} = \frac{1.22}{\sqrt{V}}\ nm - - - - - - (3.5)$$

Here NA is numerical aperture for electron microscopy = 0.01, λ=0.003 nm for V=200kV. So the resolution s = 0.2 nm.

The sample preparation for cross sectional TEM imaging was performed using a conventional route explained in Appendix II. A Si substrate was oxidized placed inside the chamber during the growth of device structure. This Si/SiO_2 substrate, coated with the same layers as the device, mimics the layers deposited on glass for the device but it is easier to cleave. Therefore, it was used to prepare X-TEM imaging sample for investigating the deposited layers. 20 nm chromium followed by 80 nm gold layer was evaporated using thermal evaporator on top of the film to protect the film from damage during X-TEM sample preparation process. This also makes X-TEM imaging easier to locate the interfaces between films and focus as gold looks dark under transmission electron microscope.

3.3.4 3D optical microscopy

3D optical images were taken using the well known confocal optical microscopy method where a light beam is focused in one plane at a time to form an image which can be named with respect to a spot focusing in z axis [21,22]. Then by raising the objective lens vertically using a precession piezoelectric transducer, the next plane is focused and imaged [23]. Thus it takes 800 to 1000 slices and then adds all to give a 3D image of hills and valleys. In some cases the z-axis precision movement was as small as 20 nm.

In our study optical images were taken using motorized vertical axis zeta 3D microscope from Zeta Instrument [24], covering an image area of 95 micron by 71 micron. Evaluation of surface roughness due to laser irradiation was performed using 3D optical microscopy.

3.3.5 2D optical microscopy

We have used MX61-F Olympus microscope [25] for optical imaging as a primary tool for viewing surface morphology of hot wire CVD grown film as well as laser irradiated film. Also outline of devices after masking was observed. Formation of cracks due to high tensile stress was also visible under this microscope.

Optical 2D image of silicon film was taken using bright field microscopy where light falls vertically on the top surface of the sample and dark field microscopy where light falls at a shallow angle on the top of the sample surface. Bright field microscopy is useful to observe the sample surface topography whereas dark field microscopy is useful to observe small surface irregularities like dust or cracks. Typically 2D optical microscope is useful for feature sizes about 0.5 micron. Resolution of image can be calculated using equation (3.4) where NA=1, λ=500 nm which gives resolution s= 300 nm [26].

3.4 Crystalline orientation

Structural characterization of silicon films was performed using high resolution x-ray diffraction (XRD) instrument Smartlab 3kW from Rigaku Corporation, Japan [27], equipped with Cu Kα radiation source operated at 40 keV. The apparatus is operated in θ - 2θ geometry for thick silicon films. To observe crystallographic orientation for thin film, as at the nucleation stage of the film synthesis, x-ray beam with very small incident grazing angle of 0.5 deg was used which is larger than the critical angle to obtain total internal reflection. The XRD instrument was operated in a step-scan mode in increments of 0.02˚ where counts were accumulated for two sec at each step. For analysis purpose we have considered only three peaks (111), (220) and (311). Calculations of peak parameters are shown in brief [28].

$$t = \frac{0.9\times\lambda}{B\,(radian)\,cos\theta} = \frac{0.9\times 1.5406A^{\circ}}{FWHM(radian)cos(\frac{2\theta}{2})} = \frac{1.38654A^{\circ}}{\frac{FWHM}{2}\times 0.017453(degree)\times cos(\frac{2\theta}{2})} - -(3.6a)$$

$$d = \frac{n\lambda}{2sin\theta} - - - - - - - (3.6b)$$

$$d = \frac{a}{\sqrt{h^2+k^2+l^2}} - - - - - - - - (3.7)$$

Here t is grain size, FWHM is full width half maxima, d is crystal planes spacing, a is lattice parameter, h,k,l are Miller indices, λ is wavelength of x-ray beam, θ is half of diffraction angle.

For silicon cubic crystal a= 5.428A°, λ=1.5406 A° for copper k(α) radiation x-ray beam. Using equation (3.7) for (h,k,l) = (111), d=3.13 A°, for (h,k,l) = (220), d= 1.91 A° and for (h,k,l) = (311), d= 1.64 A°. Using d value in equation 3.6b corresponding 2θ calculated (111) plane is 28.46°, (220) plane is 47.3° and (311) plane is 56°.

All data was taken in the angular range of 20^{o} - 60^{o}. In some cases peaks corresponding to substrates contribution have been removed to facilitate presentation and analysis. Substrate peak observed at 2θ corresponding to the silicon is 69°, sapphire is 42° and nickel is 54° from XRD spectrum.

3.5 Quantifying crystallinity

Evaluation of crystallinity and crystalline fraction of silicon film was performed using confocal Raman spectroscopy before and after laser irradiation. Here we have also presented Raman Images of silicon film after laser irradiation. This Raman images allows us to evaluate the crystallinity over a small area. This helps us to find the uniformity of absorption of laser irradiation by silicon film.

3.5.1 Raman spectroscopy

Raman spectroscopy based on the Raman Effect first reported by Raman in 1928 [29]. When light is scattered from the surface of a sample, the scattered light is found to contain mainly wavelengths that were incident on the sample (Raleigh scattering) but also at different wavelengths at very low intensities (1 in 10^{8} parts) that represent an interaction of the incident light with the material [30]. The interaction of the incident light with optical phonons is called Raman scattering. If the incident photon imparts energy to the lattice in the form of a phonon (phonon emission) it emerges as a lower-energy photon. This down-converted frequency shift is known as Stokes-shifted scattering. In Anti-Stokes-shifted scattering the photon absorbs a phonon and emerges with higher energy. The anti-Stokes mode is much weaker than the Stokes mode and it is Stokes-mode that is usually monitored. Raman spectroscopy is a vibrational spectroscopic technique that can detect both organic

and inorganic species and measure the crystallinity of solids. During Raman spectroscopy measurements a laser pump beam is incident on the sample. The weak scattered light or signal is passed through a double monochromator to reject the Raleigh scattered light and the Raman-shifted wavelengths are detected by a photo detector [31].

Raman spectroscopy is also sensitive to crystal structure. Different crystal orientations give slightly different Raman shifts. The lines become very broad for amorphous semiconductors and become very sharp for crystalline material, allowing a distinction to be made between single crystal, polycrystalline, and amorphous materials. The frequency is also shifted by stress and strain in thin film. Both compressive and tensile stress can be determined with compressive stress giving an upward and tensile stress a downward shift from the unstressed 520 cm^{-1} [32].

Crystalline quantity of laser annealed and intrinsic poly silicon film on glass was evaluated using Horiba HR 8000 Confocal Raman spectroscopy [33]. Air cooled green argon laser of wavelength 514.5 nm with a power of 10 mW was used as an illumination source. A confocal microscope with 20x lens was used to focus the laser onto the surface of sample. In the confocal approach a spatial filtering techniques was used to eliminate out-of-focus light or glare from the sample to the detector. Confocal Raman spectroscopy couples a Raman spectrometer to a standard optical microscope which allows high magnification visualisation of a sample and Raman analysis with a microscopic laser spot. Range of the measured Raman shift is from 200 cm^{-1} to 800 cm^{-1} with a 100 μm slit for 60sec signal acquisition time.

3.5.2 Raman imaging

Raman imaging is basically taking Raman spectrum at several points in the plane of sample. In our study Raman imaging was performed over 10 μm $\times$ 10 μm area with a 50x objective lens using confocal Raman microscope from WITec Inst [34]. A 532 nm green laser of 4 mW power was used as an excitation source. Spectral information on different point on a sample was acquired using point by point mapping technique. A motorized stage moves the sample under the laser which collects a spectral hypercube (a complete Raman spectrum over the range 100 cm^{-1} to 600 cm^{-1} from each point). This generates a matrix which obtained by scanning 100 lines per image with 100 points per line, over 10μm $\times$ 10μm area, moving the electronically controlled stage in 100 nm increments.

Each scan takes 20 min to complete. Image is obtained using fit spectrum with theoretical Lorentzian curve fitting. Multiple images were created from the sum of 10000 spectrums per scan. We have used full width half maximum (FWHM) of peak width to generate Raman Image. Sum of counts in a range of Raman shift 100 cm^{-1} to 430 cm^{-1} and 490 to 525 cm^{-1} were also used to generate Raman images.

3.6 Quantifying material quality

3.6.1 Photoluminescence (PL) spectrum

The PL spectrum tool from Advanced Photonics [35] comprises of three main sections: the excitation source - in this case a 532 nm green laser with a power output of 95mW, the lenses arrangement to guide the laser beam on to the sample surface and the spectrum detection system (spectra-pro 2750) in this case a spectrometer fitted with a liquid nitrogen cooled InGaAs detector [36].

When light particle (photon) has energy greater than the band gap energy incident on a material surface, then it can be absorbed by the material and thereby raise an electron from the valence band up to the conduction band across the forbidden energy gap. Subsequent to the excitation, the electron eventually falls back down to the valence band (recombine with the hole) losing energy as a luminescent photon which is emitted from the material. The process of photon-excitation followed by photon emission is called photoluminescence (PL) [37]. The emitted photon energy depends on the recombination process, where the commonly observed PL transitions are i) band-to-band, ii) free exciton, iii) bound exciton and iv) donor-acceptor recombination [38].

Samples were investigated using a beam of 1.5 mm diameter, slit width 500 microns, laser exposure duration 1 sec and laser fluence 5 J/cm^2. All data was collected in wavelength range of 800 nm to 1600 nm. All PL spectra were taken at room temperature. During each measurement maximum intensity of photon flux received by detector was assured by varying and adjusting the lenses arrangement.

3.7 Compositional analysis

3.7.1 Fourier Transformation Infrared (FTIR) Spectrum

Fourier transform spectrometer consists of a Michelson interferometer [39]. Light from an infrared source is directed onto a beam splitter, creating two separate optical paths by reflecting 50% of the incident light and transmitting the remaining 50%. In one path the beam is reflected back to the beam splitter by a fixed position mirror, where it is partially transmitted to the source and partially reflected to the detector. In the other path of the interferometer, the beam is reflected by the movable mirror that is translated back and forth while maintaining parallel to itself. The beam from the movable mirror is also returned to the beam splitter where it, too, is partially reflected back to the source and partially transmitted to the detector. Although the light from the source is incoherent, when it is split into two components by the beam splitter, the components are coherent and can produce interference phenomena when the beams are combined.

Hence FTIR interferogram contains not only the spectral information of the source but also the transmittance characteristics of the sample. The spectral response is calculated from the interferogram using fast Fourier algorithm with help of computer [40]. In our study we have taken one measurement with substrate only as background measurement and the other with the sample. The ratio of the two eliminates the background.

FTIR spectrum was obtained using Perkin Elmer spectrum BX-II spectrometer [41]. In infrared spectroscopy an infrared (IR) radiation is allowed to expose on to the sample surface. Some of the IR radiation was absorbed and rest was transmitted through the sample. The resulting spectrum represents a molecular absorption and transmission versus wave number (cm^{-1}) curve. For each molecular structure absorption is unique which allows us to evaluate the composition analysis of a semiconductor film. In our study FTIR spectrum allows us to evaluate several bonds such as Si-O-Si, Si-H, Si-OH etc. in hydrogenated silicon film on different substrates through their local vibrational mode [42,43]. This spectra yields information about the concentration of impurities, defect incorporated, effective mass, mobility of free carrier, oscillator strength, frequency and damping of optical phonon. An incident infrared photon can ionise the dopant impurity which brings it to any of its excited states, producing one or a series of characteristic absorption peaks. The corresponding peak identification in the absorption and transmission spectrum is performed using standard data chart [44].

3.7.2 Energy Dispersive X-Ray (EDX) Spectroscopy analysis

Electron microprobe method was first described in 1948 [45]. The method is based on interaction of energetic probe electrons, incident on a sample, with the inner shell electrons of the sample. This bombardment with probe electrons causes i) ejection of electrons from one of the inner atomic shells in the sample and ii) allows electrons from higher atomic shell dropping into the vacancies created by the ejected electrons. The transition from the higher atomic shell to inner shell is accompanied by emission of photon whose energy is in the x-ray regime. If the X-ray emission is the result of an L to K shell transition, the X-rays are known as Kα, If the X-ray emission is the result of an M to L shell transition, the X-rays are known as Lα and so on [46,47].

The emitted X-rays from the sample have energies characteristic of the element from which they originate, leading to elemental identification. An appropriate X-ray detector can be used to detect the characteristic X-ray spectrum from the sample [48]. Elemental identification can be performed by matching the experimental spectrum to known X-ray energies which is automatically done using appropriate software.

In our study we have used Oxford EDX system with 10 mm silicon drift X-ray detector (SDD) for composition analysis of silicon film [15]. We have used an electron beam of 20 keV as excitation source. Intensity versus photon energy curve allows us to evaluate the elemental analysis of intrinsic as well as impurity doped silicon film on several substrates. We have detected silicon, phosphorous, nickel, tungsten, tin etc, using EDX spectrum. Peak position are analysed corresponding to B is 185eV (Kα), C is 282eV (Kα), O is 523eV (Kα), Si is 1.83KeV (Kα), P is 2.10keV (Kα), Sn is 3.4keV (Lα), Ti is 4.5keV (Kα), Ni is 7.4keV (Kα), and W is 8keV (Lα) [49,50].

3.7.3 TOF-SIMS analysis

To evaluate the concentration of phosphorous and boron impurities, we have used PHI nano TOF II time of flight secondary ion mass spectrometry (TOF-SIMS) [51]. The detection of secondary ions are carried out using a mass analyzer based on the principle that these ions are accelerated into a flight tube by a 3 kV energy but different masses travel with different velocity to the detector. So the lighter masses reach the detector earlier than the heavier masses [52]

$$\frac{mv^2}{2} = qV \quad (3.8)$$

Here, v is ion velocity, m is mass of ion, q is charge of ion, V is acceleration voltage.

$$\frac{m}{q} = \frac{2Vt_t^2}{L^2} \quad (3.9)$$

Here, L is the path length, t_t is transition time.

Measuring the exact flight duration, ions are separated by the time of flight analysis from which a mass spectrum is generated. This is known as time of flight secondary ion mass spectroscopy (TOF-SIMS) which allows us to evaluate the trace elements in semiconductors and thin films [53,54,55]. This process uses a gallium liquid metal ion gun (LMIG) to generate secondary ions by sputtering the top surface slowly to be analysed [56]. Here we have used caesium and oxygen as source of primary ion which improve the secondary ion yields [57,58]. This is a surface sensitive analytical method that uses a pulsed ion beam to remove molecules from the outer most surface of sample. The particles are then accelerated into a flight tube and their mass is determined using a mass spectrometer by measuring the exact time at which they reach the detector. A mass spectrum is recorded.

In this case Caesium (Cs) beam used to sputter sample surface for phosphorous ion detection and oxygen (O_2) beam used to sputter sample surface for boron detection with energy of 3000V for 20 sec in each step. Gallium (Ga) beam with energy of 15 kV known as liquid metal ion gun (LMIG) used for secondary ion generation from the sample surface for 60 sec in each step known as analyzing time.

All the beams have x-y raster size over a variable acquisition area varied from 100μm to 600μm depending upon the thickness of the film for depth profiling. For a thin layer the raster size is increased so large surface area can be sputtered while keeping the ion beam on most of the top surface. Increasing the sputtering duration will allow more ions to be generated which allow better detection. In case of a thick sample we can reduce the raster size so the ion beam will keep sputtering the small region which allows the beam to sputter more ion from the depth on the sample. For sample with lower impurity concentration can be detected by allowing the analyzer beam to analyze for longer duration. We have used negative mode to detect phosphorous ion and positive mode to detect boron ion.

Depth profile was obtained by measuring the total crater depth with a surface stylus profiler. Duration of analysis was deducted from total time to calculate actual sputtering duration for evaluate depth profile.

Calibration of TOF-SIMS was performed using phosphorous and boron doped samples prepared by ion implantation/diffusion in order to convert the ion count to ion concentration [59].

3.8 Optical properties

3.8.1 UV-VIS-NIR spectrum

Spectrometer is an instrument which consists of a monochromator in-between the light source and the sample, for wavelength dependent measurements such as absorption/transmission, photoconductivity, and photoluminescence. Monochromator is used to separate white light into its spectral components for a subsequent spectral response measurement. Spectrometer is more commonly used when the light is emitted from the sample. Using appropriate size of slit one can vary the illumination area on the sample. The reflected/transmitted light collected using an integrating sphere which also allows diffused light from the sample surface. The silicon/germanium detector detects the light and transmitted to the lock in amplifier. A chopper synchronized the signal from the sample and the light source which is filters the electrical noise. For greater sensitivity and minimization of atmospheric attenuation, a reference sample placed in the path of reference beam and the light received by the detector is compared to that of the reference [60].

For transmission and reflection spectroscopy we have used a spectrometer from Bentham PVE300 that was capable of recording spectra in the visible range as well as in the near infrared and UV (300 nm to 1100 nm) [61]. The system consists of monochromator, dual light source with Xenon and Quartz Tungsten Halogen (*QTH*) *lamps*, phase-insensitive lock-in amplifier, chopper, current pre-amplifier, integrating sphere for reflectance/transmittance measurements and silicon/germanium detectors for calibration.

The transmission measurements were limited for Si/SiO_2 and Nickel substrate for their high absorption coefficient. So only the absorption coefficient of films on sapphire and TiO_2 substrates were calculated. The setup was having an integrating sphere thus the

spectrometer did not measure the absolute values but compared the signal from the sample to a reference beam. Transmission and reflection data were not taken on the same spot of the sample as substrate has to be replaced on the other side of the integrating sphere.

3.8.2 Absorption coefficient and optical band gap calculation

We derived the absorption coefficients from the transmission and reflection measurements. We have used the following approximation formula [62].

$$\alpha = -\frac{1}{d}\ln\left[\frac{T}{(1-R)}\right] - - - - - - - - (3.10)$$

Here α is absorption coefficient, d is thickness of film, T is amount of transmitted light and R is amount of reflected light.

Optical band gap was determined from lnα versus photon energy plot. The intercept after extrapolation of these plots (straight line) on the energy axis reflects optical band gap (E_g) of the semiconductor [63].

3.9 Electrical properties

3.9.1 Four point probe

Four probe setup is commonly used to measure resistivity of semiconductor film as the arrangement eliminates the resistance from wires and contacts. Resistivity calculation for thick silicon sample using four point probe is given by following equation [64].

$$\rho = 2\pi s F \frac{V}{I} - - - - - - - - (3.11)$$

Here, s is equal probe spacing, F is correction factor which depends on sample thickness, diameter, temperature, V is voltage and I is current.

For thin film samples, with thickness t is smaller than the probe spacing, s,

$$\rho = 4.532\, t\, \frac{V}{I} - - - - - - (3.12)$$

Sheet resistivity can be calculated from

$$R_{sh} = 4.532\frac{V}{I} - - - - - - - - (3.13)$$

In this study we have used four point probes apparatus by Lucas-Signatone [65] to determine sheet and bulk resistivity of the intrinsic, phosphorous and boron doped silicon film as well as for laser annealed phosphorous doped i-poly silicon films on Si/SiO_2, sapphire and glass substrate. The four tungsten carbide probes are spaced by 1.016 millimetre with probe tip radius of 40.64 microns. The applied pressure was kept 45 grams. A Keithley 2400 [66] series meter was used to record manually I-V data.

3.9.2 Conductivity Activation Energy

Conductivity of semiconductors generally increases with temperature as follows:

$$\sigma(T) = \sigma_0 \exp (-E_A/kT) \text{----------} (3.14a)$$

Where E_A is the activation energy, T is Kelvin temperature, k = 8.6 $\times 10^{-5}$ eV/K is Boltzmann's constant.

Conductivity activation energy may be regarded as the average energy required to add an electron to the conduction band or a hole to the valence band, assuming conductivity change occurs by change in the concentration of electrons/ holes. More specifically it is the energy separation between the conduction band edge E_c and Fermi level E_F (or Fermi level E_F and the valence band edge E_V). In the case of intrinsic poly silicon film the activation energy is half of its band gap as the Fermi level is in the middle of valence and conduction band. In this study an in house built temperature dependent I-V measurement system has been used to evaluate heating and cooling I-V curve. Resistivity calculated from the following equation.

$$\rho = \frac{VA}{IL} - - - - - - - - - - (3.14b)$$

Here, V is voltage, I is current, L is length between two probe contact, Area, A = W×t, W is width of the contact and t is the film thickness.

We have calculated activation energy from the gradient of the cooling curve using the following equation [67,68].

$$E_A = \frac{(lnR_1 - lnR_2)\,k}{\left(\frac{1000}{T_1} - \frac{1000}{T_2}\right)} - - - - - - (3.15)$$

Here, R is resistance measured at different temperatures, T is Kelvin temperature.

Since water vapour and surface conditions can affect the features of the samples, all the measurements were made under vacuum and samples were heated after vacuum chamber pressure dropped to 1×10^{-2} mbar or below shown in figure 3.1. Samples were placed on top of a copper plate that is heated by two bolt heater connected in series embedded within for ensuring uniform heating all over the plate capable of reaching an stable temperature upto 200°C [69].

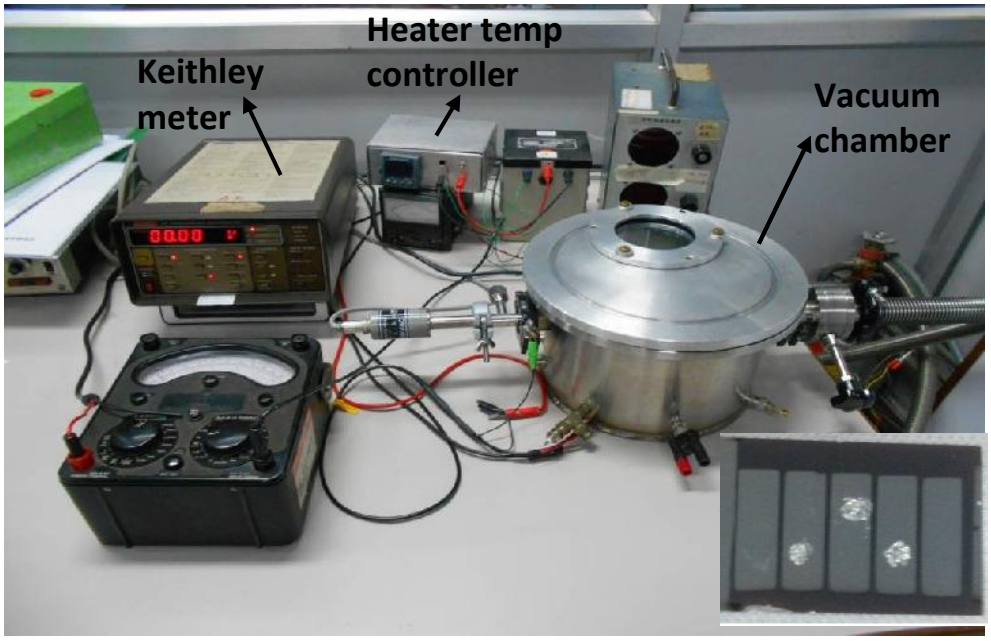

Figure 3.1 Temp dependent dark I-V measurement setup. Inset Al film with indium contact on intrinsic poly silicon thin film on glass substrate.

Temperature dependent I-V measurements can be correct by comparing the heating and the cooling curves. If the temperature of the sample is measured correctly both curves will be the same. If temperature readings have problems, heating and cooling curves will be different, yielding a hysteresis type effect. Indium was used as contact between aluminium

fingers (SiO_2 and Sapphire) or dots (TiO_2) and the tungsten probe to avoid pin hole into the contacts.

Temperature dependent I-V data acquired using this setup for silicon film on several substrates using temperature ranging from room temperature to 140°C. Series of aluminium dots of various diameter starting from 0.5 mm to 2 mm and in some cases 5 mm wide aluminium film with 1mm separation (shown inset figure 3.1) deposited using thermal evaporator to use as top contact for I-V data collection. We have used Keithley source meter to record manually I-V data.

3.9.3 Dark and illuminated I-V curve

The n-i-p structure diode devices were having FTO at the bottom for contact. So the I-V measurements were carried out using two tungsten probes contacts at top and bottom. In this case we have used ABET AAA class [70] one sun simulator for dark and illuminated I-V measurement. 100 nm of Al film were evaporated onto the film using thermal evaporator. Indium was used as contact between aluminium dot and the tungsten probe to avoid pin hole into the Al contacts.

The current of n-i-p device can be written as a function of the diode voltage V_d using following equation [71]

$$I = I_o\left(e^{\frac{qV_d}{nkT}} - 1\right) - - - - - - - - (3.16)$$

Here, I_0 is saturation current, n is diode ideality factor, k is Boltzmann's constant, T is Kelvin temperature.

Considering the series resistance the equation 3.16 can be written

$$I = I_o\left(e^{\frac{q(V-Ir_s)}{nkT}} - 1\right) - - - - - - - - (3.17)$$

Here, V is diode terminal voltage, r_s is series resistance.

Semi log plot of forward bias of this equation 3.17 is named as log (I)-V curve which gives us a non linear curve. Series resistance can be calculated from taking the gradient at high current region according to the equation

$$r_s = \frac{\Delta V}{\Delta I} - - - - - - - - (3.18)$$

3.9.4 Capacitance measurement

The capacitance – voltage technique based on the fact that, the width of reverse bias depletion region of p-i-n/n-i-p junction device depends on the applied voltage. Capacitance of reverse bias junction measured under various bias voltages for n-i-p structure diode using 4284A precession LRC meter from Agilent instrument [72]. In our case we have used two tungsten probes as contact with the device. We have calculated majority carrier concentration at the depletion region, depletion width and resistivity. We also have calibrated LRC meter and the contact arrangement using a standard p-n junction solar cell under dark condition.

Table 3.1 Capacitance versus bias voltage data acquisition of p-n junction solar cell under dark condition using precision LRC meter for calibration of capacitance measurement setup.

Bias voltage (volts)	Capacitance (nano Farad)	$1/C^2$ ($1/F^2$)	Slope $\frac{d}{dv}\left(\frac{1}{C^2}\right)$ ($1/F^2$-V)
0	729	1.88×10^{12}	
-0.1	685	2.13×10^{12}	
-0.2	647	2.38×10^{12}	2.55×10^{12}
-0.3	615	2.64×10^{12}	
-0.4	587	2.9×10^{12}	

Calculations of these standard p-n junction solar cell variables are given below for validating the clarity of the measurement as all the data collected manually. Under reverse bias the depletion width can be calculated from the following equation [73].

$$w = \frac{\varepsilon_s \varepsilon_o A}{C_o} - - - - - - - - - (3.16)$$

$$= \frac{11.7 \times 8.852 \times 10^{-14} \times 16}{729 \times 10^{-9}} = 227nm$$

Here, A is total area of top surface, C_0 is capacitance at zero bias voltage, ε_s is semiconductor dielectric constant, ε_0 is permittivity of free space.

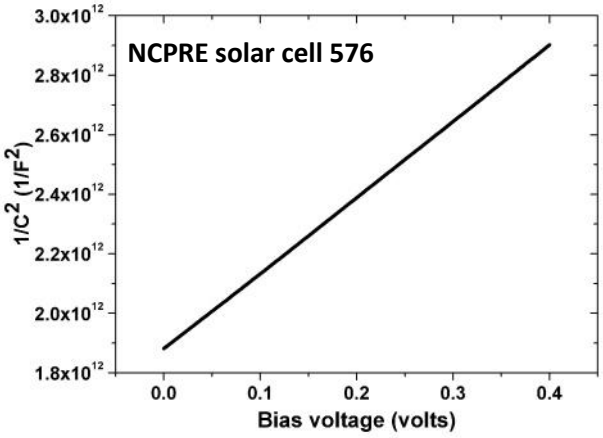

Figure 3.2: Capacitance versus bias voltage plot for evaluation of majority carrier concentration at depletion region of standard solar cell.

Majority carrier concentration at the depletion region can be calculated from the following equation.

$$N_A = \frac{2}{q\varepsilon_s \varepsilon_o A^2 \frac{d}{dv}\left(\frac{1}{C^2}\right)} \text{------(3.17)}$$

$$= \frac{2}{1.6 \times 10^{-19} \times 11.7 \times 8.852 \times 10^{-14} \times 2.55 \times 10^{12} \times 16^2} = 1.8 \times 10^{16} atom/cm^{-3}$$

Here, $\frac{d}{dv}\left(\frac{1}{C^2}\right)$ obtained from the slope of a $1/C^2$ versus V curve shown in figure 3.2.

$$\rho = \frac{1}{qN_A\mu_C} \text{------(3.18)}$$

$$= \frac{1}{1.6 \times 10^{-19} \times 1.8 \times 10^{16} \times 400} = 0.9\ \Omega - cm$$

Here, μ_c is carrier mobility.

3.10 Photocurrent spectral response

Spectral response of intrinsic poly crystalline silicon film in wavelength range of 300 nm to 1100 nm was taken to evaluate the photoconductivity of the film which is also a measure of the light sensitivity of the material. This allows us to evaluate the worthiness of these films for photovoltaic application.

The measure of photoconductivity can be determined by illuminating the sample with one sun illumination (100 mW/cm^2). The ratio of photoconductivity and the dark conductivity is known as photo response [74].

$$photoresponse = \frac{\sigma_{ph}}{\sigma_d} - - - - - - (3.19)$$

Dark conductivity can be calculated from inverse of resistivity equation 3.14, whereas photoconductivity can be calculated from the following equation [75,76].

$$\sigma_{ph} = eG\mu\tau - - - - - - - (3.20)$$

Here, G is the generation rate of the photo carriers in the unit of cm^{-3}s^{-1}, τ is the recombination time measured in seconds, μ is the photo carrier mobility in cm^2/V.s.

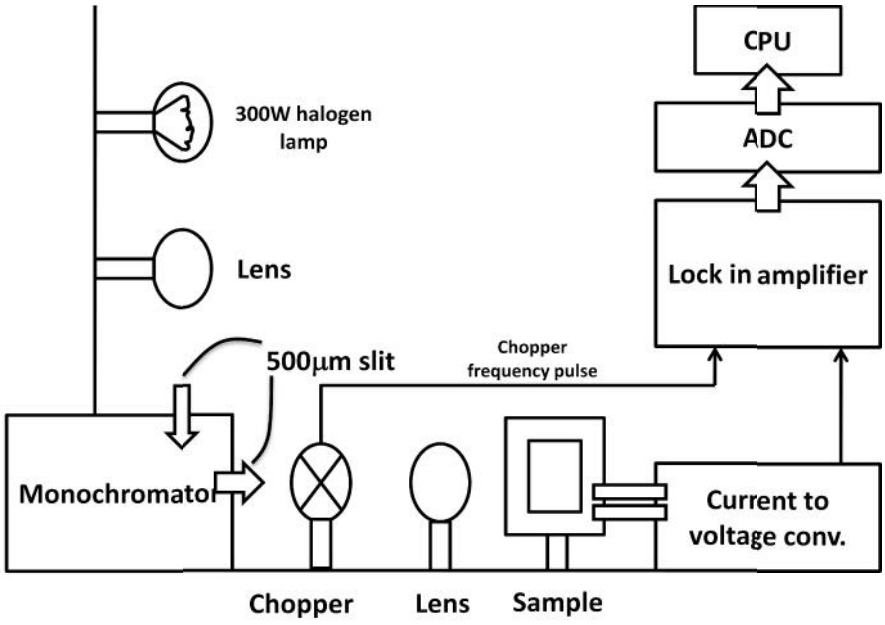

Figure 3.3: Block diagram of photocurrent spectral response measurement arrangement.

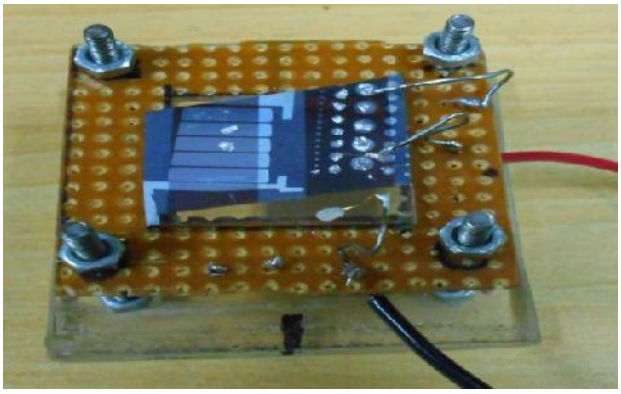

Figure 3.4: Sample stage arrangement with Al contact for photo current spectrul response measurement of intrinsic silicon film on glass substrate.

This room temperature photocurrent measurement was performed using a 300W halogen lamp as light source in a dark room. A monochromator with 500 micron slit width followed by a chopper with frequency 233Hz used to shine light beam of selected wavelength on to the sample. A 63 mm foal length lens used to focus the light. A current to voltage converter from Keithley instrument was used along with lock in amplifier, synchronized by the chopper frequency, to detect the photocurrent. Block diagram of the arrangement is shown in fig 3.3.

3.11 Discussion

We have described various techniques of semiconductor characterization used during the course of this work. These techniques are having well established theory along with their implementation through instrumentation. Due to advance in computation techniques most of the data acquisition process was aided by appropriate software. During every measurement the instrument was calibrated using standard sample for validating the measurement.

Calibration of the optical reflection measurement was performed using a Teflon disk which reflects nearly 100% incident light. Calibration of four probe instrument was performed before each measurement using standard silicon sample. All optical

measurements were performed inside dark room to avoid any additional light source. Surface morphological study using AFM observation during the nucleation growth of silicon thin film allowed us to establish the reaction condition at very early stage of the film growth. SEM study allowed us to observe morphology of thick film with large grain poly crystalline silicon film. TEM study helped us to evaluate the different layer thickness and growth direction. We observed epitaxial growth, polycrystalline silicon columnar growth and amorphous silicon film using X-TEM imaging and electron diffraction.

Study of electrical characterization such as dark, illuminated and temperature dependent I-V curve performed manually. The capacitance and voltage measurement were also taken manually. In both cases we have used standard sample to calibrate he measurement process. Temperature dependant I-V data was taken quickly, so the temperature change is small during the data acquisition. An uncertainty of $\pm 1^{\circ}C$ temperature change observed during data acquisition.

3.12 References

[1] www.bruker.com/products/ surface- analysis/ stylus- profilometry/ dektak- xt / overview.html

[2] H. Anders, Thin Films in Optics, The Focal Press, London, 1967.

[3] http://www.filmetrics.com/ thicknessmeasurement

[4] W.R. Runyan and T.J. Shaffner, Semiconductor Measurements and Instrumentation, McGraw Hill, New York, 1997.

[5] B.L. Sopori, Y. Zhang, W. Chen, and J. Madjdpour, "Silicon solar cell process monitoring by PV Reflectometer," *IEEE PVSC, Anchorage, AK, Sept, 2000.*

[6] Bhushan Sopori, U. S. Patent No. 6,275,295.

[7] P. Burggraaf, "How Thick Are Your Thin Films?", Semicond. Int.11, 96–103, Sept. 1988.

[8] J.R. Sandercock, "Film Thickness Monitor Based on White Light Interference", J. Phys. E: Sci. Instrum.16, 866–870, Sept. 1983.

[9] Q. Zhong, D. Inniss, K. Kjoller, and V.B. Elings, "Fractured Polymer/Silica Fiber Surface Studied by Tapping Mode Atomic Force Microscopy," Surf. Sci. Lett. 290, L668–L692, 1993.

[10] M. A. Lantz, S. J. O'Shea, and M. E. Welland, Phys. Rev. B 56, 15345, 1997.

[11] D. Maugis, J. Colloid Interface Sci. 150, 243, 1992.

[12] http://www.cen.iitb.ac.in/cen/online_modules/equipmentslist.php

[13] G. Meyer and N.M. Amer, "Novel Optical Approach to Atomic Force Microscopy", Appl. Phys.Lett.53, 1045–1047, Sept. 1988.

[14] Dieter K. Schroder, 'Semiconductor Material and Device Characterization", Third Edition, Copyright, 2006, John Wiley & Sons, Inc. page 545.

[15] http://www.zeiss.com/ microscopy/ en_de/ products/ scanning- electron-microscopes

[16] T.E. Everhart and R.F.M. Thornley, "Wide-Band Detector for Micro-Microampere Low-Energy Electron Currents,"J. Sci. Instrum.37, 246–248, July 1960.

[17] http://eqdb.nrf.ac.za/equipment / microscope/ philips-cm200 -transmission- electron-microscope -tem- electron-microscopes.

[18] J.C.H. Spence, Experimental High-Resolution Electron Microscopy, 2nd Ed., Oxford University Press, New York, 1988.

[19] D. Cherns, "High-Resolution Transmission Electron Microscopy of Surface and Interfaces in Analytical Techniques for Thin Film Analysis (K.N. Tu and R. Rosenberg, eds.), Academic Press, Boston, 1988, p-297–335.

[20] Dieter K. Schroder, 'Semiconductor Material and Device Characterization", Third Edition, Copyright, 2006, John Wiley & Sons, Inc. page 646.

[21] T. Wilson and C.J.R. Sheppard,Theory and Practice of Scanning Optical Microscopy, Academic Press, London, 1984; T. Wilson (ed.),Confocal Microscopy, Academic Press, London, 1990.

[22] T.R. Corle and G.S. Kino,Confocal Scanning Optical Microscopy and Related Imaging Systems, Academic Press, San Diego, 1996.

[23] Dieter K. Schroder, 'Semiconductor Material and Device Characterization", Third Edition,Copyright, 2006, John Wiley & Sons, Inc. page 571.

[24] www.zeta-inst.com/products/true-color-3D-optical-profiler

[25] www.olympus-ims.com/ja/microscope/mx61l/

[26] Dieter K. Schroder, 'Semiconductor Material and Device Characterization", Third Edition, Copyright, 2006, John Wiley & Sons, Inc. page 566.

[27] www.rigaku.com/en/products/xrd/smartlab

[28] Cullity B.D, "Elements of X-ray diffraction", Addison-Wesley publishing company Inc., Massachusetts, 1956, page 85-88.

[29] C.V. Raman and K.S. Krishna, "A New Type of Secondary Radiation," Nature 121, 501–502, March 1928.

[30] Dieter K. Schroder, 'Semiconductor Material and Device Characterization", Third Edition, Copyright 2006 John Wiley & Sons, Inc. page 609.

[31] D.A. Long, Raman Spectroscopy, McGraw-Hill, New York, 1977.

[32] G.H. Loechelt, N.G. Cave, and J. Men´ endez, "Measuring the Tensor Nature of Stress in Silicon Using Polarized Off-Axis Raman Spectroscopy,"Appl. Phys. Lett.66, 3639–3641, June 1995.

[33] www.horiba.com/ scientific/ products /raman- spectroscopy/ raman- spectrometers / raman- microscopes /hr-evolution /labram-hr-evolution-17309/

[34] www.witec.de/products/raman/alpha300-r-confocal-raman-imaging/

[35] http://www.advancedphotonicsindia.com/?product_cat=lasers

[36] www.princetoninstruments.com/products/spec/actonseries/dsheet.aspx

[37] Dieter K. Schroder, 'Semiconductor Material and Device Characterization", Third Edition, Copyright 2006 John Wiley & Sons, Inc. page 605.

[38] K.K. Smith, "Photoluminescence of Semiconductor Materials" Thin Solid Films84, 171–182, Oct. 1981.

[39] P.R. Griffith and J.A. de Haseth,Fourier Transform Infrared Spectrometry, Wiley, New York,1986.

[40] J.W. Cooley and J.W. Tukey, "An Algorithm for the Machine Calculation of Complex Fourier Series,"Math. Comput.19, 297–301, April 1965.

[41] www.perkinelmer.com/Catalog/Category/ID/FTIR%20FTNIR%20Spectrometers

[42] J.R. Ferraro, K. Krishnan (eds.), Practical Fourier Transform Infrared Spectroscopy, Acad. Press, San Diego (1990)

[43 L.L. Kazmerski, Proc. Mat. Res. Soc. Symp. Proc. Vol. 106 (1987) 199-211

[44] Gracin, D., Radic. N., Desnica U.V., Andreic Z., Balzar D., Thermal stability of amorphous silicon–carbon alloys deposited by magnetron source. Fizika A 4 (2), 329–335, 1995.

[45] R. Castaing, Thesis, Univ. of Paris, France, 1948; "Electron Probe Microanalysis," inAdv. In Electronics and Electron Physics(L. Marton, ed.), Academic Press, New York,13, 317–386, 1960.

[46] K.F.J. Heinrich,Electron Beam X-Ray Microanalysis, Van Nostrand Reinhold, New York, 1981.

[47] Dieter K. Schroder, 'Semiconductor Material and Device Characterization", Third Edition, Copyright 2006 John Wiley & Sons, Inc. p640, 2006.

[48] D.E. Newbury, "Electron Probe Microanalysis in Metals Handbook, 9th Ed. (R.E. Whan, coord.), Am. Soc. Metals, Metals Park, OH, 10, p516–535, 1986.

[49] Abmann A. and Wendt M. Spectrochim. Acta 58, p711–716, 2003.

[50] www.edax.com

[51] www.phi.com/surface-analysis-techniques/tof-sims.html

[52] Dieter K. Schroder, 'Semiconductor Material and Device Characterization", Third Edition, Copyright 2006 John Wiley & Sons, Inc. p656-658, 2006.

[53] M. Guilhaus, "Principles and instrumentation in time of flight mass spectrometry, physical and instrumental concepts", Journal of Mass Spectrometry, vol. 30, no. 11, pp. 1519–1532, 1995.

[54] M.A. Douglas and P.J. Chen, "Quantitative Trace Metal Analysis of Si Surfaces by TOF-SIMS" Surf. Interface Anal. 26, 984–994, Dec. 1998.

[55] M.T. Bernius and G.H. Morrison, "Mass Analyzed Secondary Ion Microscopy," Rev. Sci. Instrum. 58, 1789–1804, Oct. 1987.

[56] A. R. Bayly, A. R. Waugh and K. Anderson, 'SIMS micro-analysis with a gallium ion micro probe'. Nuclear Instruments and Methods In Physics Research, vol. 218, no. 1-3, pp. 375–382, 1983.

[57] L. B. Li, D. S. McPhail, N. Yakovlev, and H. Seng, "Strategies for improving the sensitivity of FIB-SIMS," Surface and Interface Analysis, vol. 43, pp. 495–497, 2011.

[58] D.S. McPhail, L.B. Li, R.J. Chater, N.Yakovlev, and H. Seng, "From FIB-SIMS to SIMS-FIB. The prospects for a 10 nm lateral resolution SIMS instrument with full FIB functionality", Surface and Interface Analysis, vol. 43, pp. 479–483, 2011.

[59] A. Benninghoven, F. G. R üdenauer, and H. W. Werner, "Secondary Ion Mass Spectrometry: Basic Concepts, Instrumental Aspects, Applications, and Trends, Wiley, New York, 1987, 1227 pages.

[60] Dieter K. Schroder, 'Semiconductor Material and Device Characterization", Third Edition, Copyright 2006 John Wiley & Sons, Inc. page 588.

[61] www.bentham.co.uk/solcell.htm

[62] Swanepoel R., J. Phys. E: Sci. Instrum., 16 (1983), 1214.

[63] MOTT N.F., GURNEY R.W., Electronic Processes in Ionic Crystals, Oxford Univ. Press, London, 1940.

[64] Dieter K. Schroder, 'Semiconductor Material and Device Characterization", Third Edition, Copyright 2006 John Wiley & Sons, Inc. page 6-11.

[65] www.signatone.com/applications/4ptprobe.asp

[66] www.keithley.com/products/dcac/currentvoltage/2400smu

[67] H. Fritzsche, Journal of Non-Crystalline Solids, 49, 62, 1971.

[68] Y. Lubianiker and I. Balberg, Phys. Rev. Lett. 78, p. 2433, 1997.

[69] Sevilay Ugur, Merih Serin, Tr. J. of Physics, Turkey, 22, 511-517, 1998.

[70] abet-technologies.com/solar-simulators/sun-3000-class-aaa/

[71] Dieter K. Schroder, 'Semiconductor Material and Device Characterization", Third Edition, Copyright 2006 John Wiley & Sons, Inc. page 186.

[72] www.keysight.com/en/pc-1000000391%3Aepsg%3Apgr/lcr-meters-impedance-measurement-products?nid=-536902441.0&cc=BD&lc=eng

[73] J. Hilibrand and R.D. Gold, "Determination of the Impurity Distribution in Junction Diodes from Capacitance-Voltage Measurements," RCA Rev.21, 245–252, June 1960.

[74] Bube R H. Photoelectronic properties of semiconductors. Cambridge: Cambridge University Press, 1992.

[75] Kakinuma H. Fermi-level-dependent mobility-lifetime product in a-Si:H. Phys Rev B, 39: 10473, 1989.

[76] Singh J, Shimakawa K. Advances in amorphous semiconductors. London, New York: Taylor & Francis Group, 250, 2003.

Chapter 4

Synthesis of intrinsic silicon film

4.1 Introduction

One of the most promising technologies for cost reduction in fabricating photovoltaic cells involves the use of polycrystalline and amorphous silicon films. Synthesis of these films requires low temperature. Films can be grown on foreign substrates such as low cost glass. In order to grow crystalline silicon films on foreign substrates, different strategies have been adopted by different workers. One early approach was solid phase crystallization by thermal annealing of amorphous silicon on glass below 600°C [1]. Refinements of this technique include metal induced crystallization and aluminium induced layer exchange [2], which cut down the crystallization time substantially. A variant of thermal annealing uses laser crystallization of amorphous silicon [3,4]. A method of synthesizing nearly epitaxial silicon on foreign substrates interposes buffer layer between the substrate and the silicon layer. Buffer layers such as CeO_2 and MgO have been used [5,6]. These are textured using ion beam assisted deposition. We decided to synthesize oriented silicon on foreign substrates without using the buffer. Our approach is based on the work of Vallat-Sauvain et al [7] who showed preferential PECVD deposition of oriented grains of silicon on glass by controlling the dilution of silane with hydrogen.

This chapter describes the strategies we have followed in order to synthesise intrinsic polycrystalline and amorphous silicon films using HWCVD techniques. Growth on several substrate types was investigated to explore the effect of the nature of the substrate on the crystallinity of the grown silicon film. Substrates used in this work include i) oxidized silicon wafer (Si/SiO_2), ii) TiO_2 coated glass, iii) alkali free borosilicate glass, iv) nickel-

tungsten alloy metal strip and v) polished sapphire. We have also included in the growth sequence steps to improve the material quality using hydrogen passivation and capping the growth with a-Si:H layer. Several characterization techniques were used throughout the synthesis process. We have performed a series of experiments during our study and only the representative results are discussed here.

4.2 Substrates

For synthesizing high quality intrinsic silicon films, we need good quality substrates. As mentioned above, we have used five different substrates for the synthesis of intrinsic poly silicon films. Most of the work has been done using alkali free borosilicate Corning 7059 glass substrates. For some experiments involving FTIR measurements on silicon films deposited on glass (glass is opaque to infra-red), Si/SiO_2 substrates were prepared by oxidizing two inch (100) silicon wafers using a wet oxidation. Titanium dioxide (TiO_2) substrates were (112) oriented anatase, prepared by atmospheric chemical vapour deposition (ACVD) techniques, on Indium tin oxide (ITO) coated glass, synthesized at Washington University [8]. Following up on the work of Findikoglu et al [5], we have used nickel - 5% tungsten (Ni-W) metal tape textured with dominant (002) orientation obtained from Evico [9] as metal substrate. In addition to these we did some experiments using c-axis oriented both sides polished sapphire (Al_2O_3) substrates [10]. Other details of the preparation of substrates and cleaning procedure are discussed in Appendix II.

4.3 Growth process

The growth of silicon in a hot wire CVD system results from dissociation of SiH_4 and H_2 coming in contact with hot tungsten filament at 1900°C. Dissociation of SiH_4 produces Si and H atoms near the filament. As Si atoms move towards the substrate, they react with SiH_4 and produce mainly Si_2H_2 growth radicals [11,12].

$$Si + SiH_4 \rightarrow H_2 + Si_2H_2$$

At the substrate surface, Si_2H_2 breaks up and results in the growth of silicon. The net growth rate decreases with increasing H partial pressure, due to etching of growing silicon by atomic hydrogen generated during the process.

4.3.1 Nucleation

The first step for the synthesis of crystalline silicon films is nucleation. Without proper nucleation, polycrystalline silicon films will have grains randomly oriented in (111), (220) and (311) directions as in fine grain silicon powder. On the other hand, epitaxial film growth has a single orientation for the entire surface of the film. For solar cell application, it is desirable to synthesize crystalline silicon film comprising of grains preferentially oriented along a crystallographic direction. This requires growth of nuclei having preferential orientation. Vallat–Sauvain [7] showed that the silicon grains synthesized by PECVD, using a dilute mixture of silane with hydrogen, develop preferential (220) orientation for certain ratio of SiH_4 / H_2 precursors as shown in the Figure below from [7].

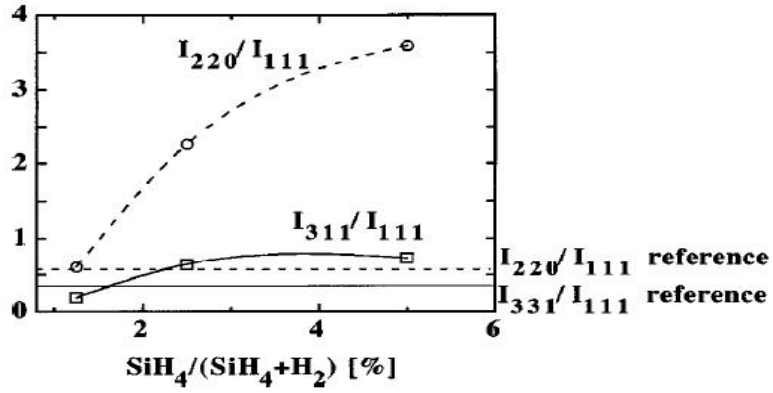

Figure 4.0: Ratio of silane-hydrogen mixture versus ratio of X-Ray diffraction peak intensities for the evaluation of preferred crystalline orientation.

In this figure, the reference lines correspond to the ratio of intensities of (220) and (311) XRD lines with respect to the intensity of (111) line for standard silicon powder. High value of the I_{220} / I_{111} ratio is taken to be the development of (220) preferred orientation of the grains. As seen, mixture of 95 % hydrogen + 5 % silane produces grains strongly oriented along (220) direction. We have used this mixture during the nucleation stage of growth.

All nucleation experiments were performed with base pressure of no higher than 2.5×10^{-6} mbar before initiating growth process. The overnight pressure in the growth chamber was 1.7×10^{-2} mbar which guarantees integrity of the system. Working pressure in the growth chamber was maintained below 1.1×10^{-1} mbar during the growth process. Hydrogen flow was adjusted in order to maintain the chamber pressure below this limit. The duration of deposition was maintained using a translatable shutter which covers the sample box. The shutter also allowed us to cover the sample during dummy run performed just prior to the actual growth process for conditioning the growth chamber. This dummy run

performed with sample shuttered and kept at 400°C, filament at 1900°C and flow of mixture of 1 sccm of pure silane (SiH_4) and 20 sccm of pure hydrogen (H_2) for 10 minutes. This dummy run covers the inner surface of the reaction chamber with approximately 200 nm intrinsic silicon layer. In this way we have avoided any contamination from the filament and the inner surface of the reaction chamber during the actual growth. Table 4.1 lists the experiment done to establish the growth conditions for silicon nucleation.

Table 4.1: Nucleation stage of intrinsic poly silicon thin films on Si/SiO_2 and glass substrates.

Sample name	Exp No.	Process Pressure in mbar	Substrate temp. in °C	Filament temp. in °C	Gas flow in sccm H_2 : SiH_4	Deposition duration in Sec	Thickness in nm
Si/SiO_2 Glass	17	6.8×10^{-2}	400	1900	20 : 1	100	20

4.3.2 Epitaxial growth

After the nucleation of oriented grains, a continuous silicon film is formed by lateral growth of the nuclei by incorporating silicon atoms, resulting from the breaks up of the gas phase species Si_2H_2 attached to the surface, having sufficient surface mobility. For high surface mobility of the silicon atoms to promote oriented growth / epitaxy, the substrate temperature has to be raised to about 600°C [1]. Higher than this temperature causes the glass substrate to be soften and deformed which we have discussed in the chapter 6, section 6.4.1.

Growth of epitaxial silicon films of thickness in the range 200-300 nm was investigated on Si/SiO_2, sapphire, glass/TiO_2, nickel and glass substrates by HWCVD at substrate temperatures ranging from 500°C-600°C. The temperature was ramped up after the nucleation stage. The flow of hydrogen was maintained at 20 sccm while and silane was ramped up (from 1 sccm during the nucleation stage) gradually from 1 sccm to 8 sccm in multiple stages as shown in Table 4.2. The total deposition duration for each stage was 100 sec. The ramp up of silane flow took around 10-15 sec and it took similar time stabilize the flow. So the duration of growth in stabilized flow will be less than 100 sec in each step. We have not measured the thickness of the film separately after each ramp up step. An

approximate estimate is that growth rate increases from about 2 A° /sec with 20 sccm H_2 : 1 sccm SiH_4 to about 20 A° /sec with 20 sccm H_2 : 8 sccm SiH_4 .

It was noticed that the reactor pressure shoots up above 0.1 mbar during these high flows. In order to keep chamber pressure below 0.1 mbar, we have reduced the hydrogen flow gradually from 20 sccm to 15 sccm, while the maximum silane flow was limited to 5 sccm. Under this condition, the chamber pressure was about 6.5×10^{-2} mbar and the deposition rate of silicon was estimated to be about 10 A° /sec. The crystalline nature of the film grown during this step is determined from the TEM imaging and electron diffraction measurements described in section 4.4.3.

Table 4.2: Growth of epitaxial intrinsic poly silicon films on Si/SiO_2, Sapphire, $Glass/TiO_2$, Nickel and Glass substrates.

Exp. No	Sample name	Process Pressure in mbar	Substrate temp. in °C	Filament temp. in °C	Gas flow H_2:SiH_4 in sccm	Deposition duration in Sec
4	10_Si/SiO_2 11_$Glass/TiO_2$ 12_ Al_2O_3 13_Ni-W	1.2×10^{-1} to 5.3×10^{-1}	480-500	1885–1900	20 : 1 20 : 2 20 : 4 20 : 8 20 : 12	500
5	14_$Glass/TiO_2$ 15_Si/SiO_2 16_ Al_2O_3 17_Ni-W	1.2×10^{-1} to 6.7×10^{-1}	530-550	1883-1900	20 : 1 20 : 2 20 : 4 20 : 8 20 : 12	500
6	19_$Glass/TiO_2$ 20_ Al_2O_3 21_Si/SiO_2 22_Ni-W	1.3×10^{-1} to 3.8×10^{-1}	530-550	1850-1900	20 : 1 20 : 1.5 20 : 2 20 : 3 20 : 5	500
17	49_Glass 54_Glass 56_Glass 82_Glass	7.4×10^{-2} 6.2×10^{-2} 6.5×10^{-2}	600	1850-1900	20 : 1.5 18 : 2 17 : 3	300

4.3.3 Thickening stage

Intrinsic silicon layer will be the absorber layer of n-i-p structure device. Film thickness will play an important role in this case. We have been able to grow films up to 5 micron thick at a very fast rate. As listed in Table 4.3, under the conditions used for very

high growth rates (high SiH_4 flow and high chamber pressure), the films develop considerable tensile strain and in several instances, film lifts off from the substrate. As such the quality of these films is uncertain. To overcome this problem, we have reduced the silane flow from 15 sccm to 5 sccm and hydrogen flow to 15 sccm. With these flows, the chamber pressure could be maintained below 0.1 mbar. This does reduce the growth rate to about 10 A° / sec, but films are more stable and have improved in quality.

Table 4.3: Growth of thick intrinsic silicon film on Si/SiO_2, Sapphire, $Glass/TiO_2$, Nickel and glass substrates.

Sample Name	Exp. No	Process Pressure in mbar	Substrate temp. in °C	Filament temp. in °C	Gas flow H_2:SiH_4 in sccm	Deposition duration in Sec	Total film Thickness in nm
$Glass/TiO_2$	4	7.0×10^{-1}	500	1830-1900	20 : 15	1000	3600
Al_2O_3	5	6.7×10^{-1}	550	1838-1922	20 : 15	1000	4900
Si/SiO_2 Ni-W	6	3.8×10^{-1}	550	1850-1900	20 : 8	1000	2400
Glass	17	6.5×10^{-2}	600	1893-1900	15 : 5	1000	1300

4.3.4 Surface passivation

Passivation with atomic hydrogen improves the material quality by reducing the number of broken and dangling bonds in the bulk of the film [13]. As shown above, the optimum condition for thick intrinsic layer growth was found to be 75 % hydrogen dilution. As such, the as grown film will have significant density of defects. In order to reduce this defect density, passivation was performed at the end of the growth process. Intrinsic silicon film grown on glass substrate was chosen for this purpose. We have done H_2 soaking of the film under hot filament during cooling the sample from growth temperature to a lower substrate temperature of 200°C for about 45 min.

This stage of hydrogen passivation improves the material quality by reducing the broken and dangling bonds which we would discuss in the photo response and photoluminescence study in this chapter in section 4.4.11 and 4.4.12 respectively.

4.3.5 Top passivation layer

Thin top layer of amorphous intrinsic silicon was grown at 200 °C under varying gas flow combination and duration shown in table 4.4. This top layer forms a junction with the intrinsic poly silicon layer while allowing maximum amount of light to reach the absorber layer. This layer should be capable of driving out the photo generated carriers with minimum recombination loses while transporting them to the outer circuit with minimum electrical resistance [14]. We have reduced the thickness of top layer as thin as 3 nm. The layer thickness was determined using cross section transmission electron microscope which we would discuss in this chapter in the section 4.4.3.

Table 4.4: Growth of amorphous silicon thin intrinsic top layer on top of intrinsic poly crystalline silicon film.

Sample name	Exp no	Process Pressure in mbar	Substrate temp. in °C	Filament temp. in °C	Gas flow H_2:SiH_4 in sccm	Deposition duration in Sec	Film Thickness in nm
39_Si/SiO_2	24	9.9E-2	200	1880-1905	20 : 2.5	30	40*
96_Si/SiO_2	27	6.8E-2			20 : 2.5	25	30*
99_Glass	29	6.7E-2			20 : 1	15	6**
104_glass	30	6.7E-2			20 : 1	8	3**

***** From cross section TEM image

******Estimated from the previous cross section TEM image

4.4 Results

Results represented in sections 4.4.1 to 4.4.4 are concerned with the topographical characterization of intrinsic poly crystalline silicon film using profilometer, atomic force microscope, scanning electron microscope, cross section transmission electron microscope and scanning electron microscope. X-ray diffraction measurements (section 4.4.5) are performed for evaluation of crystalline orientation of intrinsic poly silicon film. Crystalline fraction determined using confocal Rama Spectroscopy and Raman imaging (section 4.4.6). Electrical characterization (resistivity measurement) is performed from room temperature to

125°C and activation energy is determined (sec 4.4.7). Optical reflectance and transmission measurements have been performed using UV-VIS-NIR spectrometer (section 4.4.8). Photocurrent and photoluminescence measurement was performed for the evaluation of photo response and defects incorporated within the film respectively. We have also performed Fourier transforms infrared spectroscopy to observe impurities through their local vibrational mode. Energy dispersive X-ray analysis performed for the evaluation of the atomic percentage of oxygen, carbon and other substrate materials.

4.4.1 Thickness analysis

Thickness and roughness of intrinsic poly crystalline silicon film was measured using stylus profilometer. Typical profilometer traces showing step height and roughness of four samples of HWCVD grown silicon films are shown in figure 4.1. The growth conditions and thickness data corresponding to these have been tabulated in the Table 4.3. In our study we observed that the thickness of silicon film increases with the increase of silane concentration for the same growth duration.

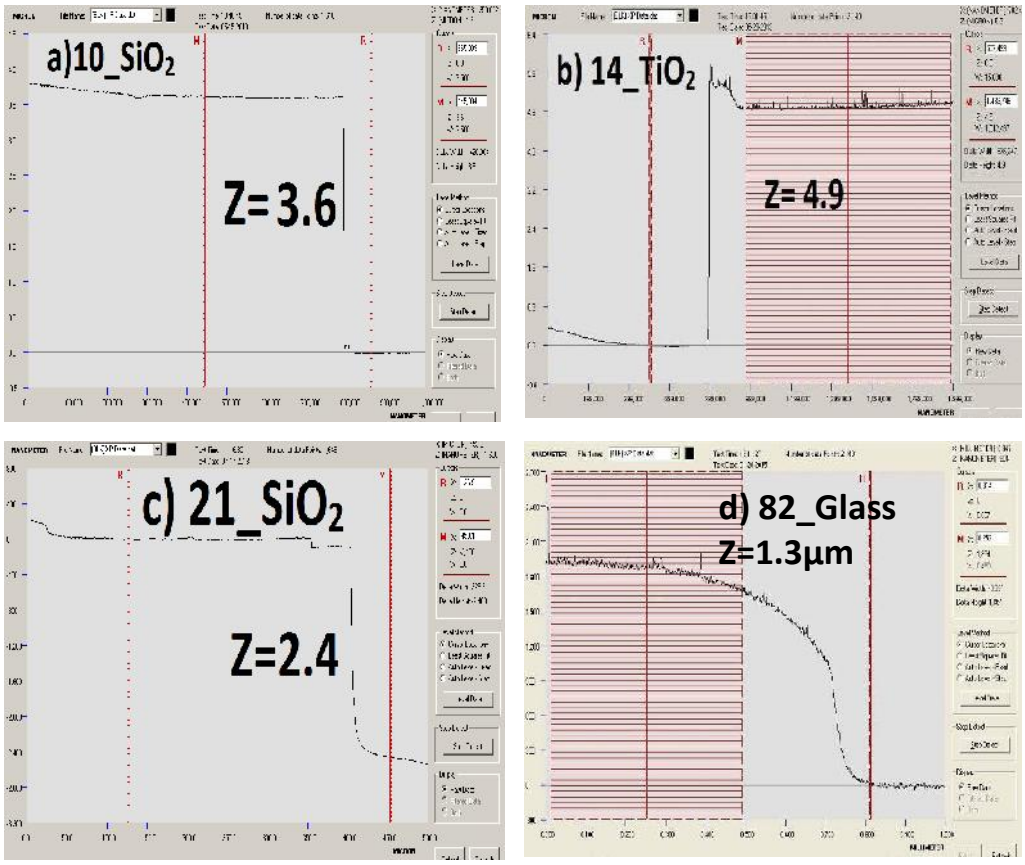

Figure 4.1: Stylus surface profiler step height measurement of silicon film on a) Si/SiO_2, b) TiO_2 c) Si/SiO_2 and d) Glass substrate.

The roughness of silicon film on Si/SiO_2 substrate is around 10 nm whereas on $Glass/TiO_2$ substrate roughness is around 200 nm. This TiO_2 layer is grown on glass substrate which contributes to the larger roughness of the film. Roughness of silicon film on glass substrate is around 100 nm. Hence we can conclude that the roughness of silicon film on glass substrate is also from the contribution of glass not from the growth process.

Knowing the total duration of growth we have estimated average growth rate tabulated in Table 4.5 for each growth condition. Higher growth rate is suitable for low cost fabrication on the other hand this also degrades the material quality. We had to decrease the growth rate from 2 nm / sec to 1.4 nm / sec in order to achieve well passivated intrinsic silicon film. For the device fabrication we have decreased the growth rate further to $0.9nmsec^{-1}$ which we would discuss in the chapter 7.

Table 4.5: Growth duration, thickness and average growth rate of intrinsic poly crystalline silicon film grown on Si/SiO_2, TiO_2 and glass substrate using HWCVD.

Exp no	Substrate name	Total growth duration in sec	Thickness in nm (From fig-4.1)	Average growth rate in nm/sec
4	10_Si/SiO_2	1740	3600	2
5	14_Glass/TiO_2	1740	4900	2.8
6	21_Si/SiO_2	1720	2400	1.4
17	82_Glass	1460	1300	0.9

4.4.2 Atomic force microscope (AFM) image analysis

AFM image allows us to observe the nucleation of intrinsic silicon thin film at the very early stage of HWCVD growth. Crystalline grain size, nucleation density and shape were evaluated using tapping mode atomic force microscopy shown in figure 4.2. We observed an increase in atomic hydrogen (H_2) dilution leads to an increase in grain size. As we further approach to decrease the H_2 dilution to increase the growth pressure, the grain size decreased. A decrease in H_2 dilution leads to decrease the process pressure from 3 mbar to

2 mbar which was not expected as higher growth pressure will reduce the free path for atoms and this will cause non uniform growth of silicon film.

To overcome the issue we have repeated the experiment and the process pressure were maintained at 1.3×10^{-1} mbar. Significant changes in grains size observed for silicon film on all four substrates. Comparative to other three substrates, grains on sapphire substrates are smaller. In Figure 4.3 we have shown the optimized nucleation growth in 3D AFM imaging. The grain parameters such as size, nucleation density and shape are given in Table 4.6.

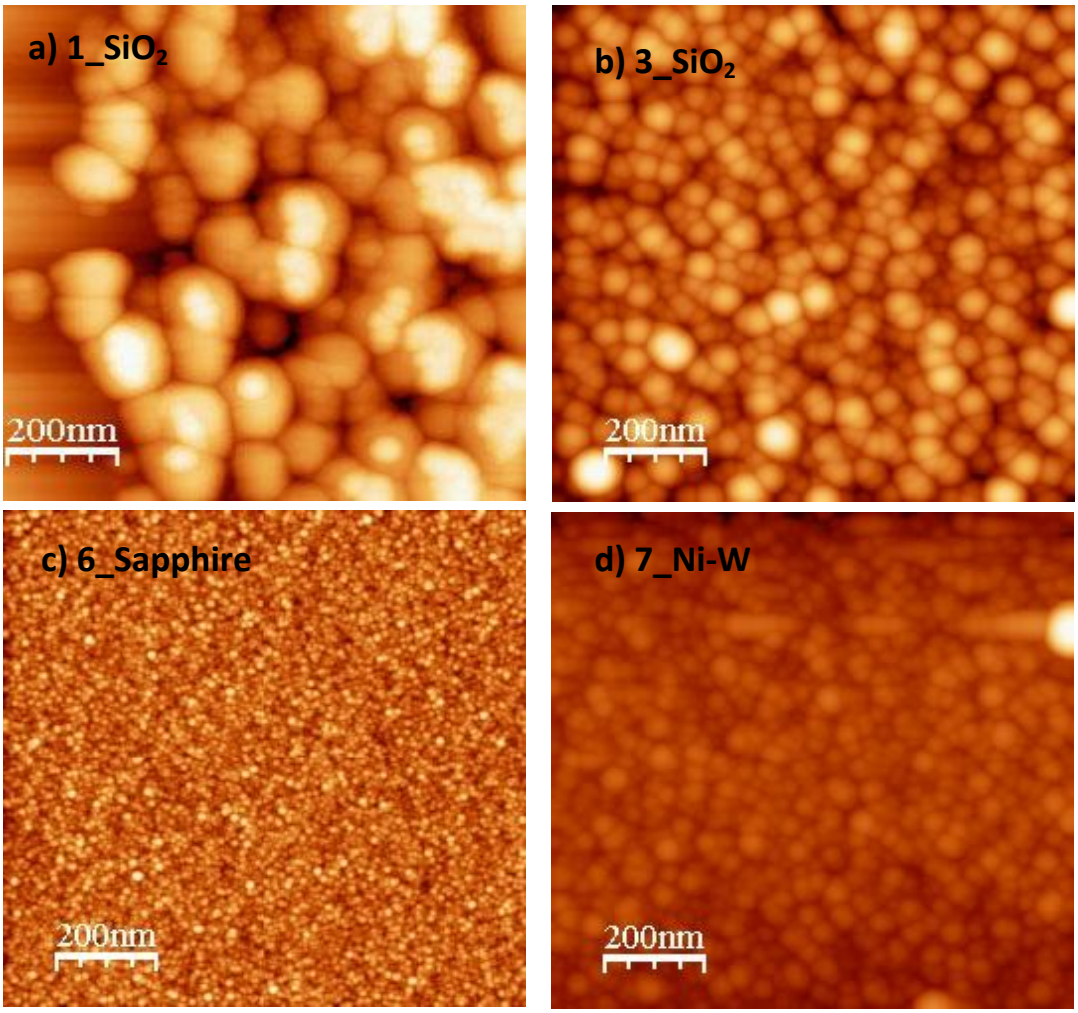

Figure 4.2 Tapping mode 2D AFM images of intrinsic poly silicon thin film on (a) 1_Si/SiO_2, 99 sccm hydrogen dilution and (b) 3_Si/SiO_2, (c) 6_Sapphire (Al_2O_3), (d) Ni-W, 20 sccm hydrogen dilution. 1 sccm of pure silane gas was introduced as a source of silane.

Table 4.6: Grains parameter from 2D & 3D AFM image analysis of silicon thin films.

Exp. No	Gas flow H_2:SiH_4 sccm	Sample name	Nucleation density in per μm^2	Average grain height in nm	Average Grain diameter in nm
1	99:1	1_Si/SiO_2	75	35	100
2	20:1	3_Si/SiO_2	160	30	40
		6_Al_2O_3	1656	1	12
		7_Ni-W	572	25	25
3	20:1	4_Si/SiO_2	115	40	18
		5_Glass/TiO_2	2	30	133
		8_ Al_2O_3	350	50	15
		9_Ni-W	1	2500	85

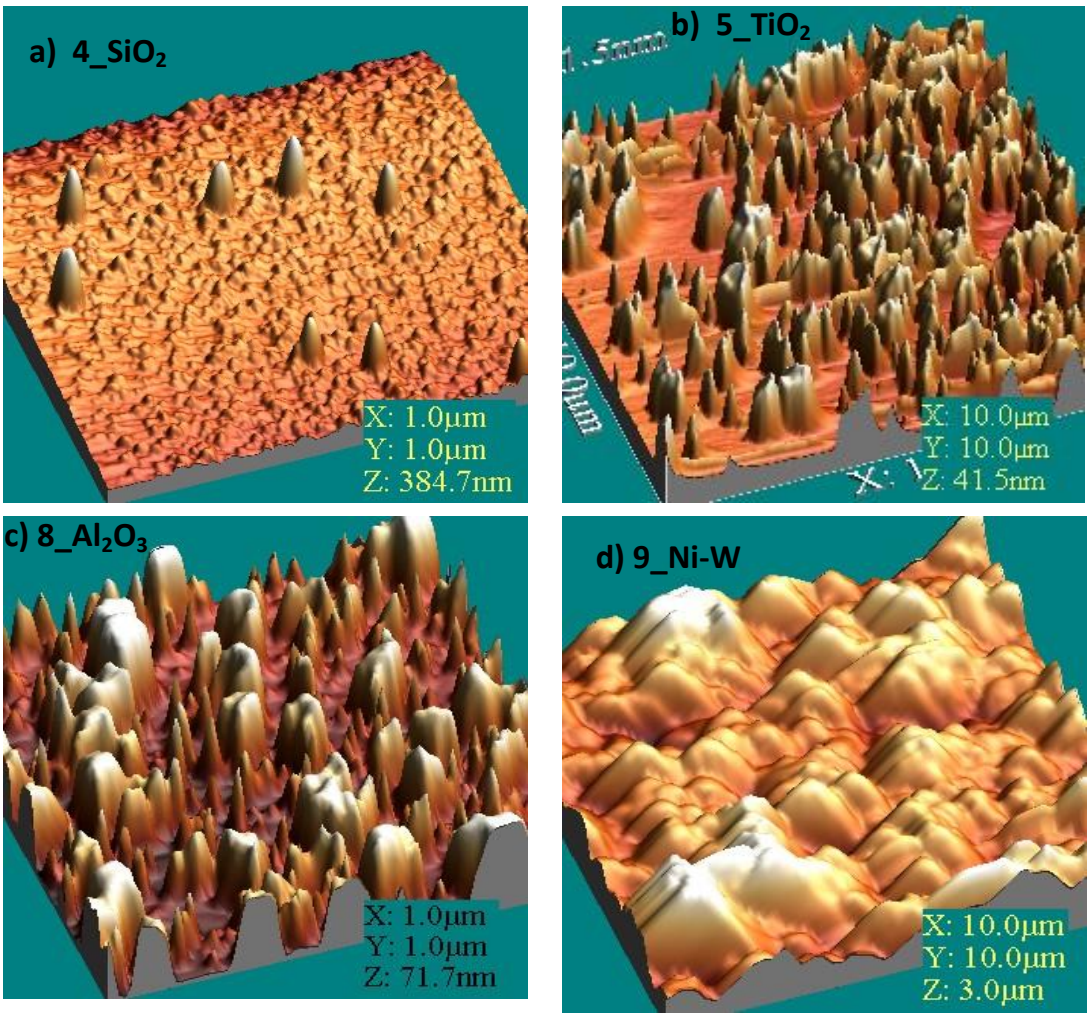

Figure 4.3: Tapping mode 3D AFM images of intrinsic poly silicon thin film on (a) 4_Si/SiO_2, (b) 5_Glass/TiO_2, (c) 8_ Al_2O_3, (d) 9_Ni-W with 20:1 H_2 : SiH_4 gas flow at a growth pressure of 1.3×10^{-1}mbar.

4.4.3 Cross section transmission electron image (X-TEM) analysis

X-TEM imaging was performed on a sample (substrate 96_Si/SiO_2) with all the sub-layers synthesized according to the process outlined in sections 4.3.1 to 4.3.5 for : i) nucleation, ii) epitaxial growth, iii) thickening stage, and iv) top layer growth stages of the intrinsic thick polycrystalline and thin amorphous silicon film on glass substrate. Si/SiO_2 substrate is used for this experiment since a) the starting surface of silicon is very smooth such that all the layers can be observed easily, and b) it is easier to cleave silicon compared to 7059 glass, which makes it easier to prepare the sample for TEM observation. Thick oxidation of silicon mimics surface such as growth on amorphous glass substrate. From X-TEM imaging, thickness of each layer is clearly observed in fig 4.4. The labels a,b,c,d,e,f ,g shown in Fig 4.4 correspond to different layers as follows: a) silicon dioxide layer of 500 nm, b) nucleation layer of 20 nm, c) epitaxial growth of 214 nm, d) columnar thick layer of 805 nm e) amorphous silicon layer of 100 nm, f) chromium layer of 30 nm and g) gold layer of 80 nm . The chromium and gold layers are deposited just prior to the TEM sample preparation to protect the grown silicon layers.

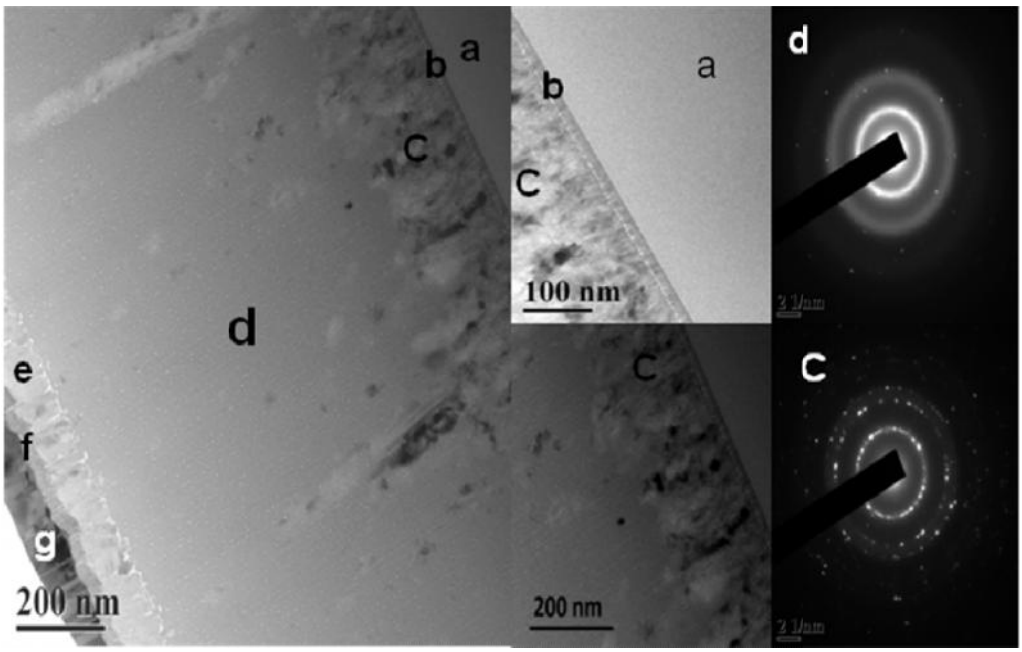

Figure 4.4 Cross section transmission electron image of intrinsic poly crystalline silicon film on 96_Si/SiO_2 substrate a) SiO_2 b) Nucleation layer c) Epitaxial growth d) columnar growth e) amorphous silicon layer f) Chromium g) Gold. Inset close look on the region a, b & c. Diffraction pattern of region c & d.

In addition to the images of different layers, Fig 4.4 shows electron diffraction from the layers. Diffraction in fig 4.4 c shows well defined spots pattern suggesting the layer (c) is predominantly single crystalline nearly epitaxial. It has some mixture of polycrystalline phases as seen from the rings. Greater detail of the phases present in this layer is also observable in fig 4.6 taken at larger magnification. Fig 4.4 d shows that the growth becomes columnar at the thickening stage. The three rings in these diffraction patterns correspond to the crystal planes of orientations (111), (220) and (311) going from the inner cone to the outer cone in sequence. These relate to the lines observed in the x-ray diffraction measurements presented in section 4.4.5.

g) Gold (80 nm)
f) Chromium (20 nm)
e) Amorphous silicon (100 nm)
d) Poly silicon columnar growth (800nm)
c) Poly silicon epitaxial layer (200 nm)
b) Poly silicon nucleation (20 nm)
a) SiO_2 (500 nm)
Si wafer (275 micron)

Figure 4.5 Schematic of different layer of silicon observed under X-TEM.

A larger magnification image of each layer quantifies crystallinity. From figure 4.6 the expected polycrystalline arrangements are clearly visible with a distinguish interface between oxide, nucleation and epitaxial layer. The top layers can be seen in figure 4.6e where amorphous region is clearly visible. Chromium film is visible from figure 4.7e where darkest portion in 4.7f is gold film. These films were deposited to avoid any damage on the silicon film during sample preparation process. Detail views of top layers are shown in figure 4.7 along with diffraction pattern of amorphous layers.

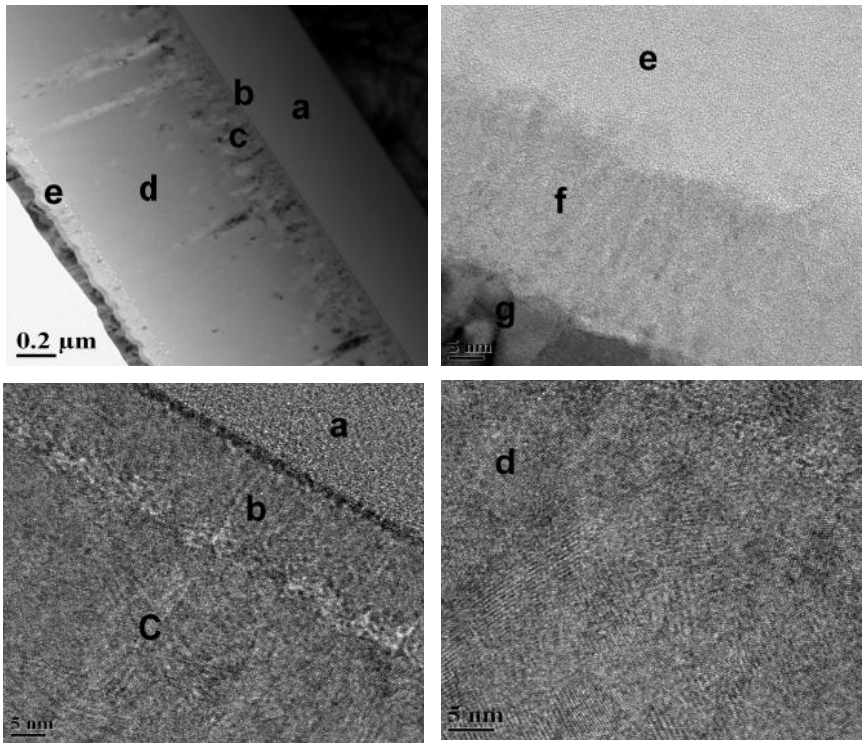

Figure 4.6 Cross section transmission electron image of intrinsic poly crystalline silicon film on 96_Si/SiO_2 substrate at higher magnification.

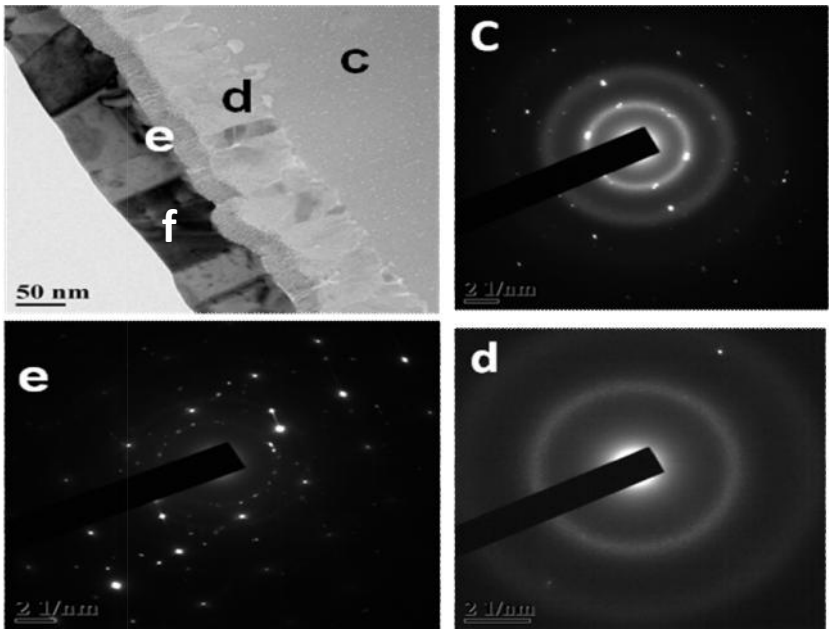

Figure 4.7 Cross section transmission electron image of intrinsic poly crystalline silicon film on 96_Si/SiO_2 substrate (Diffraction patterns).

A diffraction pattern of polycrystalline silicon film is shown in fig 4.7c. From diffraction patterns of figure 4.7(d, e) it seems to be the interface between these layers having mixed phase which can be predicted a contribution from bottom polycrystalline and top gold-chromium layers. As the thickness of total amorphous region (Fig 4.7 d,e,f) is around 200 nm which holds three different layer so it was difficult to distinguish between layers hence the diffraction patterns are of those mixed phases.

4.4.4 Scanning electron microscope (SEM) imaging

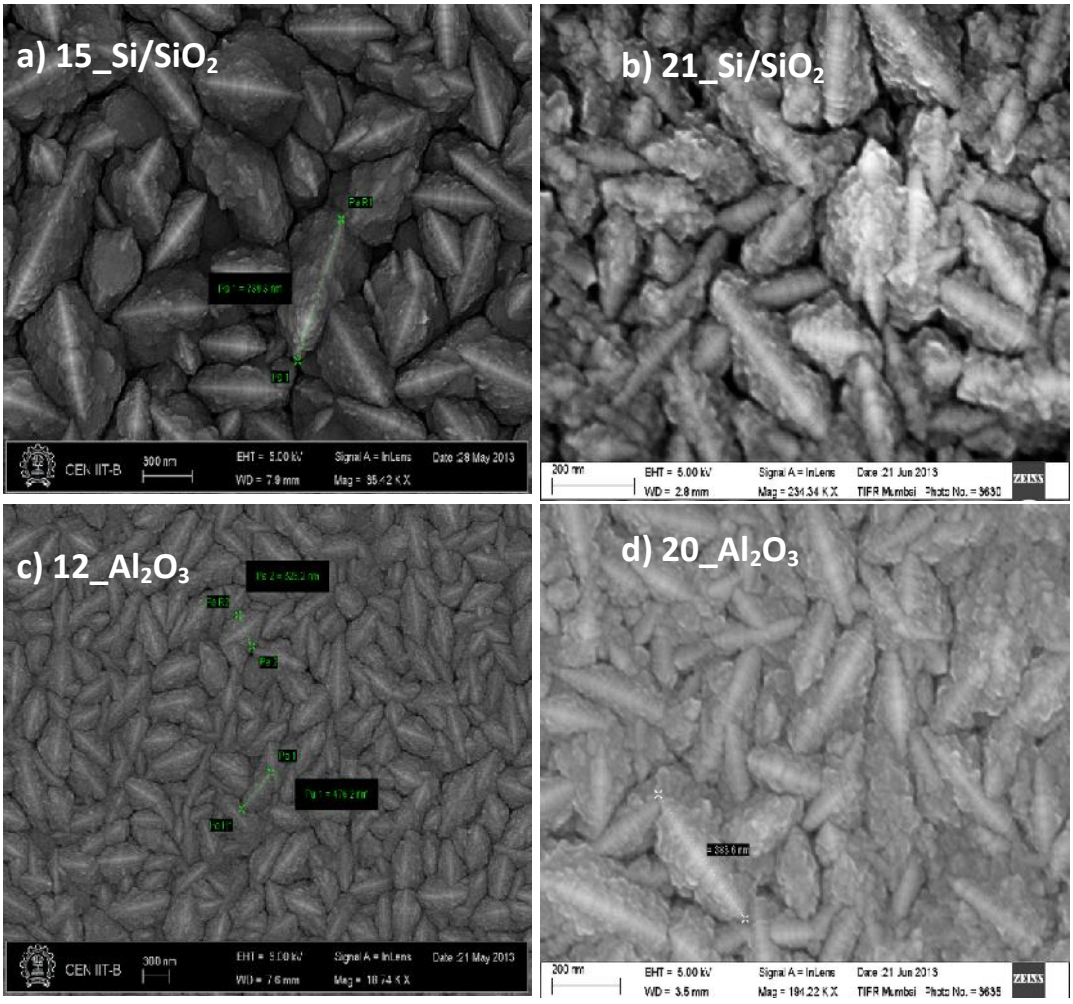

Figure 4.8 Scanning electron microscope image of intrinsic poly crystalline silicon film on Silicon and sapphire substrate (a) 15_Si/SiO_2, (b) 21_Si/SiO_2 (c) 12_ Al_2O_3, (d) 12_Al_2O_3 substrates.

We have used SEM to characterize the surface topography such as grain size, grain shape of a series of films grown at 500°C and 600°C temperatures at different SiH_4 concentration from 2 micron to 5 micron in thickness. The SEM images from figure 4.8 (silicon film on Si/SiO_2 and Al_2O_3) and figure 4.9 (silicon film on $Glass/TiO_2$) shows fish like features with a directional axis which are mostly from (220) crystal orientation. This we have explained later in x-ray diffraction analysis section 4.4.5. Crystal of orientation (111) has a shape of Bucky ball was also reported [15]. A close look magnified image prevails that the fish like grains are being added together to form a large grains.

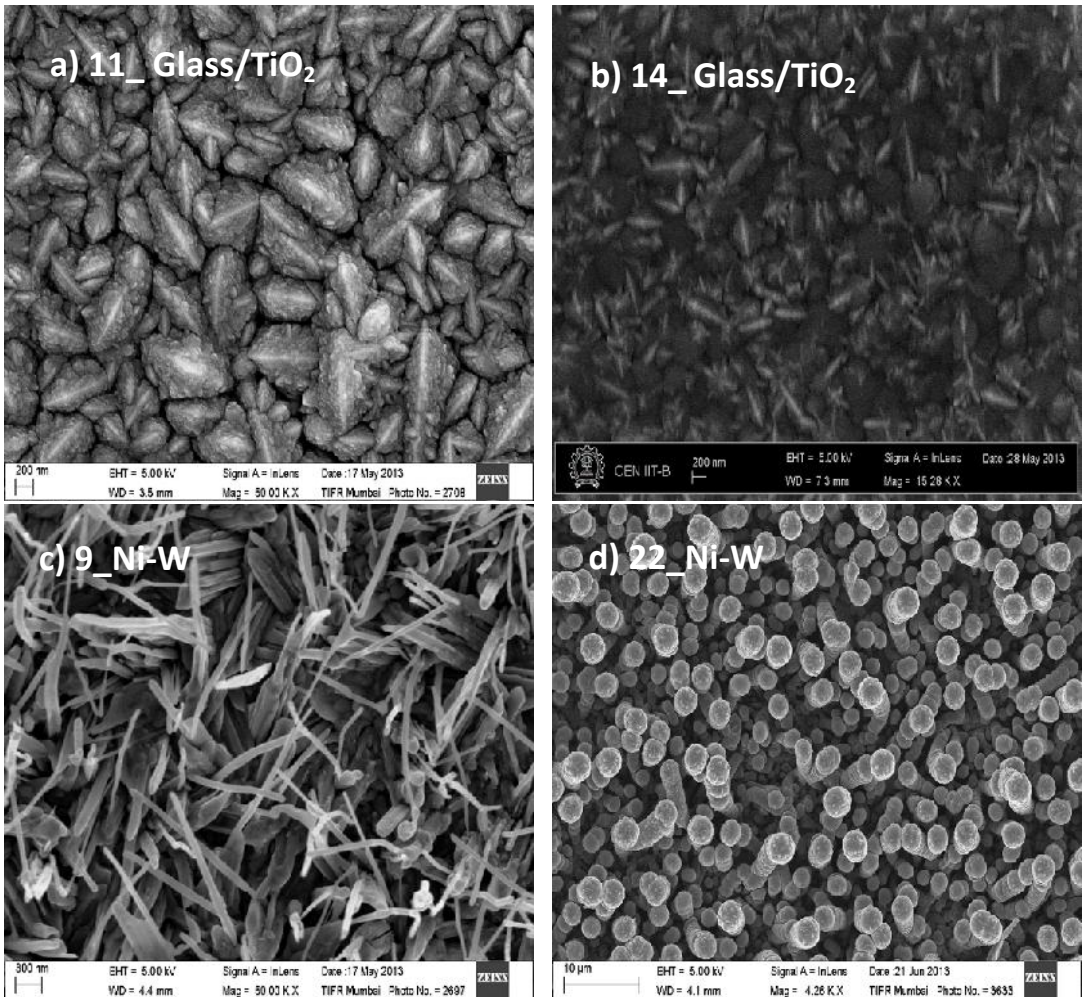

Figure 4.9 Scanning electron microscope image of intrinsic poly crystalline silicon film on titanium dioxide and nickel substrate (a) 11_$Glass/TiO_2$, (b) 14_$Glass/TiO_2$ (c) 9_Ni-W, (d) 22_Ni-W substrates.

In the case of thin film on Nickel substrates, grasses like features were observed from figure 4.9 (c). On the other hand for thick film on Nickel substrate shown in figure 4.9(d), the previous grasses like structure become columnar. Now they look like cylindrical fibre. A close look to the top of the columnar prevails that these fibre like features are combination of earlier fish like features. SEM image prevails that substrate effect is absent on Si/SiO_2, Sapphire (Al_2O_3) and TiO_2 for thick films of more than 3 microns. Thick film features on nickel substrate seems to be more columnar and an increase in temperature enhance this property.

Table 4.7: Evaluation of variation in grain size due to change in temperature and hydrogen silane concentration from SEM image.

Exp no	Substrate temp. in °C	Gas flow H_2:SiH_4 in sccm	Grain size length (L), width (W) in nm			
			Si/SiO_2	$Glass/TiO_2$	Al_2O_3	Ni-W
4	500	20:15	L631,W260	L 711,W 444	L 476,W 328	Dia 3600
5	550	20:15	L739,W300	L 500,W 300	L 697,W 300	L 12 micron Dia 4000
6	600	20:8	L300,W100	L 300,W 100	L 380,W 100	Dia 2000

From table 4.7, So far we have three different growth conditions explained in the section 4.3. With an increase in temperature, we observed grain size increased for all except TiO_2 substrate. With the decrease in silane concentration grain size decreased for all substrates.

4.4.5 X-ray diffraction analysis

X-ray diffraction measurements were performed for evaluation of crystalline orientation of intrinsic silicon film and typical size of the crystallites. XRD measurements have been made on films grown on different substrates and show the effect of the substrates on these parameters.

4.4.5.1 Effect of substrate on oriented crystalline film

Results of XRD measurements are presented in Fig 4.10 for the intrinsic poly silicon films grown on all five different substrates. These measurements were made at early stage of our work. So the growth conditions, in particular the hydrogen dilution during the growth

of thick film, differ for the films grown on different substrates. Peaks related to diffraction from the silicon films are marked (111), (220) and (311). The other peaks in the diffraction pattern observed from different substrates belong to the substrate. These are not marked in Fig 4.10 as such. Table 4.8 lists the ratio of intensities of I(111)/I(311) and I(220)/I(311) silicon XRD related peaks obtained from Fig 4.10.

Table 4.8: XRD spectra data of intrinsic poly silicon thick films grown on SiO_2, Sapphire, TiO_2, Nickel and glass substrates.

Sample name	Gas flow H_2:SiH_4 sccm	Ratio I(111)/I(311)	Ratio I(220)/I(311)	Preferred Orientation
21_Si/SiO_2	20:8	3	53	
14_Glass/TiO_2	20:15	2	41	
20_Al_2O_3	20:8	4	38	(220)
22_Ni-W	20:8	3	8	
82_Glass	20:5	5	18	

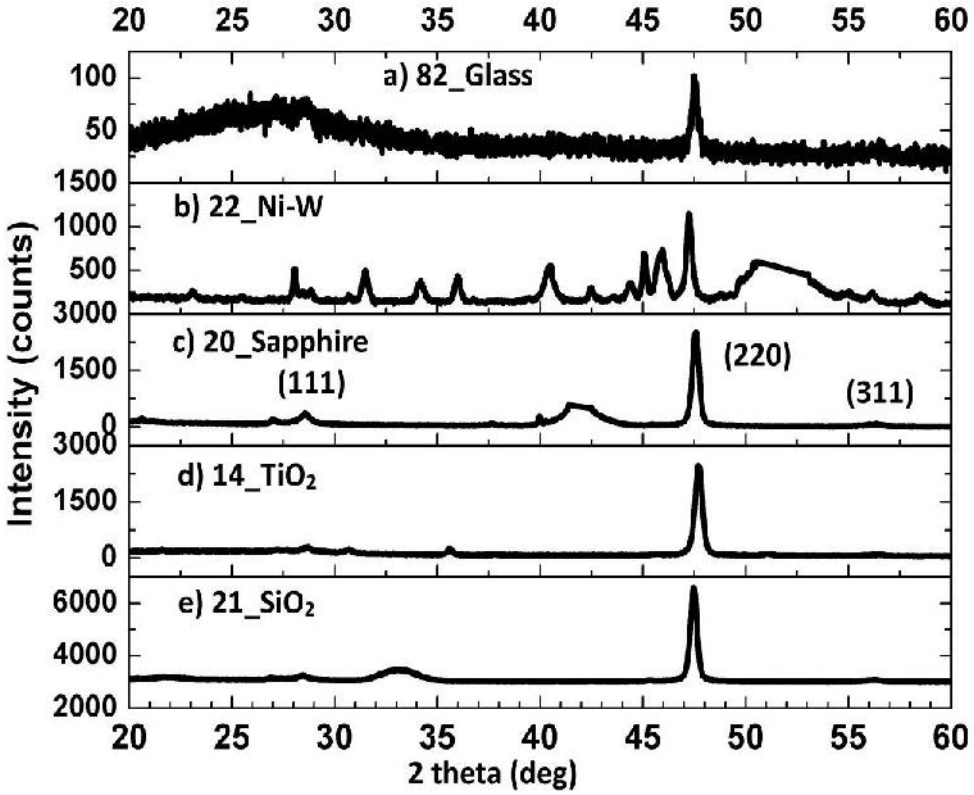

Figure 4.10 X-ray diffraction spectrum of thick (220) oriented crystalline poly silicon film on 21_Si/SiO_2, 14_Glass/TiO_2, 20_Sapphire (Al_2O_3), 22_Ni-W substrate and 82_Glass substrate.

4.4.5.2 Crystallographic texture

The relative peak heights measured on our series of samples are different from standard silicon powder [16]. We have used the ratios of the I(220)/I(311) and the I(111)/I(311) peak heights to monitor the evolution of the crystallographic texture as a function of the silane concentration. Table 4.8 and figure 4.10 show that (220) is the preferred growth direction for all the substrates except for the silicon film grown on nickel (Ni-W) substrate. Under the geometrical conditions of the θ - 2θ X-ray scan, only those planes parallel to the sample surface satisfying Bragg's condition will contribute to constructive interferences in the direction of reflexion towards the x-ray counter. Thus a preferred (220) orientation means that in most of the crystallites the (220) planes are parallel to the sample surface and, hence, the growth of the crystallites occurs by piling up (220) planes for thick silicon film. We see that the sample 21_Si/SiO_2 has the highest XRD counts and also the maximum preferred orientation intensity ratio. 22_Ni-W sample shows the lowest preferred orientation.

4.4.5.3 Grain size of oriented crystal film

Crystalline size can be explained from full width half maxima analysis. Large crystal gives rise to a sharp peak while width of peak increases as crystal size decreases. One usual way to determine the crystallite grain size is by measuring the broadening of the x-ray diffraction peaks using the Debye–Scherrer equation [17] which we have shown in Table 4.9 for (220) oriented crystals of intrinsic poly silicon film on Si/SiO_2, Glass/TiO_2, sapphire, Nickel and glass substrate. The grain size calculated from broadening of the XRD peak is smaller than we have estimated from SEM image given in table 4.7. This is because from SEM image we have estimated the size of large crystals but a closer look in those SEM image prevails that the larger grains are being accumulated by smaller grains.

4.4.5.4 Crystallographic shape

Grain shapes are obtained from SEM image shown in Figure 4.8 & 4.9. We observed the grains have a Bucky ball shape of an axial length 380 nm on Si/SiO_2, Sapphire (Al_2O_3) and Glass/TiO_2 substrate. For nickel substrate grains are more likely to be columnar. The top diameter was measured to be 2 micron where cross sectional SEM shows the height of the column is 12 micron.

Table 4.9: Full width half maxima (FWHM) and grain size of poly silicon thick film obtained from XRD spectra data on Si/SiO_2, $Glass/TiO_2$, Sapphire, Nickel and glass substrate.

Substrate	(111) FWHM at 28.5°	(220) FWHM at 47.5°	(311) FWHM at 56°	Grain size (diameter) for (220) orientation A°	Grain shape
21_Si/SiO_2	0.58	0.37	0.70	469	Bucky ball
14_$Glass/TiO_2$	0.63	0.41	0.52	423	Bucky ball
20_Al_2O_3	0.54	0.38	0.54	456	Bucky ball
22_Ni-W	0.20	0.30	0.40	578	Cylindrical
82_Glass	0.70	0.40	----	433	Circular

4.4.6 Raman analysis

4.4.6.1 Raman spectrum

The Raman spectrum of silicon film on glass substrate has been recorded to quantify the crystallinity from figure 4.11 using a 514 nm laser. The penetration depth of Raman laser beam is one micron into the film which is comparable to the thickness of the sample, which means the findings gives us an average value with respect to the depth of the sample. Raman peak position for intrinsic poly silicon film on glass is 518.5 cm^{-1} determined from the Lorentzian curve fitting [18] shown in solid green line for the spherical nano crystal in figure 4.11a. The fitted peak width is 20 cm^{-1} and a peak shift of 2 cm^{-1} observed which explains the tensile strain in the silicon film. The Raman peak shift towards the lower wavenumber (below 521 cm^{-1}) can be explained as the tensile stress in intrinsic poly silicon thin film. This deviation of peak position also attributed to the lack of complete crystallinity. Raman spectrum shows that the film on glass substrate contains amorphous and microcrystalline content which explains the peak broadening at beginning of the peak.

4.4.6.2 Raman image

Raman images of intrinsic poly silicon film on glass substrate taken with a sharp and symmetrical phonon band at around 520 cm^{-1} shown in figure 4.11b. The Raman images were formed with intensity value. Higher intensity will give large count so they will be bright on the image where lower intensity will be dark as they have less counts.

We have used sum of peak intensity from a broad range 100 cm^{-1} to 430 cm^{-1} and 490 cm^{-1} to 525 cm^{-1} of phonon band to generate two images. The average of peak intensity over the specified area will give us an image with higher and lower intensity signal from crystalline and amorphous content respectively. The Raman images from figure 4.11b can be interpreted as the brightest features which are crystalline whereas the darkest features are amorphous. The Raman images show that this silicon film is non homogeneous, contents microcrystalline and crystalline phases. The scanning area was 100 square micrometer so the resolution is less. Using a larger magnification we can narrow the scan area to 10 square micrometre which would give us a more clear view of those crystalline areas. After laser annealing we have observed significant improve in crystallinity which we would discuss in chapter 6 in section 6.5.7.

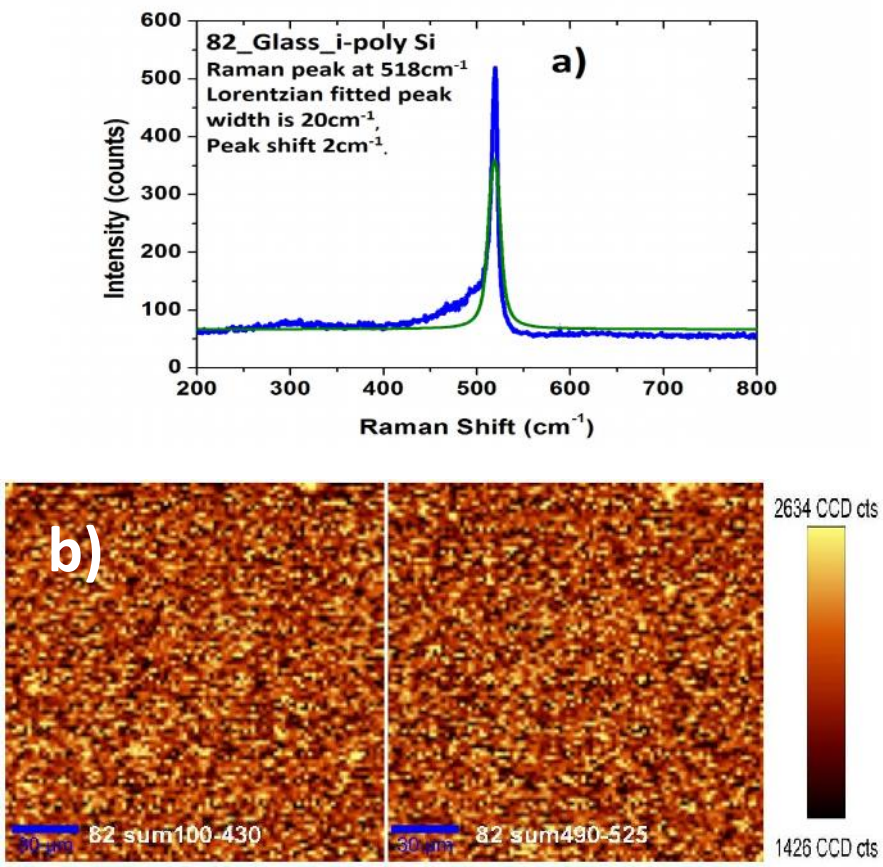

Figure 4.11: Raman shift measurement of intrinsic poly crystalline silicon film on 82_Glass substrate a) Raman spectrum b) Raman images over 100µm^2 area.

4.4.7 Activation energy analysis

One of the many virtues of poly silicon is its versatility as an electrical component in integrated circuits. The resistivity of poly silicon can vary over several orders of magnitude depending on its crystallinity and doping concentration. Therefore a method of measuring the resistivity of poly silicon films is useful because the resistance of circuit components may then be geometrically determined and designed.

Temperature dependence dark resistivity was obtained from dark I-V measurement performed in a temperature range of 323K to 403K. From temperature dependent I-V measurements, we have calculated resistivity and activation energy of intrinsic poly silicon film on Si/SiO_2, Al_2O_3 and glass substrates using log of resistivity versus 1000/T Arrhenius plot [19].

Typical plots for two samples are shown in Fig 4.12. Activation energy values for two samples calculated from slope of the Arrhenius plots are a) 0.55eV and b) 0.41eV. The lower activation energy of sample 82_Glass may be caused by background impurity in the chamber as the growth of this film was performed in the HWCVD chamber which is also used for growth of boron doped silicon film though we have cleaned and coated the chamber with 200 nm intrinsic poly silicon film before the growth [20]. At this stage we cannot rule some contamination from the substrate causing the doping.

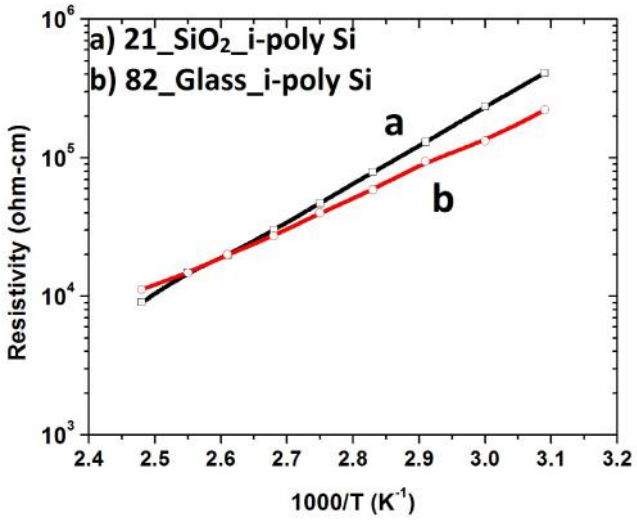

Figure 4.12 Dark resistivity versus 1000 / T curve of intrinsic poly silicon film on a) Si/SiO_2 b) Glass substrates.

Silicon has a band gap of 1.1 eV. The expected thermal activation energy of resistivity in the intrinsic regime is 0.55eV. We observed the activation energy is close to this value for the sample 10_Si/SiO_2 for the silicon film grown on Si/SiO_2 substrate. For most of the samples, the activation energy is less than 0.55 eV which shows that the films are self doped due to material defects and some contamination from the reactor chamber. Nickel substrates are highly conducting; so no in-plane electrical resistance measurements were taken on films deposited on this substrate. Glass/TiO_2 is also somewhat conducting so that in-plane measurements on silicon film deposited on this substrate will also not represent the resistivity of the silicon film.

Table 4.10: Electrical measurement of intrinsic poly silicon thick films on Si/SiO_2, Sapphire (Al_2O_3) and glass substrates.

Intrinsic poly Silicon	Resistance in ohm	Resistivity ohm-cm	Activation Energy in eV From 1000/T Vs Resistivity graph
10_Si/SiO_2	1×10^8	4×10^5	0.58
15_Si/SiO_2	4×10^7	2.1×10^5	0.36
21_Si/SiO_2	1×10^8	2×10^5	0.55
12-Al_2O_3	6×10^8	2×10^6	0.47
16- Al_2O_3	6.6×10^6	2.4×10^4	0.28
20- Al_2O_3	2.9×10^8	5×10^5	0.42
82_Glass	1.8×10^8	3.6×10^5	0.41

4.4.8 Reflectance spectrum analysis

Reflection spectra for intrinsic poly silicon films deposited on Si/SiO_2, Sapphire (Al_2O_3), Glass/TiO_2 and Nickel are presented in Figure 4.13 in the wavelength range 300 nm to 1100 nm. The reflection spectrum has features which are similar to the crystalline silicon [21].There is a peak at the energy ~3.3 eV (375 nm), characteristic of crystalline silicon. An increase in temperature as well as decreasing the silane concentration increases the reflection in the short wavelength (< 700 nm) range for all four samples. For Si/SiO_2 the increase is ~ 10 %, for Sapphire about 10 to 20 %., for Nickel it is 5 %, for Glass/TiO_2 it is 2 %. The low value of reflectivity for Ni-W and TiO_2 are related to roughness of the film on these substrates. At longer wavelengths, we observe characteristic thin film interference

effect that results from the reflectance of light from the top (air – film interface) and bottom (film – substrate interface) of the thin film. The separation of the interference fringes is related to film thickness, which changes with the process parameters such as silane concentration, hydrogen dilution etc.

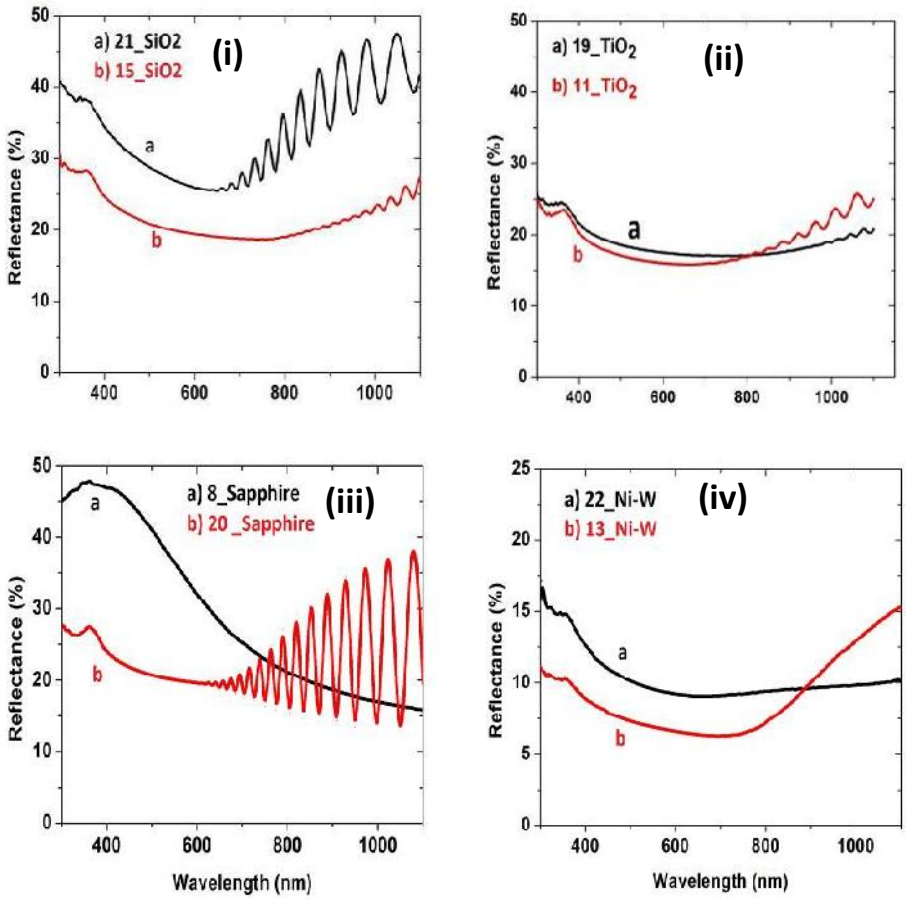

Figure 4.13: Reflectance spectrum at two different growth condition of silicon film on i) Si/SiO_2 ii) $Glass/TiO_2$ (iii) Sapphire (Al_2O_3) and iv) Nickel (Ni-W).

4.4.9 Transmission spectrum analysis

The interpretation of transmission spectrum for intrinsic poly silicon film grown on Sapphire and glass substrate preformed from figure 4.14. The energy at which absorption starts is characteristics for each material. The spectrum shows that for high energies there is no transmission because all the light is absorbed.

For low energies there are no appropriate electronic transitions possible so transmission is very high in this range. For thin film the transmission is larger for films on

both substrates. Silicon film on sapphire and glass substrate shows similar transmission characteristics with interference fringes observed in the transmission spectra [22, 23].

Texturing of these substrates using diamond powder can reduces the back and forth internal reflection between substrate and film which also will reduce the transmission of light in visible range. Also these fringes are present only in thick film which is a signature of the thickness of the film. From separation of interference fringes we can estimate film thickness, refractive index using envelope method [24, 25]. No transmission data taken for silicon film on Si/SiO_2, $Glass/TiO_2$ and Nickel (Ni-W) substrates as they were not transparent to visible light.

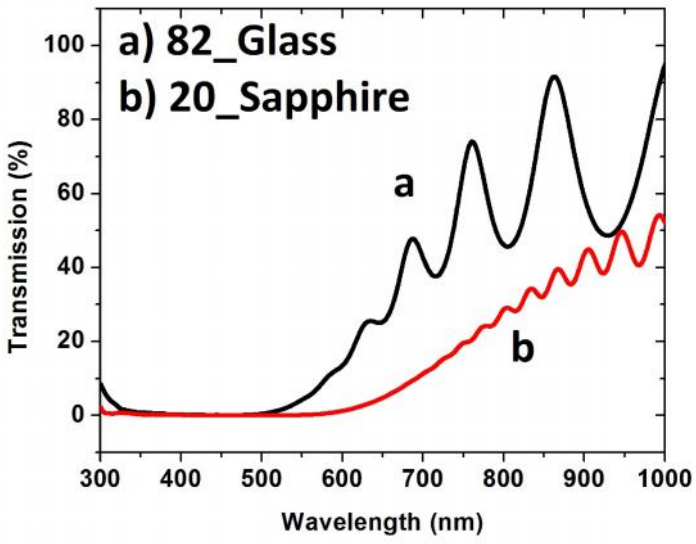

Figure 4.14: Transmission spectrum of intrinsic poly silicon film grown on a) 82_Glass and b) 20_ Sapphire substrate.

4.4.10 Photocurrent analysis

The spectral responses of two samples were studied in HWCVD with identical growth condition. The photocurrent spectral responses of these two samples are shown in figure 4.15. A decrease in photoconductivity at shorter wavelengths below 600 nm is observed which indicates surface recombination and can be further improved by better surface passivation due to atomic hydrogen during substrate cooling from 600°C to 200°C. The decrease in photoconductivity at longer wavelengths more than 800 nm is also observed

which is related to low value of light absorption co-efficient. The oscillations in the both the spectrums are related to interference from glass substrate which can be removed by using a textured glass substrate as the textured glass substrate will reduce the reflection from the plane. We have calculated the dark conductivity from room temperature dark I-V measurement for intrinsic silicon film on glass substrate which is $2.7\times10^{-6}\ \Omega^{-1}cm^{-1}$ for sample 82_Glass shown in table 4.10.

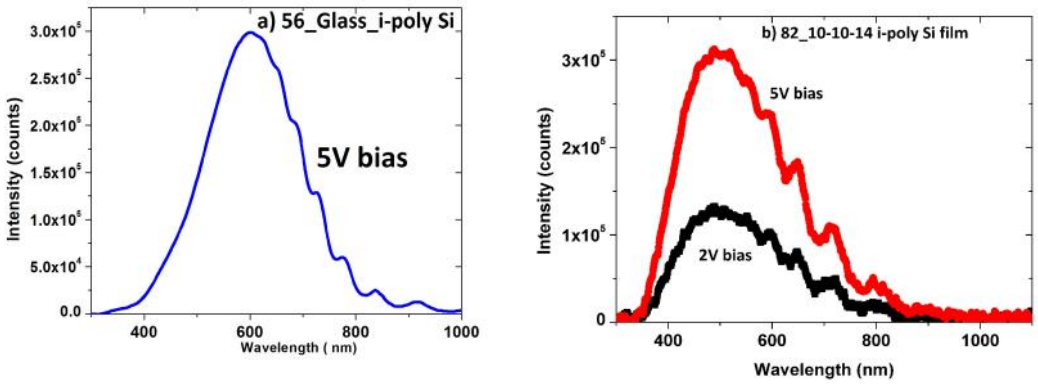

Figure 4.15: Photocurrent spectral response of intrinsic polycrystalline silicon film under 5V and 2V bias a) 56_Glass_ i-poly Si b) 82_Glass_ i-poly Si

4.4.11 Photoluminescence (PL) spectrum analysis

The PL technique has advantage of being non-contact and non destructive, allowing characterization of sample before and after each step of synthesis sequence.

Figure 4.16 shows room temperature and low temperature PL spectrum, taken on intrinsic poly crystalline silicon film grown on glass and FTO coated glass substrate. Figure 4.16 also shows PL spectrum taken on textured and polished glass substrate. It is observed that the interference fringes are not present on PL spectrum of textured glass substrate.

Figure 4.17 shows PL spectrum of intrinsic poly silicon film on glass and FTO coated glass substrate under different growth condition using HWCVD. Hydrogen passivation shows a significant improvement in the material quality by reducing defects. Here we had two such kinds of synthesis steps. First we had intrinsic poly silicon thin film grown with hydrogen passivation shown Fig 4.17a and second we had intrinsic poly silicon thin film grown.

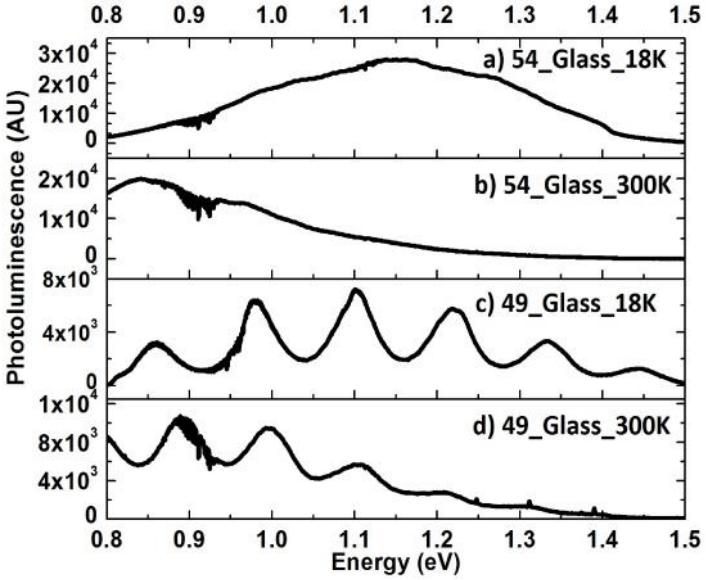

Figure 4.16 Photoluminescence (PL) spectrum of intrinsic poly silicon film on a) 54_Textured glass at 18K b) 54_Textured glass at 300K c) 49_Polished glass at 18K d) 49_Polished glass at 300K substrate under similar growth condition using HWCVD.

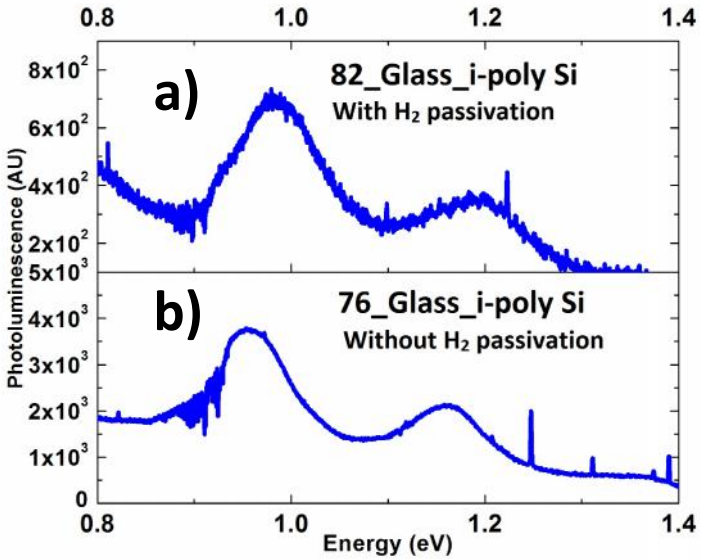

Figure 4.17 Photoluminescence (PL) spectrum of intrinsic poly silicon films on glass substrate a) 82_Gl_i-poly Si (with hydrogen passivation) b) 76_Gl_i-poly Si (without hydrogen passivation).

We have used shorter wavelength laser (532nm) which allows shorter absorption depth (about one micron), also carriers generated by short wavelengths are generated further from glass side surface [26]. In our study form PL spectrum shown in figure 4.17, we observed hydrogen passivation for intrinsic poly silicon film improves the overall material quality. Observation also prevail that PL peak shifted from 0.9 to 0.98 eV for the film on glass substrate. This shows reduced defects and radiative recombination due to atomic hydrogen passivation.

4.4.12 Fourier transform infrared (FTIR) spectrum analysis

Infrared (IR) spectra of intrinsic poly crystalline silicon film yield information about the defects, impurities etc [27]. In our study we have concentrated our FTIR analysis to Si-H, Si-OH and Si-O-Si bonds. The absorption spectrum analysis performed from figure 4.18. FTIR absorbance spectra exhibit a number of absorption peaks corresponding to Si-H, Si–O-Si bonds under certain wavelength of infrared light.

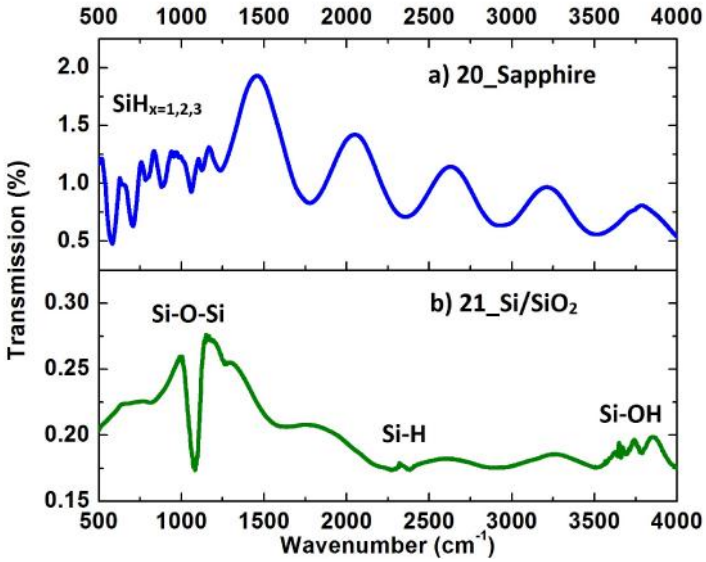

Figure 4.18: Infrared normalized transmission spectrum of intrinsic poly silicon film on a) 20_Sapphire b) 21_Si/SiO_2 and substrate.

The characteristics of vibrational modes of these bonds are explained as wagging, weak stretching, weak bending and stretching in wave number ranging (630-670, 780-800, 940-1100, 2000, 3000-3700 cm^{-1}) respectively [28]. Silicon film on Si/SiO_2 substrate shows

stretching vibrations of oxygen in the Si-O-Si bonds at 1100 cm^{-1}. Less intense surface vibrational feature around 3500 cm^{-1} is contribution from Si-OH. The area under the broad absorption around 2000-2500 cm^{-1} is stretching mono and di-hydride of Si-H and Si-H_2. In the silicon film on sapphire substrate, the peak observed about 630 cm^{-1} shows a wagging peak of Si-H. Weak stretching peak of interstitial oxygen Si-O-SI is observed at 1000 cm^{-1}. In the case of silicon film on sapphire, absorption analysis is considered only up to 1500 cm^{-1} since sapphire is opaque in mid-IR range [29, 30].

4.4.13 Energy dispersive X-ray spectroscopy (EDX) analysis

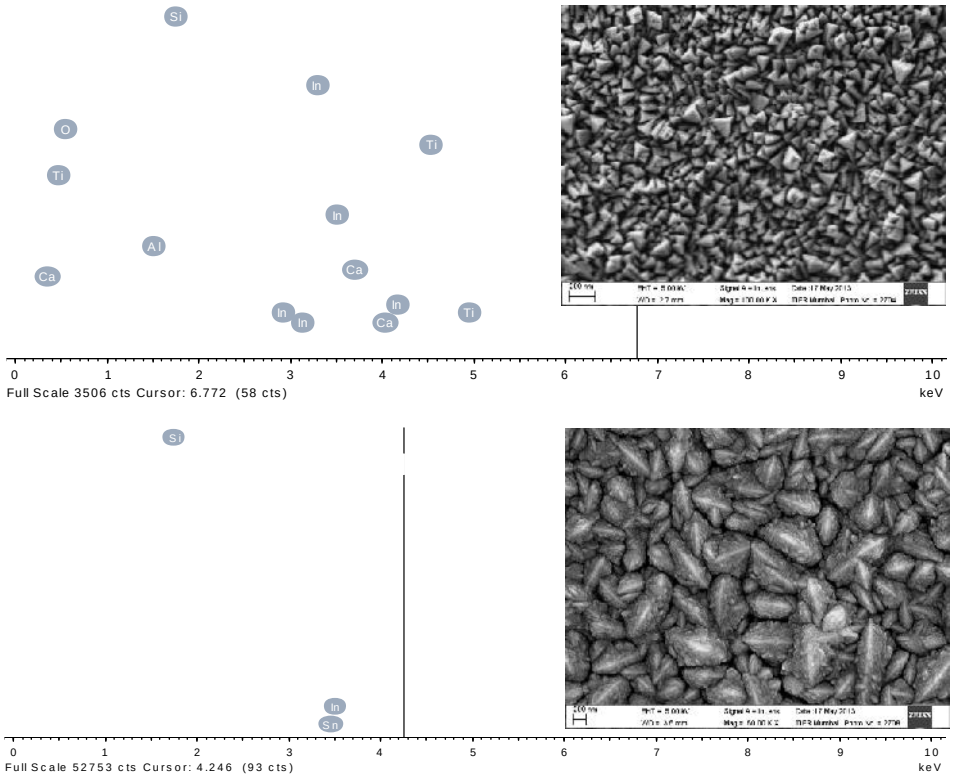

Figure 4.19: 10keV EDX spectrum of intrinsic poly Silicon film in TiO_2 substrate a) Thin film on 5_ Glass/TiO_2 b) Thick film on 11_ Glass/TiO_2, Inset SEM image of area where EDX was performed.

The elemental composition and their local distribution evaluated for intrinsic silicon film on TiO_2, nickel and glass substrate are shown in figure 4.19 and 4.20. For thin silicon film on TiO_2 substrate the EDX spectrum shows elements from substrate such as titanium and indium as well as silicon, oxygen and carbon. In case of thick silicon film the substrate elements are suppressed by silicon. From figure 4.20a, EDX of a sample of silicon thick film on nickel substrate shows substrate element nickel. Silicon film on alkali free borosilicate glass substrate shows the presence of aluminium (Al) and barium (Ba) from the substrate. Carbon and oxygen were also detected as contamination.

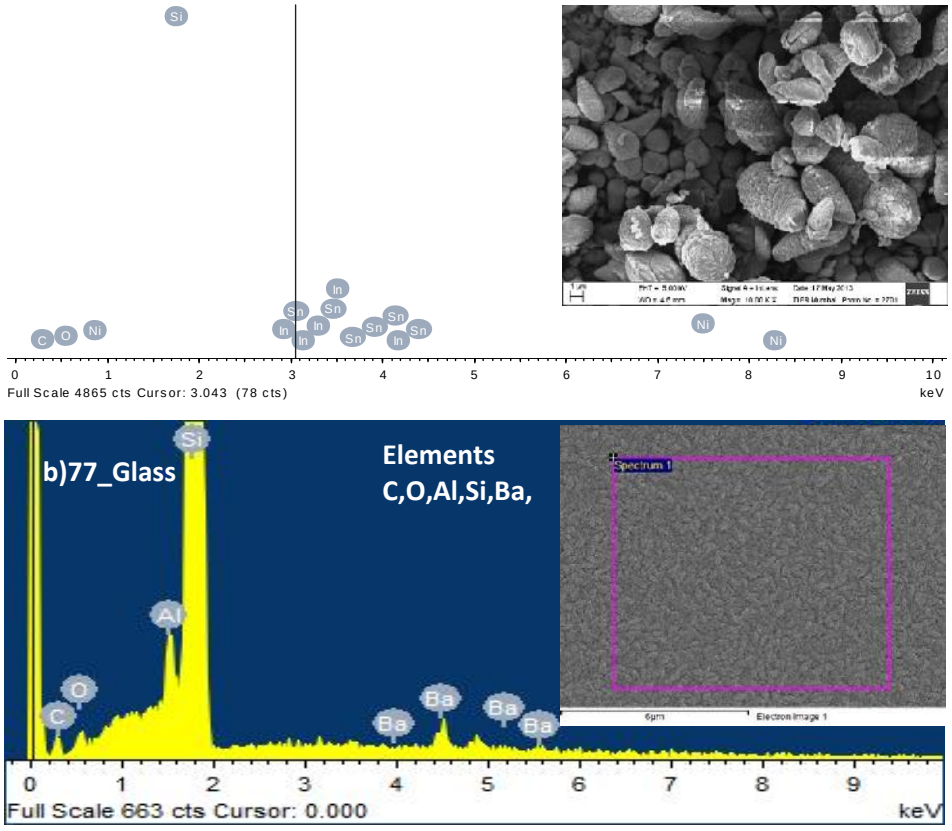

Figure 4.20: 10keV EDX spectrum of intrinsic poly Silicon film on a) 13_Nickel b) 77_Glass substrate. Inset SEM image of area where EDX was performed.

4.5 Discussion

In our study we have investigated the viability for the growth of large grain intrinsic poly crystalline silicon films on Si/SiO_2, Sapphire, $Glass/TiO_2$, Nickel and alkali free borosilicate glass substrates for possible application in photovoltaics as absorber layer in a p-i-n structure device. Grain size as large as 700 nm was observed for 15 sccm SiH_4 in 20 sccm H_2 for silicon deposited on Si/SiO_2, sapphire and $Glass/TiO_2$. As films on sapphire and $Glass/TiO_2$ substrates got lifted due to high tensile stress at high silane (SiH_4) content, we have reduced silane concentration to 8 sccm and grain size of 400 nm was obtained. With reduced silane flow, the film got highly sticky to all substrates. The stable thicknesses of the poly silicon thick film were 2.2 micron with 8 sccm SiH_4 at 600°C. For photovoltaic application SiO_2, sapphire and glass can be used using this amount of silane flow. But for $Glass/TiO_2$ substrate, silane concentration has to be increased as well as film stress has to be maintained so film does not get lifted. For nickel substrate an additional buffer layer is needed to form a junction with the absorber layer [31]. Further study can be done on these two substrates for their viability as substrate for photovoltaic application.

The observations by means of the cross sectional transmission electron microscopy of the structure of various layers of polycrystalline and amorphous silicon films intended for photovoltaic application has been presented. These observations allowed us to evaluate amorphous and polycrystalline region as well as interfaces between layers from diffraction patterns. In this study we have presented a technique for growing and defect annealing of intrinsic oriented crystalline poly Si film under atomic hydrogen soaking using HWCVD. Activation energy and photocurrent response analysis shows the films are suitable as absorber layer in photovoltaic devices. An initiative was taken to increase the thickness of film by increasing the growth duration under reduced amount of silane (5sccm) which will allow more light to absorb though the film got lifted due to high tensile stress and defects. An increase in hydrogen dilution may solve the issue. In that case increase growth pressure in the chamber may have to be taken care off.

In this work we have explored the viability for the growth of optically suitable large grain (220) oriented intrinsic poly crystalline silicon films on Si/SiO_2, Sapphire, $Glass/TiO_2$, Nickel and alkali free borosilicate glass substrates for photovoltaic application using HWCVD techniques. It has been reported [32] that using plasma enhanced CVD and very high frequency glow-discharge [7], (220) orientation silicon film was obtained. Films on these five substrates are poly crystalline as we can see optical band gap is in between the standard

value for amorphous and crystalline phase. For film on Glass/TiO_2 substrate, an increase in silane concentration enhances the crystallinity of the film which we can conclude from optical band gap.

4.6 References

[1] S. Gall, C.Becker, K.Y.Lee, T.Sontheimer, B.Rech, Growth of polycrystalline silicon on glass for thin-film solar cells, Journal of Crystal Growth 312, p1277–1281, 2010.

[2] O Nast, T. Puzzer, L.M. Koshier, A.B. Sproul and S.R. Wenham, "Aluminum-induced crystallization of amorphous silicon on glass substrates above and below the eutectic temperature", Appl Phys Lett 73, 3, p214, 1998.

[3] J.Dore,R.Evans,U.Schubert,B.D.Eggleston,D.Ong,K.Kim,J.Huang,O.Kunz, M.Keevers, R Egan, S Varlamov, M.A.Green, Thin-film polycrystalline silicon solar cells formed cells formed by diode laser crystallisation, Progressin Photovoltaics Researchand Application 21, 1377, 2013.

[4] S. Varlamov et al, Polycrystalline silicon on glass thin-film solar cells: A transition from solid-phase to liquid-phase crystallised silicon, Solar Energy Materials & Solar Cells 119, p246–255, 2013.

[5] C.W. Teplin, D.S. Ginley, H.M. Branz, "A New Approach to Thin Film Crystal Silicon on Glass: Biaxially Textured Silicon on Foreign Template Layers", J. Non- Crystalline Solids, 352, pp. 984, 2006.

[6] A T Findikoglu,W Choi, V Matias, T G Holesinger, Q X Jia, and D E Peterson, " Well oriented silicon thin films with high carrier mobility on polycrystalline substrates", Advanced Materials 17, p1527, 2005.

[7] E Vallat-Sauvain, U Kroll, J M J Meirer, A shah, and J Pohl, " Evolution of the microstructure in microcrystalline silicon prepared by very high frequency glow-discharge using hydrogen dilution", J Appl Phys 87 , 3137, 2000.

[8] Tandeep S. Chadha, School of Engg & Appl. Sci. Washington Univ. St. Louis, Missouri, USA.

[9] http://www.evico.de/en/ superconductor-material/textured-substrates.

[10] http://www.semiwafer.com/products/sapphire.

[11] Veenendaal P., "HWCVD of polycrystalline silicon: from gas molecule to solar cell", Ph D Thesis, University of Utrecht Netherlands, p. 14-35, 2002.

[12] Ruihua W, Zhiqiang L, Li L, Jahe L, "Study of HWCVD technique for silicon thin film", Solar Energy Mat & Solar Cells 62, p. 193, 2000.

[13] N. Nickel, N. Johnson, and W. Jackson, 'Hydrogen passivation of grain boundary defects in polycrystalline silicon thin film' Applied Physics Letters 62, 1993.

[14] J. Pallarès and R. E. I. Schropp 'Role of the buffer layer in the active junction in amorphous-crystalline silicon hetero junction solar cells', J. Appl. Phys. 88, 293, 2000. (doi.org/10.1063/1.373656).

[15] A. R. Middya, J.J. Liang and K. Ghosh, MRS Proceedings, 862, A19.8, 2005. (doi:10.1557/ PROC -862-A19.8)

[16] S. Schicho F. Köhler R. Carius A. Gordijn, Solar Energy Materials and Solar Cells , Volume 98, Pages 391-397, 2012.

[17] B. D. Cullity,Elements of X-Ray Diffraction, 2nd ed. Wesley,Reading, MA, pp. 283 and 284, 1978.

[18] Pelikan Peter Ceppan Michal, Liska Marek, 'Applications of Numerical Methods in Molecular Spectroscopy', Boca Raton, Chapter 2, CRC Press, 1993,

[19] H. Fritzsche, Journal of Non-Crystalline Solids, 49, p62, 1971.

[20] Gurleen K, Abul Hossion, Kulasekaran M, Brij M. Arora, 'Synthesis of oriented and passivated polycrystalline silicon films on glass by hot wire chemical vapor deposition' 40th Photovoltaic Specialists Conference, Denver, Colorado, USA. (ieeexplore.ieee.org article no 06925162).

[21] M. A. Green and Keevers, M. J, Optical properties of intrinsic silicon at 300 K, Progress in Photovoltaics: Research and Applications, vol. 3, pp. 189 - 192, 1995.

[22] Bhira L., Essaidi H., Belgacem S., Couturier G., Salardenne J., Barreaux N., Bernede J.C., phys. Status solid (a), 181, p427, 2000.

[23] George J., Joseph K.S., Pradeep B., Palson T.I., phys. status solid (a), 106, p123, 1988.

[24] R Swanepoel, 'Determination of the thickness and optical constants of amorphous silicon' J. Phps. E: Sci. Instrum.. Vol. 16, p1283, 1983.

[25] S. Ilican, M. Caglar, Y. Caglar. 'Determination of the thickness and optical constants of transparent indium-doped ZnO thin films by the envelope method', Materials Science Poland, Vol. 25, No. 3, 2007.

[26] J. Dore, D. Ong, S. Varlamov, R. Egan, M. Green, Progress in laser crystallized thin-film polycrystalline silicon solar cells: Intermediate layers, light trapping, and metallization, IEEE Journal of Photovoltaics 4(1)(2014)33/39.DOI10.1109/ JPHOTOV, 2280016, 2013.

[27] S. Perkowitz, Optical Characterisation of Semiconductors, Acad.Press, London 1993.

[28] Gracin D., Radic N., Desnica, U. V., Andreic Z., Balzar D., Thermal stability of amorphous silicon–carbon alloys deposited by magnetron source. Fizika A 4 (2), p329–335, 1995.

[29] D. Krcho, Proc. AEMC' 98, Adelaide, 1998.

[30] T.S. Eriksson, C.G. Granqvist, J. Appl. Phys. 60, 6, p2081-91, 1986.

[31] McCandless BE, Hegedus SS. Proc. of the 22 th IEEE Photovoltaic Specialists Conference, p967–972, 1991.

[32] Wu Aimin, Deng WanTing, Sci. China Ser E-Tech Sci Jan. vol. 52, no.1 260-263, 2009.

Chapter 5

Synthesis of p-type silicon in HWCVD

5.1 Introduction

In this chapter we have described growth and characterization of boron doped amorphous and poly crystalline silicon films synthesized by using HWCVD. To investigate the effect of substrate on boron doped silicon film, we have considered four different substrates (Si/SiO_2, TiO_2, Al_2O_3 and nickel) for the growth of poly crystalline silicon films. Among the characterizations, we have measured optical transmission and reflectance spectra, electrical resistivity, and crystalline orientation using X-ray diffraction. Synthesis of thin (100 nm and 75 nm) boron doped p-type amorphous silicon was also done on two different substrates: i) alkali free borosilicate glass and ii) Si/SiO_2 substrates. The substrates were covered with intrinsic polycrystalline silicon before the growth of boron doped p-type amorphous silicon layer. A range of experiments were conducted by varying the growth conditions. In this chapter, only representative experimental results are presented.

5.2 Substrates

We have used five possible substrates Si/SiO_2, $Glass/TiO_2$, Al_2O_3, Nickel and Glass for the investigation of the growth of boron doped p-type silicon film using HWCVD technique as outlined in section 2 of chapter 4. Details of substrate preparation and cleaning process are discussed in Appendix II.

5.3 Growth process

5.3.1 Growth of boron doped poly crystalline silicon film

Boron doped silicon films were grown on various substrates using HWCVD, starting with thin silicon nucleation layer at lower substrate temperature (400°C) followed by growth of thick silicon film at higher substrate temperature (600°C).

The gas mixture used for nucleation consists of 15 sccm H_2, 1 sccm SiH_4 and 5 sccm of dilute diborane (5% diborane diluted in 95% hydrogen). After the growth of nucleation layer, the substrate shutter is positioned between the substrate and the filament and silane flow is stopped while leaving the filament on. The substrate temperature is ramped from 400°C to 600°C using the substrate heater kept under the substrate holder. After reaching the required temperature, we turn on silane, hydrogen, and diborane gas mixed flow, remove the shutter and continue the growth of silicon.

Table 5.1: Growth of boron doped p-type polycrystalline silicon films on Si/SiO_2, Sapphire (Al_2O_3), $Glass/TiO_2$ and Nickel substrates.

Exp. No	Sample name	Process Pressure in mbar	Substrate temp. in °C	Gas flow in sccm H_2: SiH_4: 5%B_2H_6	Growth duration in Sec	Film Thickness in nm
Two stage growth (Thin film)						
7	18_Si/SiO_2 24_Al_2O_3 25_$Glass/TiO_2$ 26_Ni-W	2.4×10^{-1}	400	15 : 1 : 5	120	___
		2.5×10^{-1}	600	15 : 1 : 5	1000	
Six stage growth (Thick film)						
8	2_Si/SiO_2 27_$Glass/TiO_2$ 29_Ni-W 30_ Al_2O_3	2.3×10^{-1}	400	15 : 1 : 5	100	1085
		2.1×10^{-1} to 2.3×10^{-1}	600	15 : 1 : 5	100	
				15 : 1.5 : 5	100	
				13 : 2 : 5	100	
				12 : 3 : 5	100	
				10 : 5 : 5	1000	

Growth of silicon layer has been done by two schemes. In the first scheme, the gas mixture remains the same as used for the nucleation stage. This stage helps us to evaluate the electrical conductivity of boron doped poly crystalline silicon film under low concentration of silane in hydrogen. In the second scheme, the growth of silicon layer proceeds in 5 stages after the nucleation stage, with gradually increasing concentration of SiH_4 as listed in Table 5.1. The silane flow rate is increased in steps while simultaneously decreasing the H_2 flow rate in order to keep the chamber pressure constant. Growth parameters are given in Table 5.1.

5.3.2 Growth of boron doped amorphous silicon film

Boron doped amorphous silicon film was grown on glass and Si/SiO_2 substrate at 200°C substrate temperature. This amorphous silicon layer was grown at 1900°C filament temperature on top of intrinsic polycrystalline silicon film explained in chapter 4, section 4.2. Growth conditions of these films are given in Table 5.2.

Table 5.2: Growth of boron doped p-type amorphous silicon films on Si/SiO_2 and glass substrates.

Exp No	Sample name	Process Pressure in mbar	Substrate temp. in °C	Gas flow in sccm H_2: SiH_4: $5\%B_2H_6$	Growth duration in Sec	Film Thickness* in nm
24	87_Glass 89_pSi 39_Si/SiO_2	7.8×10^{-2}	400	20 : 1	100	20
		8.5×10^{-2}	600	20 : 1.5	100	1040
		7.5×10^{-2}		18 : 2	100	
		7.8×10^{-2}		17 : 3	100	
		8.9×10^{-2}		15: 5	1200	
		9.9×10^{-2}	200	20 : 2.5	30	100
		1.1×10^{-1}		20 : 1 : 1	600	
27	96_Si/SiO_2	6.7×10^{-2}	400	20 : 1	100	20
		7.5×10^{-2}	600	20 : 1.5	100	1020
		6.5×10^{-2}		18 : 2	100	
		6.8×10^{-2}		17 : 3	100	
		7.1×10^{-2}		15: 5	1200	
		6.8×10^{-2}	200	20 : 2.5	25	75
		1.3×10^{-1}		20 : 1 : 2.2	50	

* Cross section TEM Imaging

5.4 Characterization Results

Results presented in this section deal with i) topographical characterization using scanning electron microscope, ii) electrical characterization using four point probe set up, iii) reflectance, transmission measurements using UV-VIS-NIR spectrometer, iv) X-ray diffraction is performed for evaluation of crystalline orientation of boron doped silicon film, v) concentration of boron is determined using time of flight secondary ion mass spectroscopy, vi) Fourier transform infrared spectroscopy for evaluation of Si-H, Si-OH, Si-O-Si stretching bonds; vii) Energy dispersive X-ray analysis for the evaluation of atomic percentage of contaminations such as oxygen, carbon etc.

5.4.1 SEM image analysis

We have taken scanning electron microscope (SEM) images at different magnification to observe the grain size and shape in p-type polycrystalline silicon films.

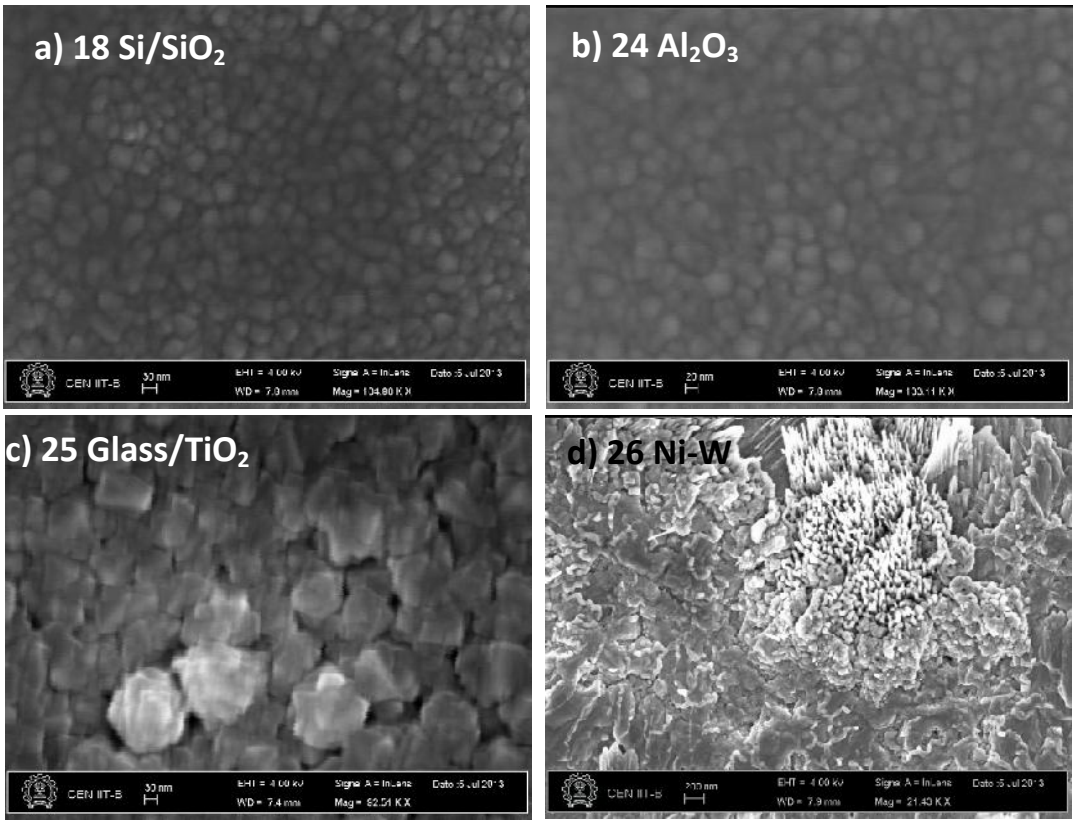

Figure: 5.1 SEM image of boron doped p-type poly crystalline silicon thin film on a) Si/SiO_2 30 nm scale b) Al_2O_3 20 nm scale c) Glass/ TiO_2 30nm scale d) Ni-W 200 nm scale.

Figure 5.1 shows morphology of silicon thin films grown on different substrate following the recipe given in table 5.1, experiment number 7. Films on Si/SiO_2 and Al_2O_3 substrate have similar shaped circular grains with average grain size 30 nm. Grains on $Glass/TiO_2$ substrate are not circular in shape and average grain size is larger, about 100 nm. The crystalline grains on nickel substrate are rather different from the shapes observed in all other substrates. Grains are randomly oriented, merged together to form larger grains of 400 nm and in some portion a columnar growth is also observed.

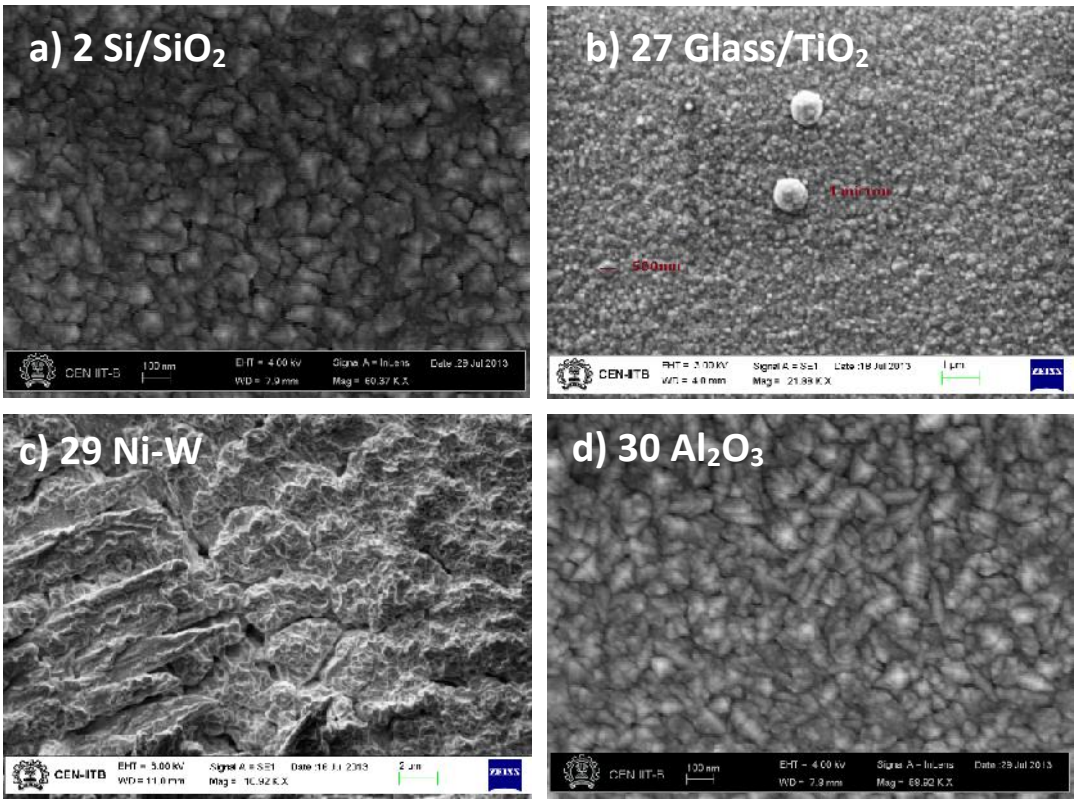

Figure: 5.2 SEM image of boron doped p-type poly crystalline silicon thick film on a) Si/SiO_2 b) $Glass/TiO_2$ c) Ni-W d) Al_2O_3 substrates.

Figure 5.2 shows morphology of thick polycrystalline silicon film grown on different substrate following the recipe given in Table 5.1, experiment number 8. Films grown on Si/SiO_2 and Al_2O_3 substrates have grain shapes similar to those observed in the case of intrinsic silicon film (chapter 4, section 4.4.3). Average grain size of 100 nm is observed on both substrates with a directional growth as shown in x-ray diffraction analysis in this chapter (section 5.4.5). Grains on $Glass/TiO_2$ have average size of 100nm.

Grains on nickel substrate look different though. Grains are merged, two to three micron in size. Sharp pointed four micron features are observed which is due to the contribution from the substrate effect [1].

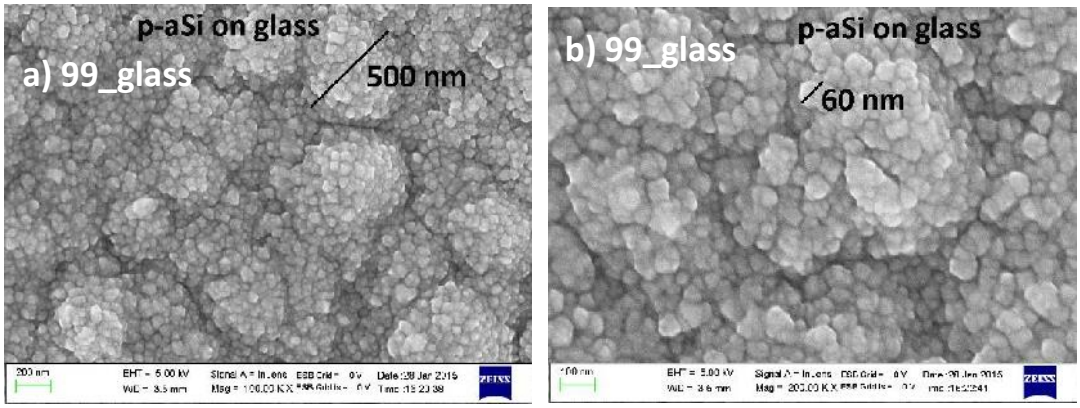

Figure 5.3: SEM image of sample 99_FTO/Glass boron doped p-type amorphous silicon film grown on polycrystalline on glass substrate. Magnification a) 100 KX b) 200 KX.

Morphology of p-type boron doped amorphous silicon (sample 99_FTO/Glass) films grown on polycrystalline silicon on glass substrate is shown in figure 5.3. The recipe for the growth of boron doped amorphous silicon on sample 99_ FTO/Glass is identical to the recipe shown in table 5.2, experiment number 27. The detailed recipe given in table 7.2, chapter 7. It shows grains are well merged, circular in shape of 60 nm average size. Small grains get accumulated to form larger aggregates; aggregates as large as 500 nm can be seen. The morphology seen here could be the result from the underlying polycrystalline silicon film on which the amorphous layers have been grown.

5.4.2 Thickness measurement

Stylus surface profiler step height measurement for the thickness and roughness analysis of p-type boron doped polycrystalline silicon film was performed as shown in figure 5.4. The growth conditions and thickness data tabulated for silicon film on each substrate are given in the section 5.3.

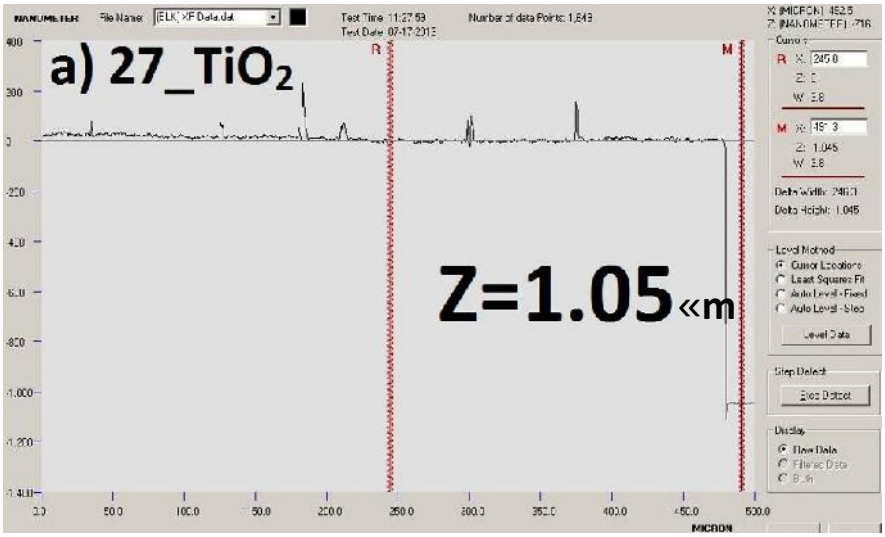

Figure 5.4: Stylus surface profiler step height measurement of p-type polycrystalline silicon film on Glass/TiO_2 substrate.

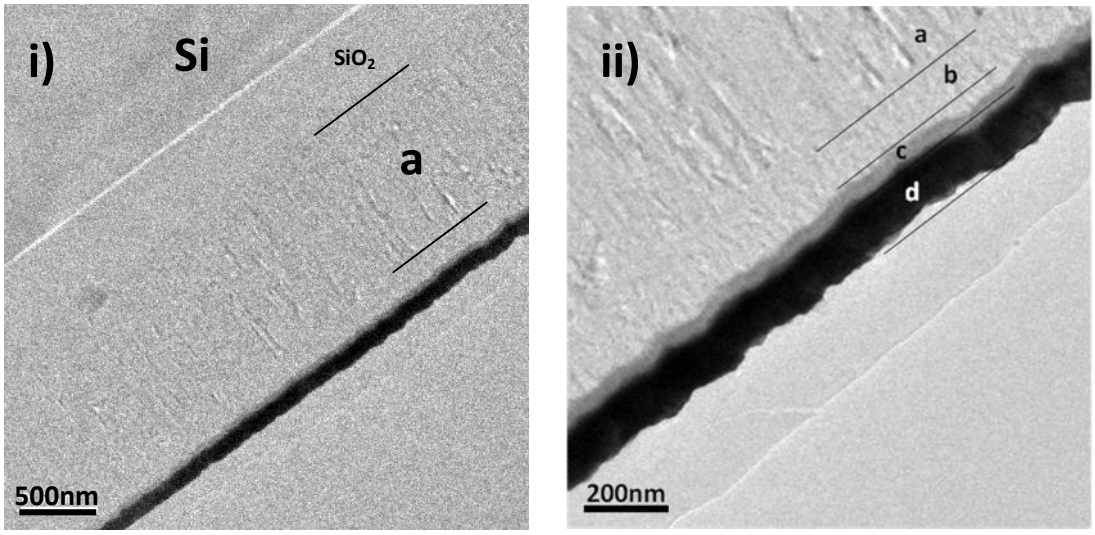

Figure 5.5 Cross section transmission electron microscope image of 39_Si/SiO_2 i) complete structure ii) Top amorphous layers.

In our study we observed, thickness of silicon film increases with the increase in silane concentration for the same period of time. The roughness of silicon film on TiO_2 substrate is around 100 nm. Knowing the total duration of growth we have estimated average growth rate is about 7 A° /sec.

Cross section transmission electron microscope (X-TEM) imaging was performed on sample 39_Si/SiO_2 and 96_Si/SiO_2 with all the sub-layers synthesized according to the process outlined in table 5.2. From X-TEM imaging, thickness of each layer is clearly observed in figure 5.5 & 5.6. The labels a, b, c, d, shown in both figure 5.5 & 5.6 correspond to different layers as follows: a) intrinsic polycrystalline silicon layer about 1 micron, b) boron doped amorphous silicon, c) chromium layer of 30 nm and d) gold layer of 80 nm . The chromium and gold layers are deposited just prior to the TEM sample preparation to protect the grown silicon layers. Thickness of the boron doped amorphous silicon is measured about 100nm from figure 5.5b and 75 nm from figure 5.6b.

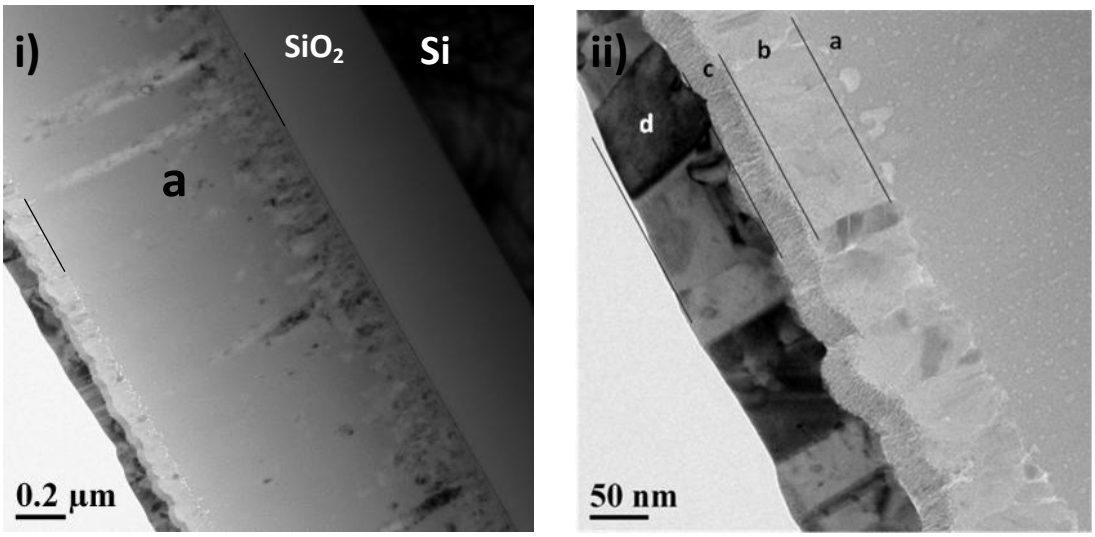

Figure 5.6 Cross section transmission electron microscope image of 96_Si/SiO_2 i) complete structure ii) Top amorphous layers.

5.4.3 Resistivity analysis

Sheet resistivity and bulk resistivity of the films are measured using four point probe setup for boron doped silicon film on Si/SiO_2, glass and sapphire substrate is shown in table 5.3. Relatively higher resistivity observed for thick poly crystalline silicon film on $2\_Si/SiO_2$ and $30\_Al_2O_3$ substrate compare to the thin p-type silicon film grown on same substrate. This is due to reducing hydrogen dilution used during thick film growth to maintain the process pressure constant.

Sheet and bulk resistivity is evaluated for the boron doped amorphous p-type silicon film on Si/SiO_2 and glass substrates as shown in table 5.3. We see that the sheet resistance is nearly 10 times larger for the sample $96\_Si/SiO_2$ in comparison to the sample $39\_Si/SiO_2$. Since the main difference between these two samples is the duration of growth of the boron doped amorphous layer, we believe that thickness of the boron doped amorphous layer is 10 times smaller in sample $96\_Si/SiO_2$ in comparison to the boron doped amorphous layer in sample $39\_Si/SiO_2$. No I-V data was taken for p-type silicon film on nickel and $Glass/TiO_2$ substrates using four probe setup because these substrates were having back conducting metal.

Table 5.3: Resistivity of boron doped silicon thin film on Si/SiO_2, Al_2O_3 and glass substrates.

Sample name	Voltage Volt (V)	Current Amp (I)	Sheet resistance =V/I*4.532 ohm/square	Thickness cm	Resistivity Ohm-cm
Polycrystalline silicon film					
$18\_Si/SiO_2$	1.35	1×10^{-2}	6.12×10^{2}	2.18×10^{-5}	1.33×10^{-2}
$24\_Al_2O_3$	1.67	1×10^{-2}	7.6×10^{2}	2.18×10^{-5}	1.65×10^{-2}
$2\_Si/SiO_2$	1.3×10^{-4}	1×10^{-6}	5.9×10^{2}	1.1×10^{-4}	6.48×10^{-2}
$30\_Al_2O_3$	1.5×10^{-4}	1×10^{-6}	6.8×10^{2}	1.1×10^{-4}	7.48×10^{-2}
Amorphous silicon film					
87_Glass	5.5×10^{-2}	1×10^{-6}	2.5×10^{5}	1.0×10^{-5}	2.5
$39\_Si/SiO_2$	7.4×10^{-2}	1×10^{-6}	3.4×10^{5}	1.0×10^{-5}	3.4
$96\_Si/SiO_2$	4.8×10^{-2}	1×10^{-7}	2.8×10^{6}	1.0×10^{-6}	2.2

5.4.4 Reflectance spectrum analysis

Reflectance measurement allows us to evaluate the response of the boron doped silicon film under illumination of white light. Usually for photovoltaic application the silicon film should absorb most of the light under visible spectrum. In our case we did not use any anti reflection coating nor have we used any substrate texturing for the reduction of reflection of light from the top surface. Applying these two processes we can reduce the reflection significantly.

In this section, we present measurements of reflectance spectra measured on the as-deposited thin and thick silicon films.

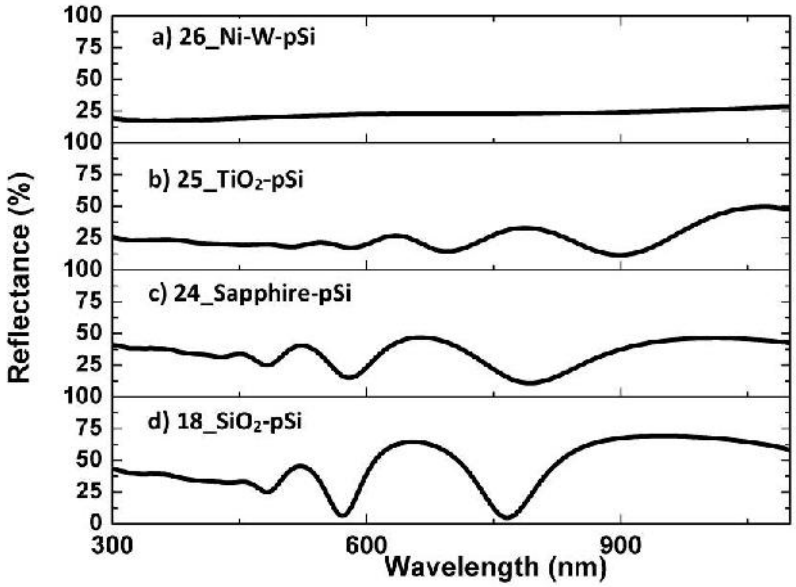

Figure 5.7: Reflectance spectrum under UV-VIS-NIR range using integrating sphere method of boron doped p-type silicon thin film on a) 26_ Ni-W b) 25_Glass/TiO_2 c) 24_ Al_2O_3 (d) 18_Si/SiO_2 substrates

Figures 5.7 & 5.8 shows reflectance spectra of p-type boron doped poly crystalline silicon i) thin and ii) thick films on Si/SiO_2, Glass/TiO_2, Al_2O_3, and Nickel substrates under near ultraviolet-visible-near infrared range. The mean value of reflectance is about 45% for thin silicon films deposited on Si/SiO_2 and sapphire substrates in the range 300 to 400 nm. Reflectance is about 25% for silicon films on Glass/TiO_2 and nickel for the same range. For wavelengths longer than 500 nm, we observe interference oscillations in the spectra of all

substrates except nickel. Thin film grown on nickel substrate was non uniform, columnar, randomly oriented as observed from the SEM images in the section 5.4.1.

For thick films (Figure 5.8), the overall reflection is 30% or lower. Interference oscillations are observed at wavelength longer than 500nm for silicon films on Si/SiO_2 and sapphire substrates. As expected, more oscillations are seen for the thick film in comparison to the oscillations observed in figure 5.7 for thin film. No interference fringes are observed for the film on TiO_2 and nickel substrate.

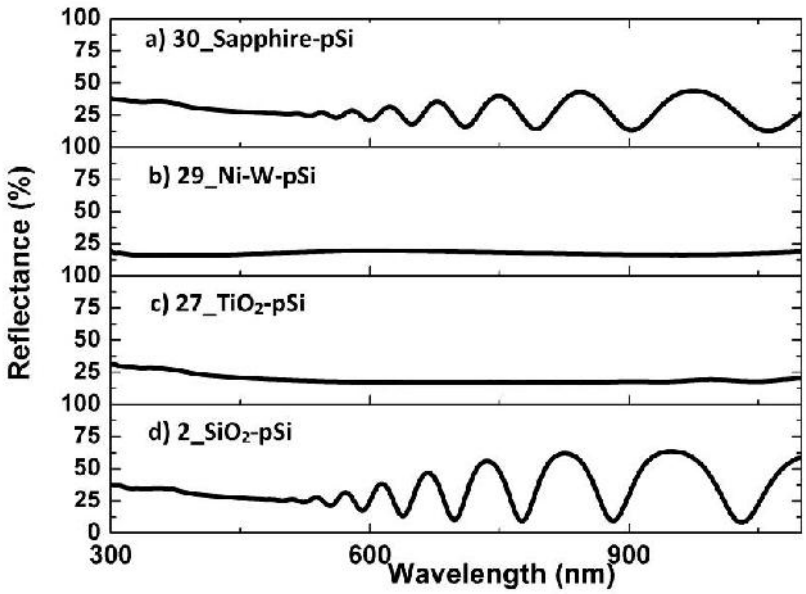

Figure 5.8: Reflectance spectrum of boron doped p-type silicon thick film under UV-VIS-NIR range using integrating sphere method on a) 30_ Al_2O_3 b) 29_ Ni-W c) 27_ Glass/TiO_2 (d) 2_Si/SiO_2 substrates.

5.4.5 Transmission spectrum analysis

Transmission spectrum allows us to evaluate the boron doped silicon film spectral response to the white light. Figure 5.9 shows transmission spectra for i) thin and ii) thick boron doped p-type silicon films on sapphire and TiO_2 on glass substrates. Interference oscillations are observed beyond 600nm and the spacing between the maxima is larger for the thin film compared to the spacing in the thick film, as observed above in the reflectance spectra. Thicker films (Fig 5.9 a&c) shows stronger absorption at wavelengths below 800nm compared to the thinner films (Fig 5.9 b&d). No transmission measurement is performed

for the silicon films deposited on Si/SiO_2 and nickel substrates, since these substrates themselves absorb light of wavelengths in the range of interest.

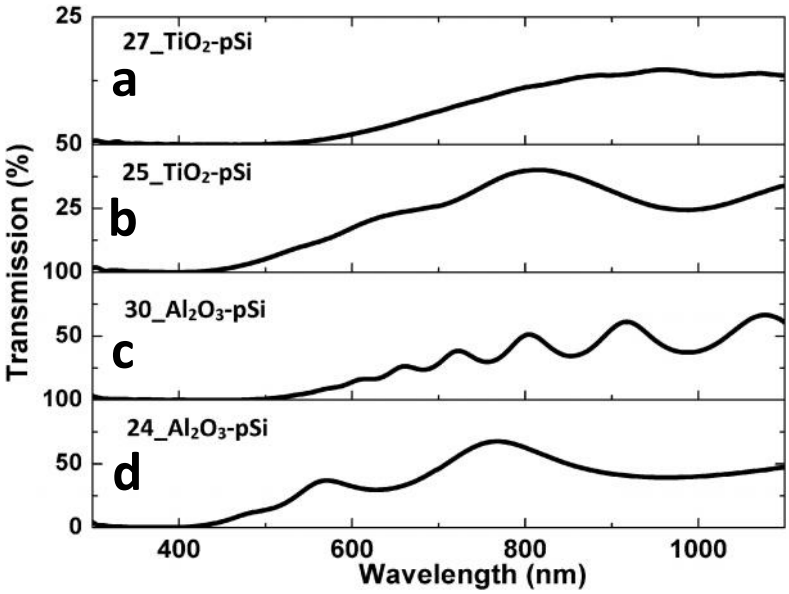

Figure 5.9: Transmission spectrum of boron doped p-type silicon thin film on b) 25_ Glass/TiO_2 and d) 24_ Al_2O_3 substrate; thick film on a) 27_ Glass/TiO_2 and c) 30_ Al_2O_3 substrates under UV-VIS-NIR range using integrating sphere method.

5.4.6 X-ray diffraction (XRD) analysis

Figure 5.10 shows plot of θ-2θ XRD scans for thin p-type polycrystalline silicon film grown on Si/SiO_2, Glass/TiO_2, Al_2O_3, and Nickel substrates. For analysis we have considered only peaks at 2θ values 28.5°, 47.5° and 56° for the polycrystalline silicon planes (111), (220) and (311) respectively. Peak corresponding to sapphire and nickel substrates are also seen in Figure 5.8 at 2θ equal to 44° and 51° respectively. On all four substrates we observed another peak at 2θ equal to 27° close to 2θ equal to 28.5° for thin film only. These peaks are merged in case of thick film. For thin film no preferred crystal orientation was observed.

Figure 5.11 shows plot of θ-2θ XRD scans for thick p-type polycrystalline silicon film grown on Si/SiO_2, Glass/TiO_2, Al_2O_3, and Nickel substrates. With the increase in the silane concentration to make thick film, the peaks corresponding to (220) increased significantly for boron doped p-type poly silicon film for all four different substrates. The crystalline volume fraction increases which is shown in table 5.4. Variable grain parameters from peak

analysis are also given in table 5.5. In our case, the ratio of the I(220)/I(311) and the I(111)/I(311) peak heights have been used to monitor the evolution of the crystallographic texture. For thick poly crystalline silicon film (220) as preferred growth direction was observed.

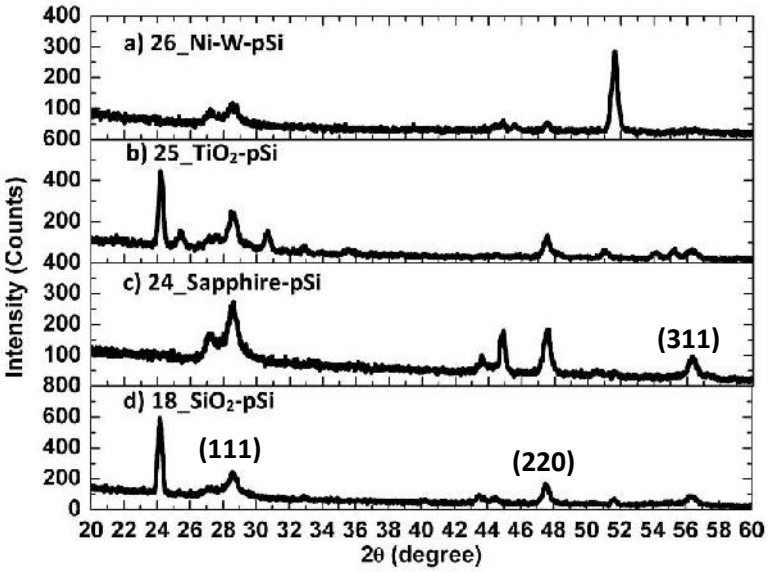

Figure 5.10: X-ray diffraction spectrum of boron doped p-type silicon thin poly crystalline film on a) 26_Ni-W b) 25_ Glass/TiO_2 c) 20_Sapphire (Al_2O_3) and d) 18_Si/SiO_2 substrate.

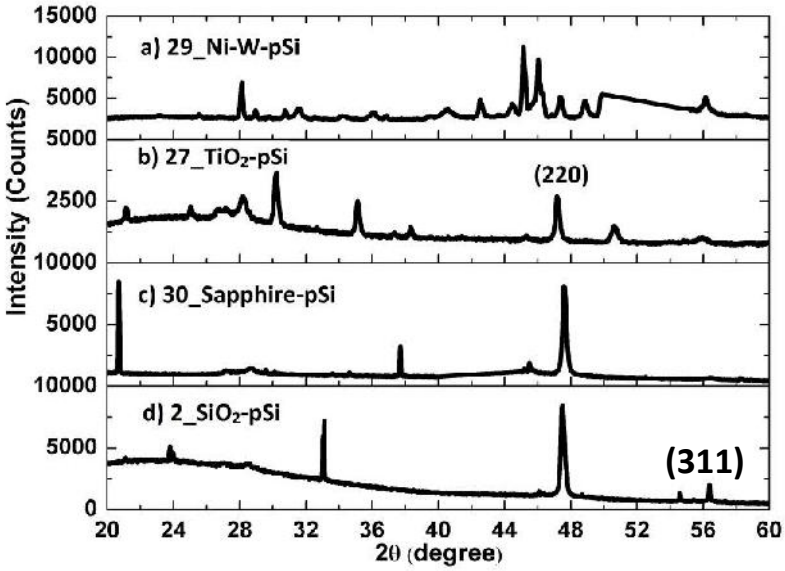

Figure 5.11: X-ray diffraction spectrum of thick poly crystalline silicon film on a) 29_Ni-W b) 27_ Glass/TiO_2 c) 30_Sapphire (Al_2O_3) and d) 2_Si/SiO_2 substrate

Table 5.4: XRD spectra data of boron doped p-type silicon thick films on Si/SiO_2, Sapphire, $Glass/TiO_2$ and Nickel substrates.

Sample name	(111) Count at 28.5^o	(220) Count at 47.5^o	(311) Count at 56^o	Intensity Ratio 111:220:311	Preferred Orientation
2_Si/SiO_2	410	7310	1435	01:18:04	(220)
27_$GlassTiO_2$	930	1832	264	03:07:01	
30_Al_2O_3	394	7166	171	02:42:01	
29_Ni-W	4318	2469	1770	03:02:01	

Table 5.5: XRD spectra data on Full width half maxima (FWHM) for grain size of poly silicon thick film on Si/SiO_2, Sapphire, $Glass/TiO_2$ and Nickel substrate for grain size and shape.

Sample name	(111) FWHM at 28.5^o deg	(220) FWHM at 47.5^o deg	(311) FWHM at 56^o deg	Grain size (diameter) for (220) orientation nm	Grain shape
Si/SiO_2	0.41	0.27	0.10	100	Spherical
$Glass/TiO_2$	0.51	0.30	0.83	400	
Sapphire	0.52	0.28	0.54	100	
Nickel	0.18	0.29	0.33	3000	

Under the geometrical conditions of the θ- 2θ X-ray scan, only those planes parallel to the sample surface satisfying Bragg's conditions will contribute to constructive interferences in the direction of reflection towards the x-ray counter. Thus a preferred (220) orientation means that in most of the crystallites the (220) planes are parallel to the sample surface and, hence, the growth of the crystallites occurs by piling up (220) planes.

5.4.7 TOF-SIMS analysis

Dopant concentration levels and their spatial and depth distribution are of major importance for the electrical performance of semiconductor devices. Due to its high detection sensitivity secondary ion mass spectrometry (SIMS) is an established method for the determination of concentration levels of dopant materials [2]. The SIMS apparatus used by us relies on the time-of-flight (TOF) detection technique.

Calibration of TOF-SIMS instrument was performed using a polished silicon wafer as reference in which boron was diffused at 1000°C for 20 minutes. Boron concentration versus depth profile of this reference sample was obtained using another (SIMS) apparatus [3] which was a standard. We have used this concentration profile as standard to convert the intensity counts obtained with our TOF-SIMS measurement. The conversion factor obtained for boron detection is 1 count =10^{16} atoms-cm^{-3} as estimated from Table 5.6.

Table 5.6: Calibration of TOF-SIMS for boron detection using SIMS profile of reference boron sample.

Depth in nm	Boron reference sample		
	Using standard SIMS		Using TOF-SIMS Intensity (Counts/sec)
	Intensity (Counts/sec)	Concentration Atoms-cm^{-3}	
250	1.2×10^4	1.2×10^{20}	1.1×10^4
500	7×10^3	7×10^{19}	5.5×10^3
750	2×10^3	2×10^{19}	1.3×10^3
1000	1.5×10^1	1.5×10^{17}	3×10^1

Depth profile was obtained by measuring the total crater depth with a surface stylus profiler. We have used oxygen (O_2) beam to sputter sample surface for boron detection with energy of 3000V for 20 sec in each step. Gallium (Ga) beam with energy of 15 kV known as liquid metal ion gun (LMIG) used probe the sample surface for 60 sec in each step. This is known as analyzing time. Duration of analysis was deducted from total time to calculate actual sputtering duration to evaluate the depth profile.

Neglecting the droop close to the surface, TOF SIMS analysis shows that concentration of boron near the top surface is about 2×10^{20} atom-cm^{-3}, and boron concentration can be reliably detected to as low as 1×10^{17}atoms-cm^{-3}. The depth profiling of the boron doped silicon film shown in Fig 5.12a, was done with sputtering rate of 0.38 nm/sec. The sputtering rate for the furnace diffused crystalline silicon data shown in Fig 5.12b, was 0.34 nm/sec.

Figure 5.12a shows concentration versus depth profile of sample 89_pSi prepared following the recipe given in table 5.2, experiment number 24. The profiling was performed using positive mode TOF-SIMS measurement. The concentration of boron is about 5×10^{20} atoms-cm^{-3} which remains nearly uniform over 150 nm and then starts to decrease as it reaches the underlying intrinsic poly silicon layers.

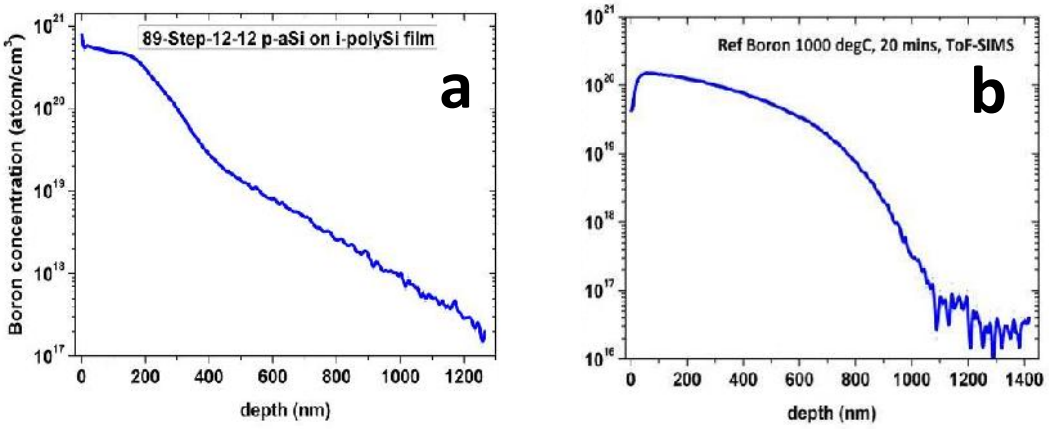

Figure 5.12: Concentration – depth curve of a) boron doped amorphous silicon film on intrinsic poly silicon film, b) standard boron doped p-type silicon sample prepared by boron diffusion furnace at 1000°C for 20 min.

5.4.8 Fourier transform infrared (FTIR) spectrum analysis

FTIR spectra of boron doped p-type poly crystalline silicon film on Si/SiO_2 and Al_2O_3 presented in the Figure 5.13. FTIR spectra exhibit a number of peaks corresponding to film as well as substrates. The spectrum analysis shows that Silicon film on Si/SiO_2 substrate shows stretching vibrations of oxygen in the Si-O-Si bonds at 1100 cm^{-1} and a feature around 2900 cm^{-1} is a contribution from Si-OH bonds [4].

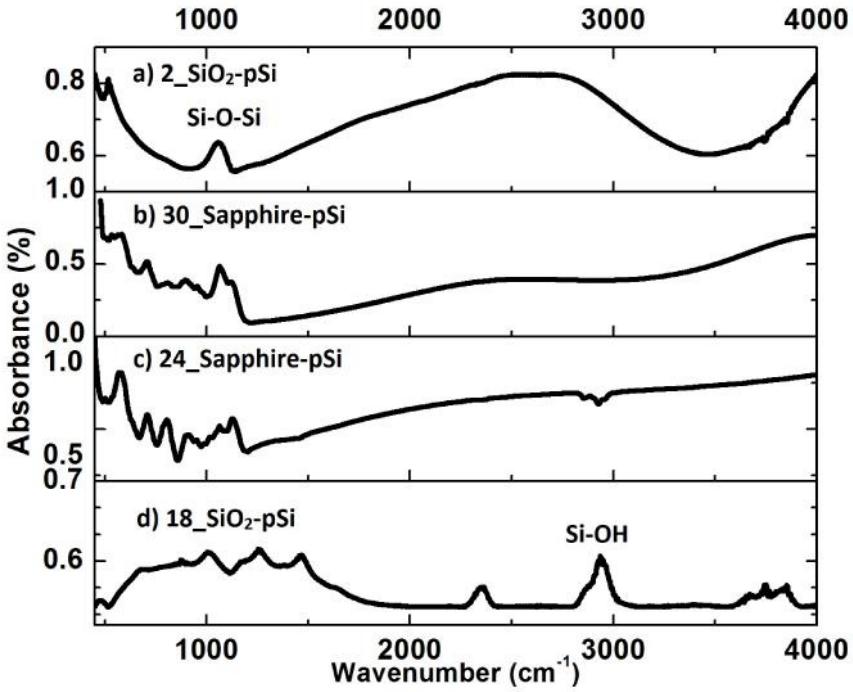

Figure 5.13: FTIR absorption spectrum of boron doped p-type polycrystalline silicon film on a) 2_Si/SiO_2 b) 30_Al_2O_3 c) 24_Al_2O_3 and d) 18_Si/SiO_2 substrate.

5.5 Discussion

Thin film solar cells of silicon have p-i-n structure, in which i-layer is the absorber and p and n layers provide the field for separating the photo-generated charge carriers. At the initial stage, we concentrated on experiments for the synthesis p-type polycrystalline silicon layers on a variety of substrates. At this stage, the structure of devices we would fabricate was not yet clear since we did not have access to a system for synthesizing n-type silicon layers and choice of substrate for device fabrication was also open. Thus, we concentrated on materials synthesis and characterization.

Our experiments showed that like the undoped films of silicon, 1 micron thick polycrystalline films of p-type boron doped films prepared at 600°C are preferentially oriented along (022) direction, although thinner films (about 200 nm) did not display high degree of orientation. We could achieve fairly high average growth rates (about 7A°/sec) for the thick films by increasing the silane content in the gas mixture 10 H_2 : 5 SiH_4: 5 B_2H_6 (5% B_2H_6 : 95% H_2) compared to about 2 A°/sec obtained from mixture using lower silane content 15 H_2 : 1 SiH_4: 5 B_2H_6 (5% B_2H_6 : 95% H_2). However, the average grain size remained small (about 100 nm) on Si/SiO_2 and Al_2O_3 substrates.

Resistivity of thin (about 200nm) films was in the range (1.3 – 1.7) x 10^{-2} Ω-cm, while in the thicker (about 1000 nm) films, the resistivity was larger in the range (6.5 – 7.5) X 10^{-2} Ω-cm. This may be understandable since the ratio of diborane to silane was reduced by factor of 5 in the thicker films compared to that in the thinner films. We do not have a measurement of boron concentration in these films. However SIMS measurements made on boron doped p-type amorphous silicon films grown with mixture 20 H_2: 1 SiH_4: 1 B_2H_6 (5%B_2H_6:95%H_2) gave boron concentration about 5 x 10^{20}/cm^3.

The p type amorphous silicon films were prepared at lower temperature of 200°C on top of undoped polycrystalline silicon deposited on glass and Si/SiO_2 substrates. We have grown p-type a-Si:H of resistivity (2 – 3.5) Ω-cm. By this time, we had access to a system where we could deposit thin film of n-type silicon. This will be discussed in detail in the next chapter. With the availability of n-type silicon film, we have decided to use a structure p - aSi:H – undoped c-Si – n-µcSi for the device.

5.6 Reference

[1] http://www.evico.de/en/superconductor-material/textured-substrates

[2] B.G Svensson, M.K. Linnarsson, J. Cardenas and M. Petravic, Nucl. Inst. & Meth. B, Vol 136-138, p-1034, 1998.

[3] Karthik M, M.Tec thesis, Indian Institute of Technology Bombay, Mumbai, India, 2014.

[4] M. Porrini, M.G. Pretto, R. Scala, A.V. Batunina, H.C Alt, R.Wolf, 'Measurement of boron and phosphorous concentration in silicon by low temperature FTIR spectroscopy', Appl. Phys. A 81, 1187-1190, 2005.

[5] Terborg R. and Rohde M.: Microscopy and Microanalysis 14, s-2, p-1166 2008.

[6] Abmann A. and Wendt M.: Spectrochim. Acta 58, p711–716, 2003.

Chapter 6

Synthesis of n-type silicon film

6.1 Introduction

In this chapter we shall describe our experiments on the synthesis of n-type silicon film using phosphorus as the source for impurity doping. Synthesis of n type silicon film was challenging since initially we did not have access to a silane system fitted with phosphine precursor. So, we decided to synthesise undoped polycrystalline silicon films, as described previously, and convert them to n type by doping. Terms intrinsic silicon films and undoped silicon films are used interchangeably in this chapter. We tried mainly two schemes for doping. These were: i) phosphorus ion implantation followed by laser annealing [1], and spin-on phosphorus dopant (SOD) deposition followed by thermal/laser drive in [2,3]. An extensive study was carried out to determine the laser dosage required to remove the ion induced damage using Nd:YAG continuous wave 1064 nm infrared laser [4,5]. Sheet resistivity measurement was used for quick evaluation of laser annealed phosphorus doped n-type silicon film. Structural, optical and material characterizations were also done on some films. In addition, laser induced crystallinity of silicon film was investigated using confocal Raman spectroscopy and 3D Raman imaging tool. Towards the end of these doping experiments, we were able to access a HWCVD system fitted with phosphine for synthesis of phosphorus doped n-type silicon films. Experiments done with these films are also described.

6.2 Substrates

Substrates used in this work include : i) Si/SiO_2 substrate (Silicon wafer resistivity 1-5 ohm-cm, thickness 275 micron) with 160 nm silicon dioxide layer grown by using wet oxidation, ii) alkali free borosilicate glass and FTO coated glass substrates. Single side polished sapphire (Al_2O_3) substrates were also used [6]. Details of substrate preparation and cleaning process are further discussed in Appendix II.

6.3 Phosphorus source for n-type silicon film

Table 6.1 lists the sample used in the ion implantation, spin-on dopant and HWCVD synthesis for n-type silicon.

Table 6.1: List of samples: Synthesis of n-type silicon film using ion implantation, spin-on dopant and HWCVD techniques on glass substrate.

Sample name	Process	Recipe
80_Glass 83_Glass 84_Glass 91_Glass/FTO 93_Glass/FTO	Ion implantation	Phosphorus ion implanted on one micron thick intrinsic poly silicon film
61_Glass 66_Glass 74_Glass 78_Glass 90_Glass/FTO	Spin-on dopant (SOD)	Spin one micron phosphorus solution on one micron thick intrinsic poly silicon film
82_Glass	HWCVD	one micron thick intrinsic poly silicon film
87_Glass 98_Glass	HWCVD	180 nm phosphorus doped silicon film on glass

6.3.1 Ion implantation using 100kV ion implantation setup

Ion implantation has been the dominant tool for introducing dopants into the silicon crystal for over two decades, and this trend is expected to continue well into the future. In this process, the impurity ions are accelerated to kinetic energies ranging from a few keV to several MeV and are directed onto the surface of the semiconductor. As the ions enter the crystal, they give up their energy to the lattice atoms by means of electronic stopping and nuclear stopping, and they finally come to rest at some depth in the crystal. Figure 6.1 shows reference plots of projected range and straggle for distribution of ions versus energy for several ions implanted into silicon [1,7].

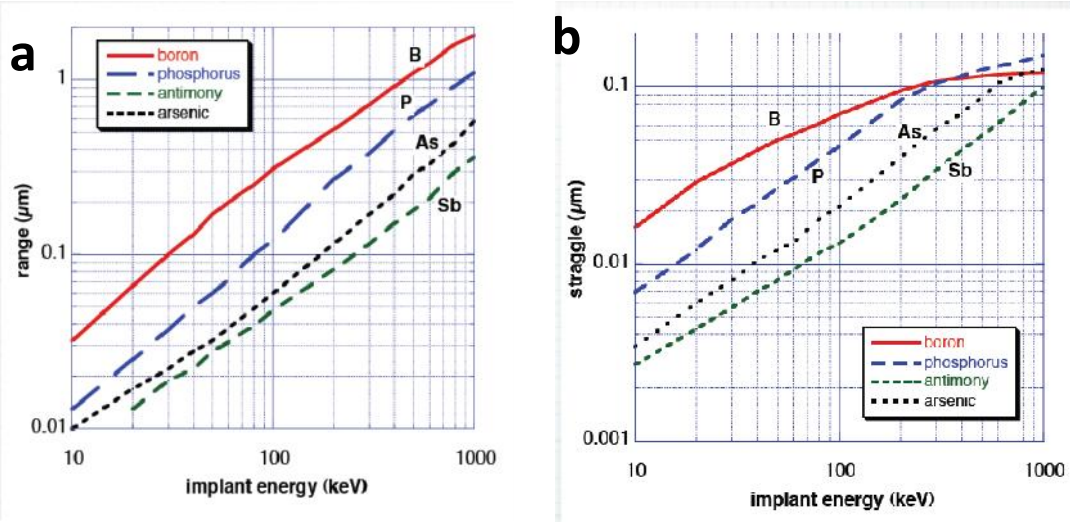

Figure 6.1 Reference graph of phosphorus ion implanted into silicon film for a) Range versus implant energy, b) Straggle versus implant energy [1,7].

We have used EATON NV 3204 medium current ion implantation system [8] for implanting 100keV phosphorus ions into intrinsic poly silicon film on glass substrate without any mask. Thickness of these poly silicon films on glass substrate was about one micron. The recipe for the growth of one micron intrinsic poly silicon is explained in section 4.3, chapter 4. Solid phosphorus Freeman type source was used to produce phosphorus vapour [9] in the ion implanter. The implant dose was 10^{15} ion/cm^2.

During implantation beam line vacuum was kept 1×10^{-6} mbar and sample chamber pressure was 2.66×10^{-6} mbar. The focused ion beam scans the sample surface in a highly controlled manner to achieve uniform implantation over the 1 cm $\times$ 2 cm sample area. We kept the sample stationary during the scanning. From Fig 6.1, for implantation with 100 keV phosphorus ions, we expect the range to be about 0.12 micron and straggle about 0.05 micron.

6.3.2 Spin-on dopant techniques

For spin-on dopant, we have used ethanol based phosphorus solution from Filmtronics Ltd. [10]. One micron thick layer of phosphorus dopant was coated by spinning the sample with the solution on it at 3000 rpm for 45 sec, followed by 15 minutes post baking at 250°C on a hot plate. There was no prebaking of sample before spinning dopant on it. The spinning and baking was performed under controlled atmosphere inside glove box. Standard atmospheric parameters in the glove box were: nitrogen pressure kept between 2 to 4 bar, amount of oxygen was between 1 to 2 ppm and moisture level maintained at 0.70 ppm to 1 ppm. We have used a small sealed steel chamber to take the sample outside the glove box. The samples were kept inside the same steel chamber during laser annealing.

6.3.3 HWCVD techniques

Thin phosphorus doped microcrystalline silicon layer was deposited in a HWCVD system different from the HWCVD system used for the undoped and p-type doped polycrystalline silicon. The growth was done at 350°C substrate temperature with a tantalum filament kept at a temperature 1650°C. Base pressure in the system was 1×10^{-6} mbar while process pressure was maintained at 6.6×10^{-2} mbar. The n-type doped microcrystalline silicon films were grown using gas flow ratio of SiH_4:H_2:PH_3 = 2:50:1 sccm. The growth duration was 32 minutes for 150 nm thick film and 45 minutes for 180 nm thick film.

6.4 Dopant activation

Dopant activation in the ion implanted samples and the spin-on dopant samples was done by i) thermal annealing and by ii) laser annealing.

6.4.1 Thermal annealing

We have used the same HWCVD chamber, which was used for the synthesis of undoped and p-type doped polycrystalline silicon films, for thermal annealing of ion implanted samples. Initially, we annealed the ion implanted polycrystalline silicon film on glass with 1900°C filament temperature for 30 min. During this high temperature annealing, there was no H_2 flow and temperature of substrate reached 750°C to 800°C. As a result, the glass substrate (93_FTO_Ion) softened and to deformed. We used hydrogen gas during the cooling of the substrate from 600°C to room temperature. Since there was deformation of the substrate during the thermal annealing process, we did not pursue further the thermal annealing option of dopant activation in the rest of the work.

Table 6.2: Thermal annealing of n-type silicon film on glass substrate using HWCVD system.

Sample name	Step	Substrate heater temp. (°C)	Filament temp. (°C)	Growth pressure (mbar)	Hydrogen (H_2) Gas flow (sccm)	Duration (minutes)
84_Glass/ Ion	Heating Cooling	750 600-200	1900 1864	2.5×10^{-6} 7.8×10^{-2}	No gas 20	30 45
93_FTO/ ion	Heating Cooling	800 800-120	1913 1902	2.5×10^{-6} 2.5×10^{-6}	No gas No gas	30 75
80_Glass/ Ion	Heating Cooling	750 750-200	1906 1887	1.5×10^{-6} 5.8×10^{-2}	No gas 20	30 45
98_Glass/ nSi film	Heating Cooling	750 750-200	1900 1886	9.1×10^{-6} 7.3×10^{-2}	No gas 20	30 45

6.4.2 Laser annealing

An infrared (IR) 1064 nm wavelength continuous wave (CW) fibre laser pumped with single diode laser by SPI lasers limited Germany [11], was used to anneal and dope intrinsic poly silicon films. The laser operated was operated in transverse electromagnetic mode (TEM 00) with a Gaussian beam profile and pushed at a frequency 10 kHz with power output adjustable in the range 1W to 25 W. Computer controlled x, y, z movement with a minimum line to line translation 5 μm by Scantech laser [12] was used to raster the beam. This arrangement allows us to control the movement of beam scan speed in the range of

10mm/sec to 100 mm/sec. A beam delivery optical cable and beam focusing lens with 58mm focal length focused the beam on to the sample with a 10 micron beam spot diameter in the focused condition.

Table 6.3: List of samples: Annealing and dopant activation of n-type silicon film on glass substrate using infrared continuous wave laser.

Sample	Scan area mm^2	Laser annealed Region	Laser pulse duration in µs	Laser fluence in J/cm^2	Scan speed cm/sec
61_Glass_SOD	7×12	R1	9.5	9.7	2
		R2	10	10.2	4
		R3	10	10.2	2
66_Glass_SOD	3×12	R1	9.5	9.7	4
	6.5×12	R2	9	9.2	4
74_Glass_SOD	10×4	R1	9	9.2	2
		R2	9.5	9.7	4
78_Glass_SOD	2.5×12	R4	9	9.2	1
90_Glass/FTO_SOD	3×8	R1	8.5	8.7	4
80_Glass_Ion	7×12	R1	10.5	10.7	6
83_Glass_Ion	7×12	R3	11	11.2	4
84_Glass_Ion	6×12	R1	10.5	10.7	4
		R2	10.5	10.7	2
		R3	10.5	10.7	3
91_Glass/FTO_Ion	3×4	R5	8.5	8.7	4
		R6			
87_Glass_nSi	3×8	R1	10	10.2	3
	8×14	R9	10	10.2	3

A red pointer beam, coincident with the IR laser beam, was used as reference to align the sample scan area before laser irradiation. Pulse duration and scan speed were two key parameters which we have varied to reach the required annealing condition. The calculation of laser fluence for 10 µs pulse duration is given in appendix I.

Samples were kept inside a nitrogen filled sealed container with a quartz window for laser irradiation during the annealing process. The packaging was performed in standard glove box where chamber pressure was 2 to 4 bar, oxygen content was 1 to 2 ppm and moisture level was 0.8 to 1 ppm. 99.999 % pure nitrogen (N_2) gas jet at 1.2 bar was used during the laser annealing to ensure the cooling of lens as well as the quartz window. Image of laser processing tool is presented in Appendix I.

6.5 Results

Results presented in this section include i) topographical characterization using optical and scanning electron microscope, ii) electrical characterization using four point probe set up, iii) reflectance and transmission measurement using UV-VIS-NIR spectrometer, iv) X-ray diffraction performed for evaluation of crystalline quality and orientation of phosphorus doped silicon film, v) depth distribution of phosphorus performed using time of flight secondary ion mass spectroscopy. We have also performed Fourier transform infrared spectroscopy for evaluation of Si-H, Si-OH, Si-O-Si stretching bonds.

6.5.1 2D optical imaging

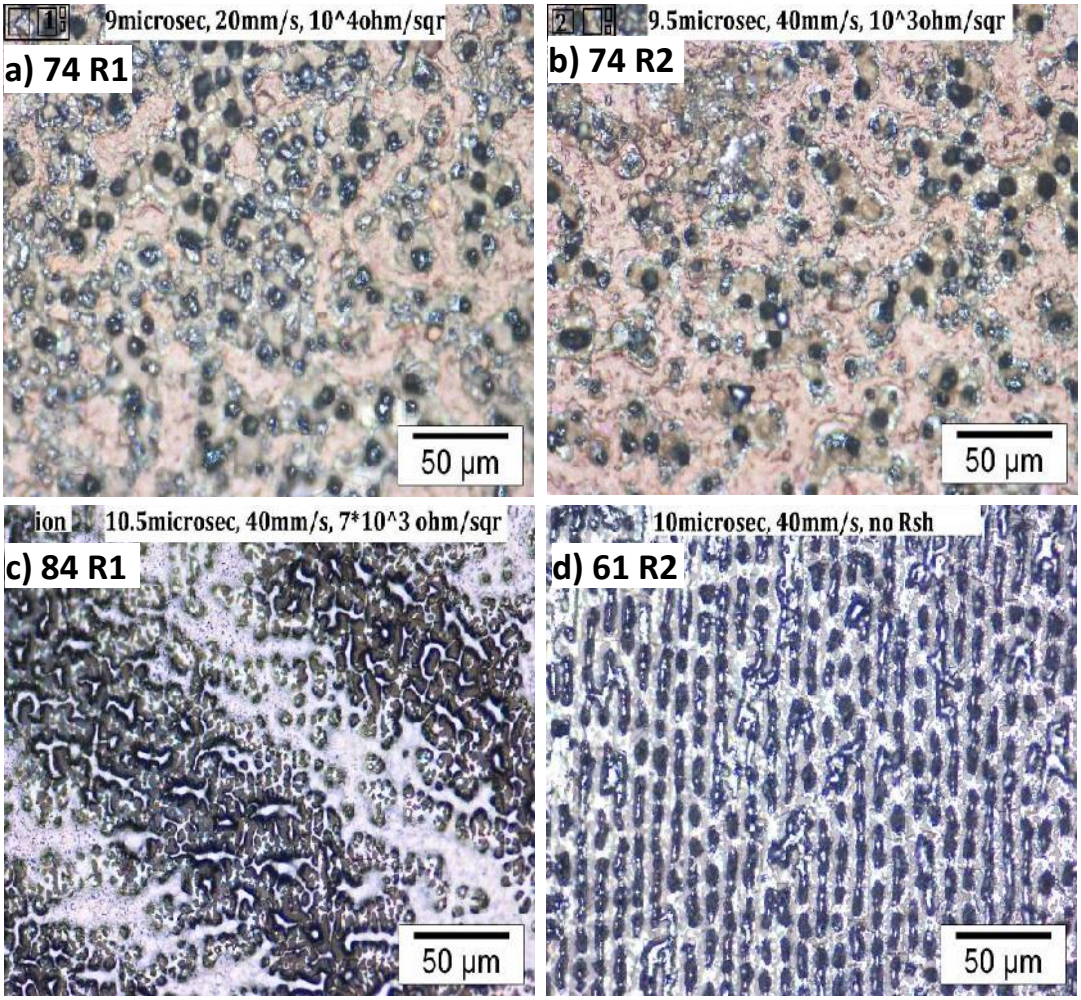

Figure 6.2: 2D optical microscope image of laser annealed phosphorus doped silicon film on glass substrate prepared by spin-on dopant a) 74_R1, b) 74_R2, d) 61_R2 and c)84_R1 prepared by ion implantation.

Figure 6.2 show surface morphology of polycrystalline silicon film using 2D optical dark field images just after laser irradiation of i) samples coated with spin-on dopant film and ii) ion implanted sample. Laser annealing is performed for varying laser pulse duration and scan speed. Lower scan speed and longer pulse duration allows more laser irradiation absorption into the silicon film. Higher scan speed and shorter pulse duration allows less absorption of laser into the silicon film. We have optimized the two variables and reduced the resistivity of the n-type silicon film which we will discuss in resistivity analysis section 6.5.10. The average size of dark spots estimated from images in Fig 6.2 a&b is 10 micron which is close to the diameter of laser beam. These dark spots are randomly distributed over the entire scanned region and correspond to the region where laser absorption is highest.

For ion implanted silicon film on glass, the optimum condition was pulse duration 10.5µs and scan speed 4cm/s. For spin-on dopant on silicon film, the optimum condition was pulse duration 9.5µs and scan speed 4cm/s. Figure 6.2d, shows very regular laser scanning line, but electrical measurement showed the film to be highly resistive. 2D optical microscope image gives visible idea of laser annealing process apart from electrical measurement. Our observations lead us to the conclusion that the laser annealing process for processing of thin silicon films is very critical from the device point of view.

6.5.2 3D optical imaging

3D optical image allows us to analyse the surface roughness of laser irradiated n-type silicon film on glass substrate. These images were taken with motorized vertical axis zeta 3D microscope covering an image area of (71×95) μm^2 shown in Figure 6.3. Average roughness of n-type film is 10 nm on glass substrate before laser annealing shown in figure 6.3c. Laser irradiation changes the surface morphology as the silicon film melts and solidifies which creates hills and valleys as the melting and solidification takes places randomly. Average roughness, peak width and z-axis scanning parameters are presented in table 6.4.

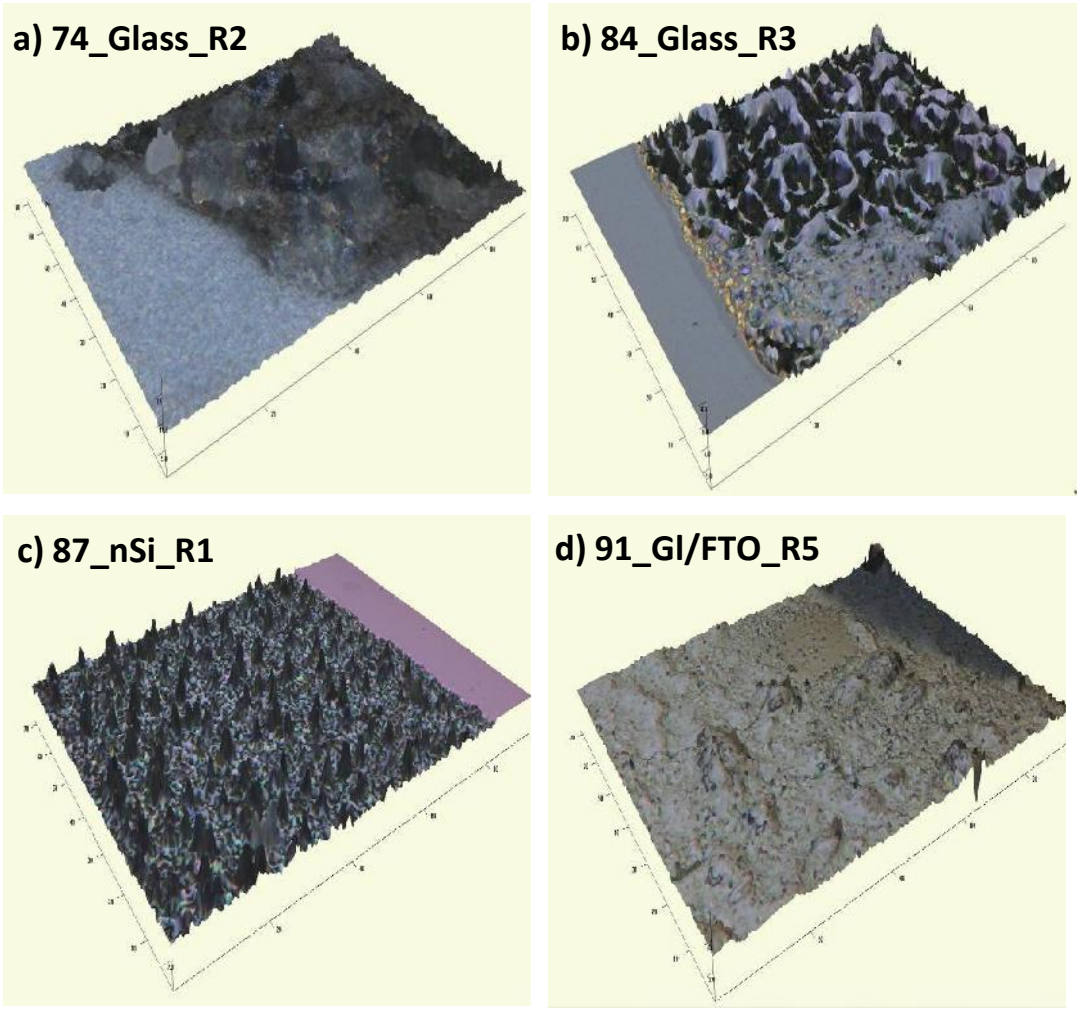

Figure 6.3 100x magnified 3D optical image with laser annealed silicon film. a) 74_Glass_R2 spin-on-phosphorus dopant b) 84_Glass_R3 phosphorus ion implanted c) 87_nSi_R1 n-type silicon film using HWCVD d) 91_Glass/FTO_R5 phosphorus ion implanted.

Total thickness of as-grown silicon film on glass substrate is one micron as mentioned earlier in section 6.3, table 6.1. From the data presented in the above table, it is seen that the laser caused significant texturing of the film on glass surface which is larger than the thickness of silicon film. It is possible that laser annealing cause melting and islanding of silicon during solidification on top of the glass surface. At this stage we cannot rule out local heat causing melting of glass surface as well. For sample 91_Glass/FTO, where the silicon film on top of FTO coated glass (Fig 6.3d), the texture morphology is different from that observed for the silicon film on glass (Fig 6.3 a,b,c).

Table 6.4: Numerical data from 3D optical image analysis of laser annealed phosphorus doped silicon film on glass substrate.

Sample name	Laser recipe	Average peak height in µm	Average peak width in µm	Motorized Z-axis step movement in µm	No. of steps	Total range in Z-axis movement of lens (µm)
74_Glass_SOD_R2	9.5µs,4cm/s	6.4	0.45	0.044	400	17.6
84_Glass_ION_R3	10.5µs,3cm/s	5	0.34	0.029	300	8.7
87-nSi_HWCVD-R1	10µs,3cm/s	3	0.34	0.019	300	5.7
91-Gl/FTO-ION-R5	8.5µs,4cm/s	3	0.63	0.020	300	6

In particular, the peak width is larger, which means less texturing occurred due to laser irradiation. In this case the conducting FTO at the back of silicon will reflect some of the laser light and reduce the laser energy entering glass. Presence of conducting FTO may also spread the heat laterally. Understanding this will require a detailed optical/thermal modelling of the process. We conclude that 3D optical microscope images give an idea about laser irradiation induced surface texturing of silicon film deposited i) directly on glass and ii) on FTO coated glass .

6.5.3 Scanning electron microscope (SEM) image analysis

Figure 6.4 shows SEM image of phosphorus doped n-type micro crystalline silicon film grown on glass substrate using HWCVD before and after laser irradiation. Significant changes are observed for the film before (6.4a) and after (6.4b) laser irradiation. Before laser irradiation grains were random in shape and average grain size was 400nm shown in Figure 6.4a. The film irradiated with laser fluence of 10.2J/cm^2 causes the grains to melt, re-crystallize and to become 10 µm size large. From sheet resistivity measurement as described in the section 6.5.9, the improvement of conductivity due to laser irradiation is also observed.

This reference work established that with the laser system, it is possible to anneal silicon film on glass with an increase in the conductivity of silicon film.

Table 6.5: List of samples: Laser parameter for phosphorus doped silicon film on glass substrate of SEM images given in Fig 6.4, 6.5 and 6.6.

Sample	Laser scan area mm^2	Laser annealed Region	Laser pulse duration in µs	Laser fluence in J/cm^2	Scan speed cm/sec
66_Glass_SOD	6.5×12	R2	9	9.2	4
74_Glass_SOD	10×4	R1	9	9.2	2
90_Glass/FTO_SOD 83_Glass_Ion	3×8 7×12	R1 R3	8.5 11	8.7 11.2	4 4
84_Glass_Ion	6×12	R2	10.5	10.7	2
91_Glass/FTO_Ion	3×4	R6	8.5	8.7	4
87_Glass_nSi	8×14	R9	10	10.2	3

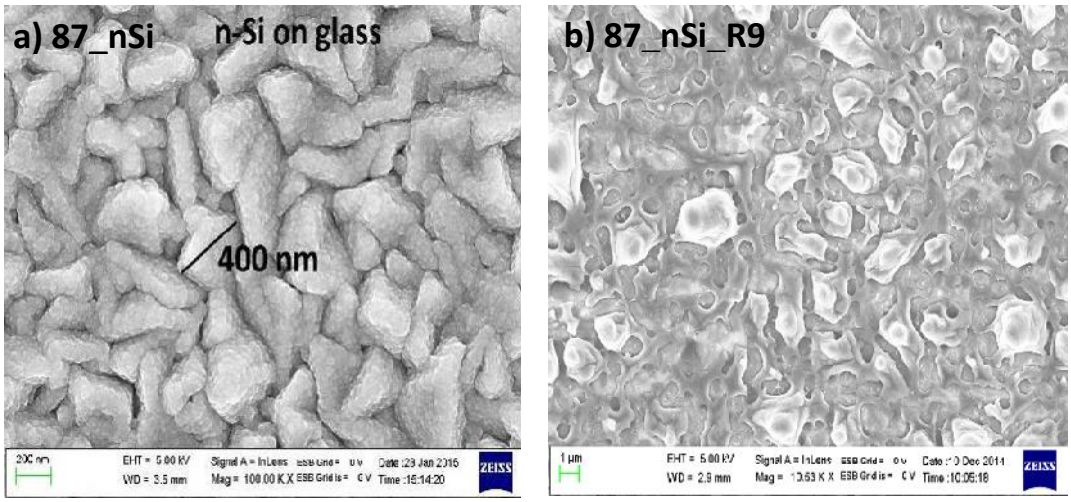

Figure 6.4: SEM image of n-type a) 87_nSi micro crystalline silicon thin film on glass substrate b) 87_nSi_R9 laser annealed n-type micro crystalline silicon thin film on glass.

Figure 6.5 shows SEM images of silicon films coated with spin-on dopant and subjected to laser irradiation under melting condition. The estimated temperature of melting region is expected to be in between 1000°C to 1400°C where the melting point of poly silicon is about 1410°C [13]. It is seen that grains have melted, re-grown and merged to form larger grains due to the laser irradiated with fluence of 10 J/cm^2. The grains as large as 1 to 10 μm size are achieved by the laser irradiation processes for silicon film on glass and FTO coated glass substrates respectively.

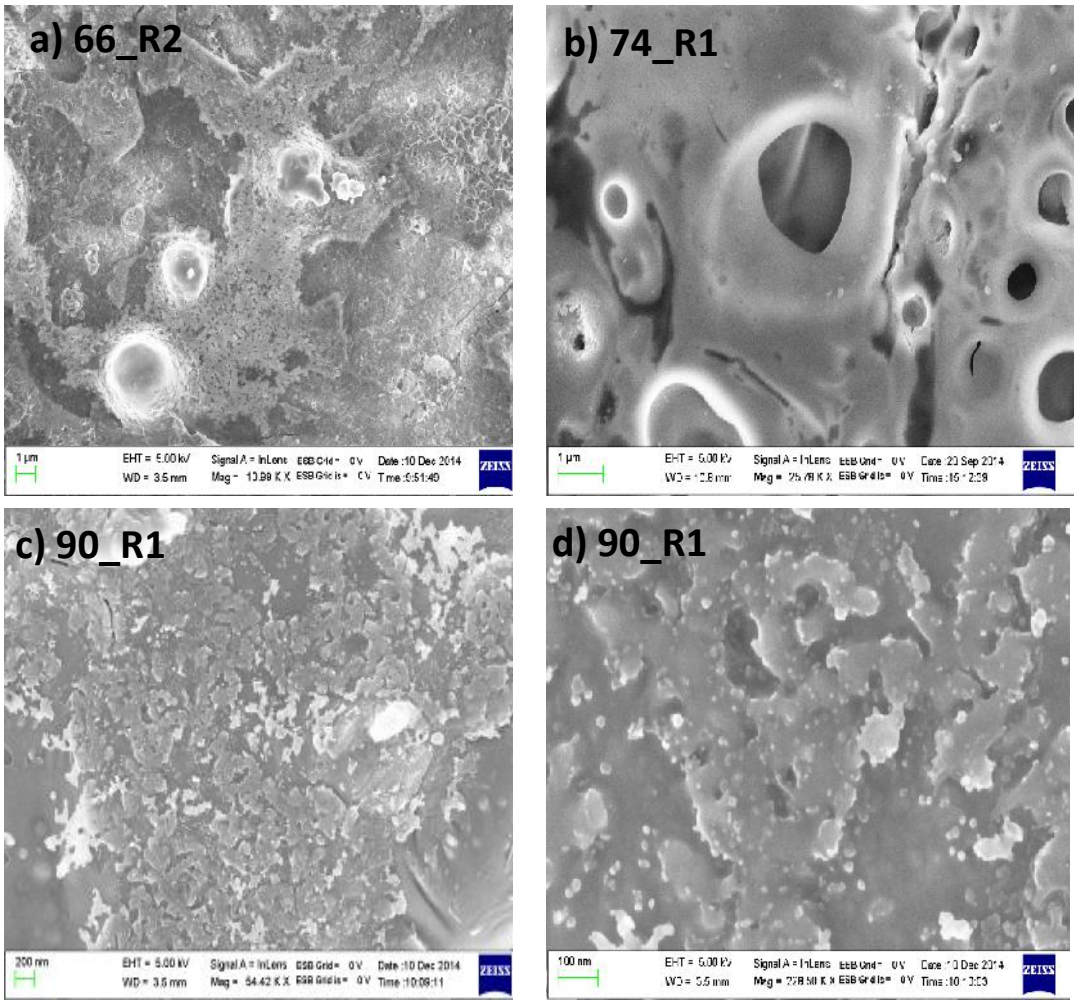

Figure 6.5 SEM image of laser annealed spin phosphorus doped (SOD) silicon film on glass substrate a) 66_R2 b) 74_R1 and on FTO coated glass substrate, c) 90_R1 54 KX, d) 90_R1 228 KX magnification.

Figure 6.6 shows SEM image of morphology of silicon film implanted with phosphorus ions and subjected to laser irradiation. It shows non-uniformly distributed island which are connected. This could be due to melting and re-crystallization processes occurring due to laser annealing.

Thus the n-type silicon obtained by the laser treatment of i) ion implanted silicon film, and ii) SOD coated silicon film is quite non-uniform and does not have the device like quality. Further work is necessary in view of reports in the literature [14].

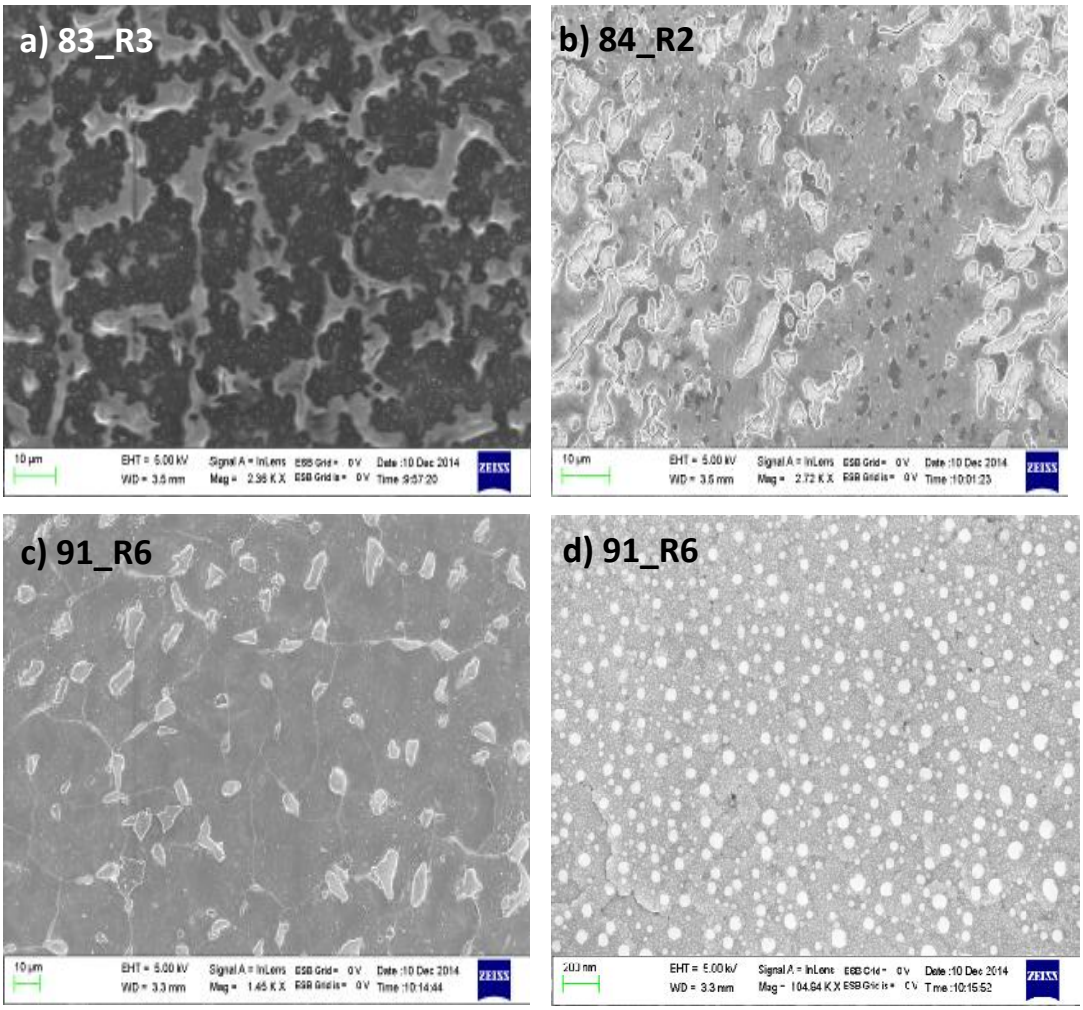

Figure 6.6 SEM image of laser annealed phosphorus ion implanted silicon film on glass substrate a) 83_R3 b) 84_R2 and on FTO coated glass substrate c) 91_R6 1.45KX d) 91_R6 104 KX magnification.

6.5.4 X-ray diffraction analysis

In this section, we compare the x-ray diffraction pattern obtained from as-deposited silicon films and after laser treatment of i) ion implanted silicon films and ii) SOD films

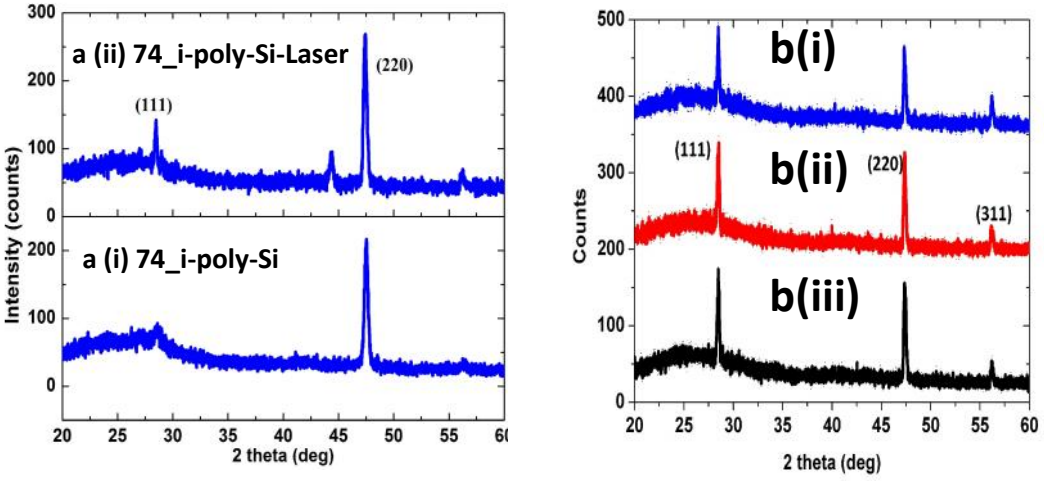

Figure 6.7: X-ray diffraction spectrum of phosphorus doped i-poly Si film on glass a) (i) 74_ intrinsic poly silicon film on glass, (ii) 74_R2, spin-on phosphorus dopant, laser annealed (9.5µs, 4cm/s) b) phosphorus ion implanted, laser annealed silicon film (i) 83_12µs, 4cm/s, (ii) 83_11.5µs, 4cm/s, (iii) 83_11µs, 4cm/s.

Figure 6.7 shows X-ray diffraction measurement done on laser annealed n-type silicon film on glass substrate. Figure 6.7a(i) intrinsic poly silicon thin film grown on glass substrate shows a particular (220) directional crystalline growth. Figure 6.7a(ii) shows XRD scans of i-poly Si samples with spin-on phosphorus dopant after laser irradiation with fluence 9.7 J/cm^2 driving in the spin-on phosphorus dopant into the film.

Figure 6.7b shows XRD measurements of phosphorus ion implanted poly silicon film and subject to laser irradiation. Considering the laser annealing of ion implanted silicon film, the laser fluence 11.2, 11.7 and 12.2 J/cm^2 was used to achieve the melting condition. In comparison to the as-grown silicon films, the laser annealed samples lose the directional property. This is particularly obvious in the case of ion implanted samples where we can see the (111) and (220) both peaks are having intensity of same order. Thus, these films have become randomly oriented. This may be because there are no oriented nuclei to promote particular orientation during the process of laser induced melting and re-crystallization.

6.5.5 Raman spectroscopy

6.5.5.1 Raman analysis for Laser induced crystallinity

The Raman spectra for several samples have been recorded to quantify the crystallinity of intrinsic poly Silicon film as well as for laser treated films as shown in Figure 6.8. The penetration depth of 514 nm Raman laser beam is one micron into the film which is comparable to the thickness of the silicon film, this means the findings give us an overall behaviour with respect to the depth of the sample.

We have collected Raman spectrum using 20X objective lens. Raman peak position for intrinsic poly silicon film on glass is 519.4 cm^{-1} fig 6.8a, for spin coated laser annealed sample 517.6 cm^{-1} fig 6.8b and for ion implanted laser annealed sample 521.7 cm^{-1} fig 6.8c. The Raman peak shift towards the lower wavelength can be explained as the tensile stress in intrinsic poly silicon thin film. This deviation of peak position also attributed to the lack of complete crystallinity.

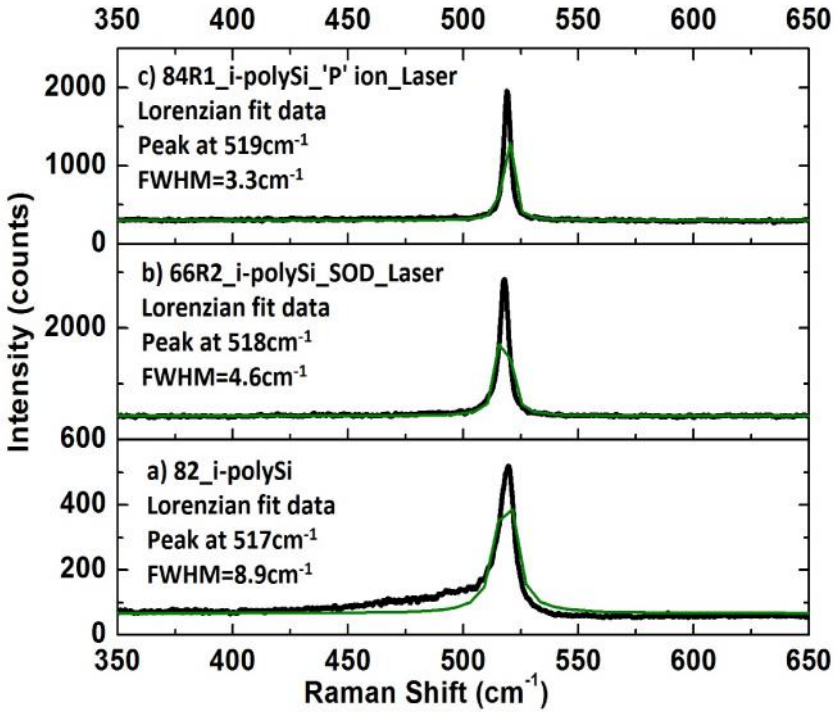

Figure 6.9: Confocal Raman spectrum of a) 82_i-poly silicon thin film on glass b) 66_R2 laser annealed n-type doped (Spin-on-dopant) silicon film on glass c) 84_R1 laser annealed n-type doped (ion implantation) silicon film on glass.

From fig 6.8a the continuous line is Lorentzian fitted curve for the spherical nano crystal. The Raman peak shift towards lower wavenumber (red shift) can occur because of several reasons. Tensile strain is known to red shift the Raman peak [15]. Disorder can lift the degeneracy of TO and LO modes and cause red shift.

6.5.5.2 Raman analysis for ion induced damage

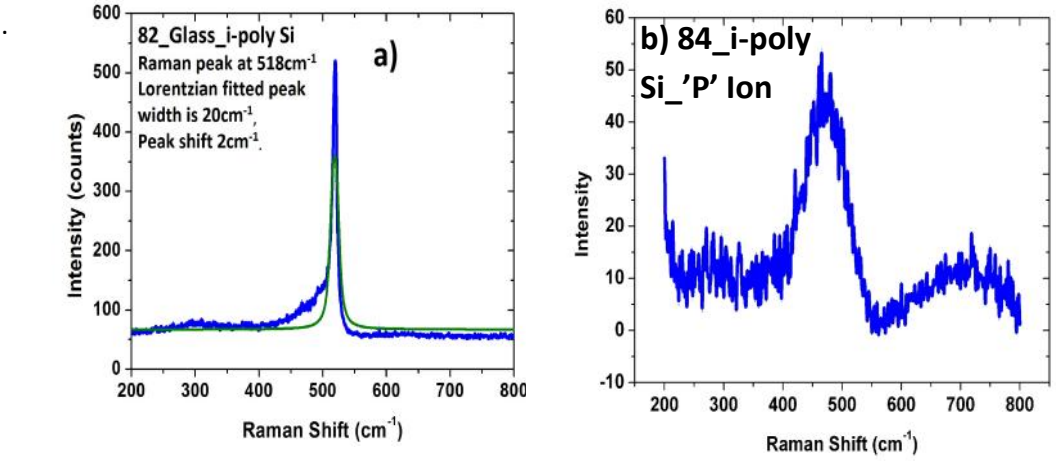

Figure 6.9: Confocal Raman spectrum of a) 82_i-poly Si film on glass substrate b) 84_i-poly Si-'P' Ion implanted.

Phosphorus ion implantation process causes phosphorus ion to penetrate the target by colliding and displacing the silicon atoms in its path. Both the incident ion and displaced host atom continues to cause further damage until they are stopped as the initial energy is spread over larger number of atoms by collisions. As a result after a complete process of ion implantation the initial polycrystalline silicon film become highly disordered in crystalline state. Eventually at a critical dose of ions, the film becomes amorphous [16].

Figure 6.9 shows Raman spectroscopy spectrum of intrinsic poly silicon film before and after phosphorus ion implantation. After phosphorus ion implantation Raman spectrum from figure 6.9b shows a broad Raman peak at 480 cm^{-1} which establishes the amorphous condition of the polycrystalline silicon film due to ion implantation. Figure 6.9a shows the Raman peak observed at 518 cm^{-1} before ion implantation.

6.5.6 Raman imaging

Raman imaging has been done for some selected samples to determine the spatial distribution of different forms of silicon in the film. This is done by integrating the counts in different wavenumber ranges as shown in Figs 6.10 (c, d, e, f) and Figs 6.11 (c,d) below.

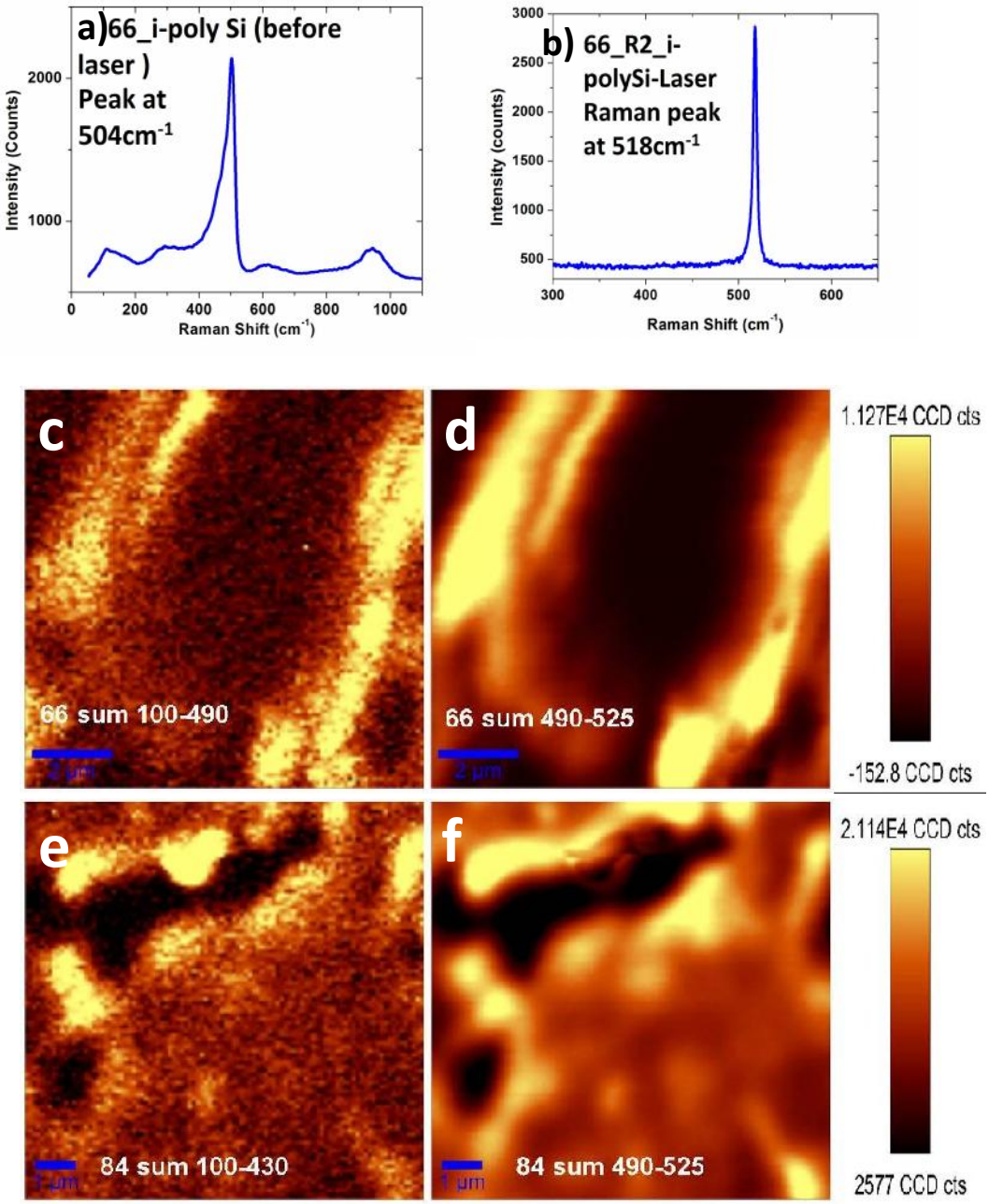

Figure 6.10 Confocal Raman spectrum of a) 66_i-poly Si before laser b) 66_i-poly Si after laser irradiation. Raman images of sum of intensity (counts) in the range 100-490 cm^{-1} in (c), 100-430 cm^{-1} in (e), 490-525 cm^{-1} in (d) and (f) of laser annealed n-type doped intrinsic poly silicon film on glass: for 66_R2 Spin-on-dopant, e & f) 84_R1 ion implanted.

Figure 6.10 a) and b) show typical Raman spectra of as grown n-type silicon film before and after laser irradiation. Figs 6.10 (c to f) are 10×10 micron Raman mapping for laser annealed crystalline silicon. Images are created by using sum of peak intensity from a range 100 to 490 cm^{-1} in Fig 6.10c, 100 to 430 cm^{-1} in Fig 6.10e; and from the sharp and symmetrical Raman band around 520 cm^{-1} (490 to 520 cm^{-1}) in Figs 6.10 (d and f). Raman peak intensity for amorphous silicon at wavenumbers less than 490 cm^{-1} is lower than the Raman intensity of crystalline silicon peak at around 520 cm^{-1}.

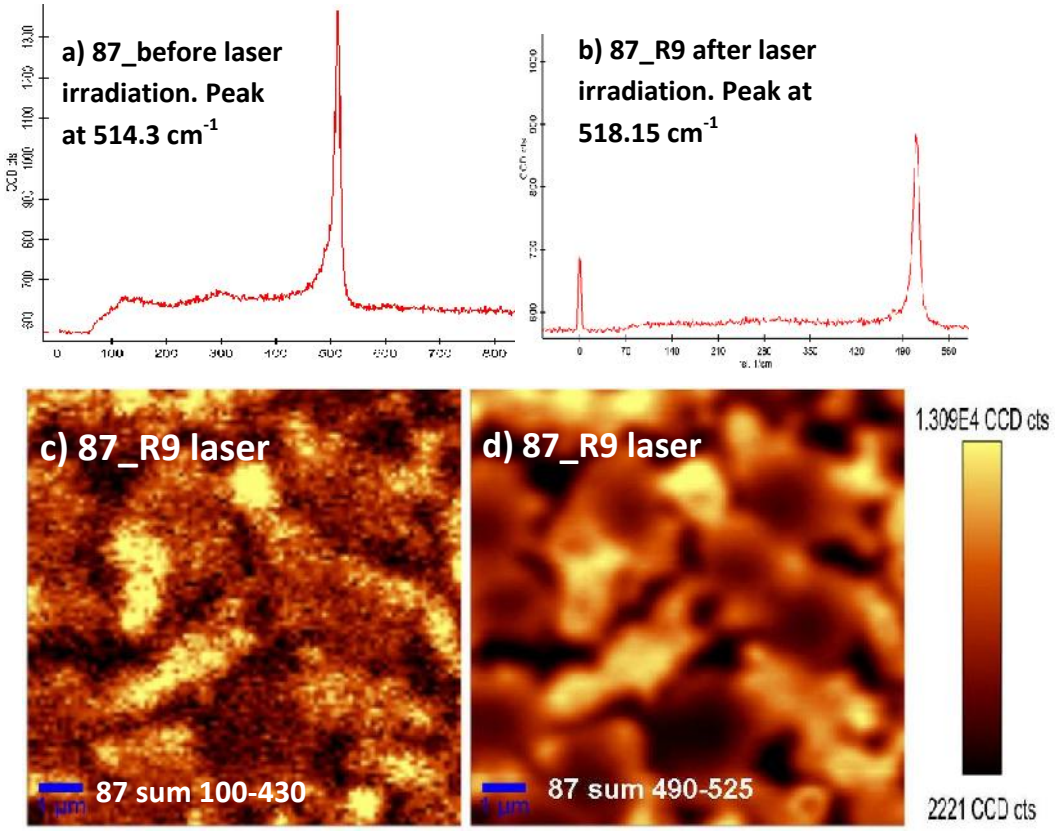

Figure 6.11: Confocal Raman spectrum at a single spot a) 87_nSi before laser irradiation b) 87_R9 after laser irradiation of 10.2 J/cm^2, c & d) 87_R9 Confocal Raman images of sum of intensity (counts) in the range 100-525 wave number of laser annealed n-type doped intrinsic poly silicon film grown in HWCVD on glass substrate.

The images from Figure 6.10 can be interpreted as follows: the brightest features are crystalline whereas the darkest features are amorphous region, which could be partly due to the exposed glass substrate in regions from where silicon has moved into islands. A

significant peak intensity increase observed in the crystalline region of laser irradiated n-type silicon thin film on glass in i) spin-on phosphorus dopant and ii) phosphorus ion implantation. However a non homogeneous annealing is observed. This may be due to non uniform melting and solidification of silicon film during laser annealing. From 3D optical image also, we observed laser irradiation caused the surface roughness of about 5 micron.

Evaluation of crystallinity and doping uniformity is performed from confocal Raman spectrum (Fig 6.11a). We observe i) sharp microcrystalline peak at wave number 514.3 cm^{-1} and ii) some amorphous content in the wave number range 100 to 400 cm^{-1} before laser irradiation. After the laser annealing (Fig 6.11b) significant change is seen in the spectrum. The n-type silicon film becomes better crystalline and the amorphous content is significantly reduced. Raman images taken over 10×10 μm^2 surface area to analyse the crystallinity and laser annealing uniformity of n-type silicon film on glass substrate are presented in Figure 6.11c&d. A large degree of spatial non-homogeneity is observed in the crystallinity of the laser irradiated film.

6.5.7 Photoluminescence (PL) study

PL spectra of doped and undoped silicon films have been measured to characterize the samples before and after each step of synthesis sequence. Here we have three such kinds of synthesis steps. First we have this intrinsic poly silicon film second we have spin-on phosphorus dopant (SOD) followed by laser annealing and third we have ion implanted on silicon film followed by laser irradiation. Room temperature PL spectra of all these three stages are presented in Figure 6.12. PL is excited by using laser operating at 532nm. Excess carriers are generated over the film thickness from glass side surface [17]. PL spectrum in Figure 6.12a shows the PL of intrinsic poly silicon film before laser irradiation. Figure 6.12b shows effect of phosphorus doping in laser irradiated spin-on-dopant. Fig 6.12c shows the PL of ion implanted silicon films after laser annealing. Using the Gaussian line fit for PL bands shown in Figure 6.12, we have calculated the full width half maxima and peak position, shown in table 6.5. The as grown film is very smooth and the spectrum shows typical interference peaks. The position of peak and half width are approximate in this case. The laser irradiated films are textured and no interference peak is seen in these spectra. PL spectra show that laser irradiation improved the material significantly and reduced defects in the n-type silicon film. Smaller full width at half maxima (FWHM) is observed after laser

irradiation. In particular, PL emission at energies below 1.0eV seen prominent in the as-grown film, which is symptomatic of gap states caused by defects, is absent in the laser annealed films. This indicates better crystallinity of the films after laser irradiation as also seen in the Raman spectra. The broad nature of the PL spectra extending to higher energy 1.3 to 1.43eV is expected from the doping concentration caused band filling.

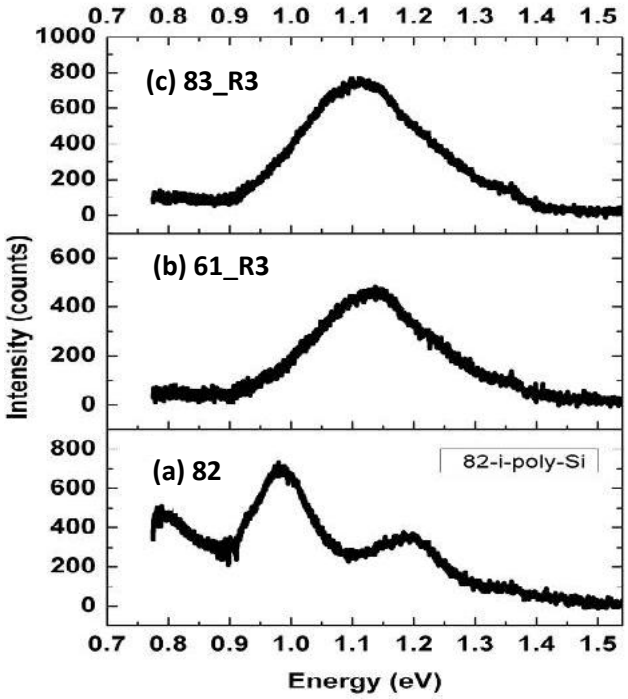

Figure 6.12 Photoluminescence (PL) spectrum a) 82_Glass intrinsic poly silicon film on glass b) 61_R3 laser annealed spin-on phosphorus dopant (SOD) silicon film on glass c) 83_R3 laser annealed phosphorus ion implanted silicon film on glass substrate.

Table 6.6: Numerical data from PL spectrum (Figure 6.12) of laser annealed n-type silicon film on glass substrate.

Parameters	Intrinsic poly Si film before laser irradiation (a_82)	Laser annealed SOD n-type silicon film (b_61)	Laser annealed ion implanted n-type silicon film (c_83)
Peak position	0.98 eV	1.13 eV	1.11 eV
FWHM	0.53 eV	0.22 eV	0.23 eV

PL spectrum shows that laser irradiation improved the material significantly also reduced defects in the n-type silicon film. Smaller full width half maxima (FWHM) observed after laser irradiation. In particular, PL emission at energies below 1.0eV seen prominent in the as-grown film, which is symptomatic of gap states caused by defects, is absent in the laser annealed films.

6.5.8 Optical transmission

Optical transmission spectra of as-grown and laser annealed n-type silicon film are shown in Figure 6.13. All transmission spectrums were taken in a range of wavelength from 350 nm to 1000 nm which covers ultraviolet-visible-near infrared (UV-VIS-NIR) region of electromagnetic spectrum. We have used integrating sphere to collect the transmitted light. The transmission spectrum of the un-annealed films shows interference fringes typical of smooth silicon films on glass caused by multiple reflections of light back and forth from the substrate which we have discussed in chapter 4, section 4.4.9.

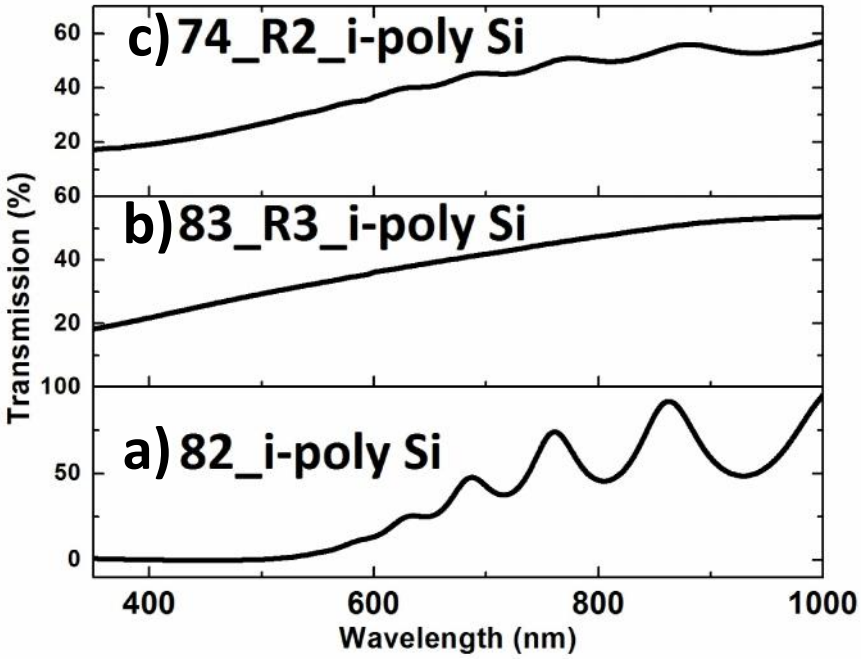

Figure 6.13: Optical transmission spectrums on glass substrates of a) 82_intrinsic poly silicon film b) 83_R3 laser annealed phosphorus ion implanted silicon film c) 74_R2 laser annealed spin-on phosphorus dopant silicon film.

Transmission spectra of laser irradiated film shows significant changes over the range of UV-VIS-NIR. Over the visible range transmission was steady around 50% on both laser irradiated spin-on dopant and ion implanted films shown in fig 6.13 c & b respectively. The interferences fringes observed in the spectrum of as-grown film have disappeared after laser irradiation, which makes the film rough and textured and eliminates the interference effects. Apart from this, we see high transmission at wavelengths less than 600 nm. This is a result of non- homogeneity of the films as seen from the morphology studies. Regions where there is no film on glass, continue to transmit light even at wavelengths where silicon has become opaque.

6.5.9 Resistivity analysis of Laser annealed silicon film

Laser parameters were varied to find condition for n-type silicon thin film so that phosphorus atoms get diffused (in case of spin-on dopant) and phosphorus ions get activated (in case of ion implantation). Resistivity values were obtained from sheet resistivity measurement using four probe instrument, are given in table 6.7. During the laser annealing, we have scanned sample surface using 10 micron diameter laser beam under focused condition, as described in the Table 6.2.

For spin-on phosphorus dopant silicon film, the optimized laser annealing condition is 9.5µs and scan speed 4cm/sec. The lowest resistivity obtained 0.4 ohm-cm.

For phosphorus ion implanted silicon film the optimized laser annealing condition 10.5µs and scan speed 4cm/sec. The lowest resistivity obtained 0.7 ohm-cm.

For n-type silicon film grown using HWCVD the optimized laser annealing condition 10µs and scan speed 3cm/sec. The lowest resistivity obtained 0.05 ohm-cm.

The resistivity measurements presented here are indicative since the films are not homogeneous. We observed that with an increase in the area of laser scanned film, using the same laser annealing condition, resistivity was not uniform in the different part of annealed area.

Table 6.7: Resistivity data of laser annealed n-type silicon thin film on glass for spin-on phosphorus dopant (SOD), phosphorus ion implanted (Ion) and n-type silicon film (n-Si) HWCVD.

Laser annealed Sample	Laser parameter		Voltage Volt (V)	Current Amp (I)	Sheet resistance =V/I*4.532 ohm/square	Resistivity Ohm-cm
	scan speed cm/s	Pulse duration μs				
78_R4_SOD	1	9	8×10^{-2}	4.53×10^{-8}	8×10^{6}	8×10^{2}
74_R1_SOD	2	9	3.28×10^{-1}	4.53×10^{-5}	3.28×10^{4}	3.25
66_R2_SOD	4	9	7.1×10^{-3}	4.53×10^{-6}	7.1×10^{3}	7.1×10^{-1}
74_R2_SOD	4	9.5	4×10^{-1}	4.53×10^{-4}	4×10^{3}	4×10^{-1}
84_R2_Ion	2	10.5	7×10^{-1}	1×10^{-6}	3.16×10^{6}	3.17×10^{2}
83_R3_Ion	4	11	2.1×10^{-2}	1×10^{-6}	9.52×10^{4}	9.5
84_R3_Ion	3	10.5	4×10^{-3}	1×10^{-6}	1.8×10^{4}	1.8
84_R1_Ion	4	10.5	1.6×10^{-3}	1×10^{-6}	7.25×10^{3}	7.25×10^{-1}
87_R1_nSi	3	10	7×10^{-4}	1×10^{-6}	3.17×10^{3}	5.7×10^{-2}
87_R9_nSi	3	10	2×10^{-3}	1×10^{-6}	9.06×10^{3}	1.6×10^{-1}

A large non-uniformity in resistivity varying from 0.1 Ohm-cm to 0.8 Ohm-cm observed in one film. Similar behaviour is seen in other sample also. There may be several reasons for this non uniformity. One major reason is that the laser annealed films are not uniform as seen in the optical, SEM and Raman imaging. The films become patchy and poorly connected. As a result, the measurements vary depending on the connectivity and contacts with the probes.

6.5.10 Resistivity analysis of thermally annealed silicon film

Resistivity analysis was performed to evaluate dopant annealing and activation of n-type silicon film on glass substrate. Thermally annealing was performed in the HWCVD reaction chamber. Under the growth condition that we have explained in section 6.4.2, lowest resistivity obtained using HWCVD annealing is 2.13 ohm-cm for ion implanted silicon film.

Table 6.8: Resistivity data of n-type silicon film annealed using atomic hydrogen in HWCVD chamber.

Sample	Voltage Volt (V)	Current Amp (I)	Sheet resistance =V/I*4.532 ohm/square	Thickness cm	Resistivity Ohm-cm
84_Glass/ Ion	4.7×10^{-1}	1×10^{-4}	2.1×10^{4}	1×10^{-4}	2.13
80_Glass/ Ion	1×10^{-2}	1×10^{-6}	4.53×10^{4}	1×10^{-4}	4.53
98_Glass/ nSi	1×10^{-3}	1×10^{-6}	4.53×10^{3}	1.8×10^{-5}	8.16×10^{-2}

For microcrystalline n-type silicon film grown at 350°C substrate temperature using HWCVD on glass substrate the resistivity was obtained 0.08 ohm-cm. This HWCVD grown film has initial resistivity of 0.57 ohm-cm before annealing. No non uniformity in resistivity was observed in HWCVD annealed film. Values obtained from the literature suggested that sheet resistance 4.7 Ω/□ was observed for annealing at 1000°C for 1h in conventional furnace [18] and 100 Ω/□ was observed for annealing at 900°C for 25s in lamp furnace [19].

6.5.11 Phosphorus concentration analysis using TOF-SIMS

Time of flight secondary ion mass spectrometer (TOF-SIMS) used to evaluate phosphorus concentration in n-type silicon film shown in Figure 6.14.

Calibration of TOF-SIMS was performed using reference sample as explained in section 5.4.7, chapter 5. The reference sample was prepared in a diffusion furnace using a solid phosphorus source at 890°C for 15 minutes on 2 inch diameter n-type silicon wafer. Phosphorus concentration versus depth profile of this reference sample was obtained using another secondary ion mass spectrograph (SIMS) apparatus [20] which was calibrated with a standard. The conversion factor for phosphorus detection is 1 count $=10^{17}$ atoms-cm^{-3} estimated from table 6.9. Distribution of phosphorus in this reference sample obtained by the SIMS measurement is shown Fig 6.14 a.

Table 6.9: Calibration of TOF-SIMS apparatus for detection of phosphorus using reference phosphorus sample's SIMS profile.

Depth in nm	Phosphorus reference sample		
	Using SIMS		Using TOF-SIMS
	Intensity (Counts/sec)	Concentration Atoms-cm^{-3}	Intensity (Counts/sec)
100	1.8×10^{3}	1.8×10^{20}	1.13×10^{3}
200	3×10^{2}	3×10^{19}	3.8×10^{2}
300	2×10^{2}	2×10^{19}	2.21×10^{2}
400	8×10^{1}	8×10^{18}	9.84×10^{1}
500	4×10^{1}	4×10^{18}	4.6×10^{1}

TOF-SIMS analysis shows that concentration of phosphorus at the very top surface was 5.8×10^{20} atom-cm^{-3} for n-type silicon film, 1.6×10^{21} atom-cm^{-3} for laser annealed n-type silicon film grown by HWCVD with phosphine. Our SIMS measurement system could measure phosphorus concentration reliably up to about 1×10^{18} atoms-cm^{-3}. This is a system limitation.

Time of flight secondary ion mass spectrometer (TOF-SIMS) used to evaluate phosphorus concentration in n-type silicon film shown in Figure 6.14.

Concentration of phosphorus was measured using caesium (Cs) ion source as a primary ion beam to sputter the top surface of thin silicon film. Depth profile of sputtered region was obtained by measuring total crater depth using surface stylus profiler. The calibration silicon sample was profiled upto depth of 1137 nm with sputtering rate 0.28 nm/sec as shown in Figure 6.14a; however the trace beyond about 700 nm does not have any meaning since because counts saturate because of background.

In Figure 6.14b phosphorus concentration profile of as-grown n-type silicon thin film on glass is presented as obtained from TOF-SIMS measurement. We continued the dynamic profiling up to 242 nm with sputtering rate 0.30 nm/sec for phosphorus doped silicon film shown in Figure 6.14b. For laser annealed n-type silicon film shown in Figure 6.14c, we profiled upto depth 348 nm at sputtering rate 0.3 nm/sec.

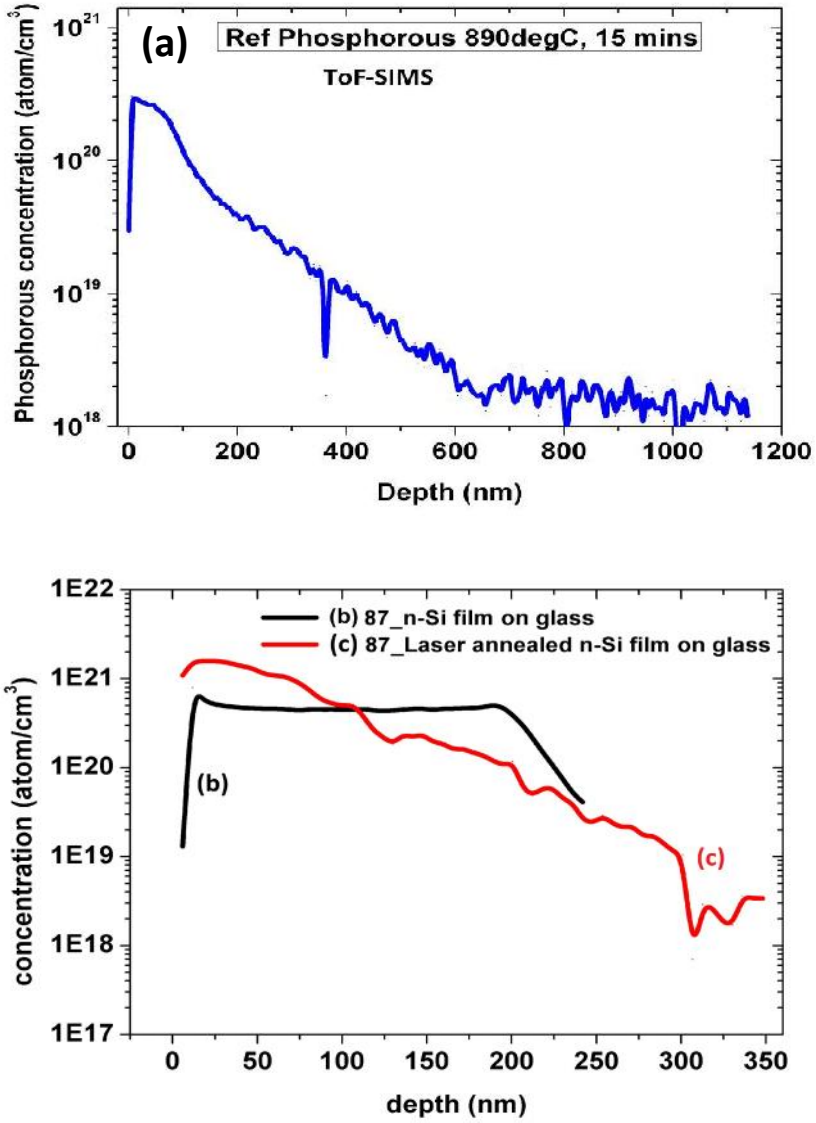

Figure 6.14: Concentration – depth curve of a) standard phosphorus doped n-type silicon sample prepared by furnace diffusion of phosphorus at 890°C for 15 minutes. b) 87_ phosphorus doped silicon film on glass, c) 87_R9 laser annealed phosphorus doped silicon film on glass.

From Figure 6.14b, it is seen that the concentration of phosphorus is uniform (about $5x10^{20}$ atoms/cm^3) over the thickness of the HWCVD synthesized thin silicon film. This measurement also gives estimate of the thickness of the film to be 180nm, which is in agreement with the thickness obtained from depth profiling using surface stylus profiler.

From Figure 6.14c, it is seen that after laser irradiation the phosphorus concentration is no longer uniform. It has increased to ~$1.5x10^{21}$ atoms/cm^3 near the surface

of the sample and decreased along the film thickness. This redistribution can be understood as follows. With laser irradiation, the silicon film melts and then starts to solidify from the position closest to the glass substrate. So the film at the top surface solidifies later. We know that phosphorus has a segregation coefficient of around 0.35 which leads to an increase in the phosphorus concentration at the top surface as the top portion solidifies first [21]. In the as-grown sample, phosphorus was uniform up to 180 nm from the top surface. However, in the laser annealed sample phosphorus was present up to 300nm. This is an estimate since the film becomes spatially non-uniform as a result of laser annealing

6.6 Discussion

We have investigated three routes for preparing phosphorus doped silicon films for photovoltaic application. Initially we tried spin-on dopant and ion implantation techniques to dope as-grown undoped silicon films. To avoid thermal treatment for dopant diffusion /activation and achieving n-type doped silicon thin film on glass, we tried using infrared laser induced annealing and dopant activation process. While phosphorus doped films could be obtained with acceptable dopant concentration, the films were highly non-uniform spatially. The doping and annealing occurred by melting of the surface region followed by liquid phase regrowth. As a result, laser irradiation increased surface roughness to several microns. Across the sample surface, silicon formed islands and there was bare glass in between which makes the film non-useable for device application. We worked with silicon films one micron thick. Increasing the thickness of silicon film to several microns or changing the shape of the optical beam to a line rather than a point may improve this aspect. Then some texturing of the film may be even useful and allow better utilization of sunlight by the silicon film for the photovoltaic application.

Another significant part of the above study is that the average grain size increased after laser irradiation as observed from Raman spectrum. Further, the sub-band gap defects density reduced as observed from the PL spectra. This would contribute to better lifetime of excess carriers and device worthiness of material if the film can be made spatially connected.

Finally, we tried to fabricate device from the n type silicon layer grown by HWCVD. This will be discussed in the next chapter.

6.7 References

[1] S. Oosterhoff, " Distributions of boron and phosphorus implanted in silicon" Nuclear Instruments and Methods in Physics Research, B30, 1-12 North-Holland, Amsterdam, 1988.

[2] K. Sera, F. Okumura, S. Kaneko, S. Itoh, K. Hotta, and H. Hoshino, "Excimer-laser doping into Si thin films,"J. Appl. Phys., vol. 67, pp. 2359– 2363, 1990.

[3] E. A. Al-Nuaimy, J. M. Marshall, and S. Muhl, "Properties of n+ and p+ polysilicon thin films fabricated by an excimer laser-activated spin-on dopant technique, "J. Non Crystalline Solids, vol. 227–230, pp. 949–953, 1998.

[4] S.-Y Lien, B.-R Wu, H.-Y Mao, J.-H Wang, I.-C Hsieh, P.-C Yao, and D.-S Wuu, "Simultaneous re-crystallization, phosphorus diffusion and antireflection coating of silicon films using laser treatment," Thin Solid Films, vol. 496, pp. 643–648, 2006.

[5] I. A. Palani, N. J. Vasa, M. Singaperumal, and T. Okada, "Investigation on production of highly textured Sb doped polycrystalline silicon using solid state Nd:YAG laser for photovoltaic application," Proc. SPIE, vol. 7584, pp. 758410-2–758410-8, 2010.

[6] http://www.semiwafer.com/products/sapphire.

[7] Billy L. Crowder, Ion Implantation in Semiconductors and Other Materials, 1973.

[8] Nicholas R. White, "Ion implantation for VLSI, VVLSI Electronics microstructure science volume 21, beam procession technology, 360-438, Academic press, Oriando, FL, 1989"

[9] Y. Tamura, T. Ohnishi, T. Shin'yama, T. Maeda, Y. Kibi, K. Takaoka, M. Naito, N. Hamamoto, Y.goino, S.Nishimura, "The nissin NH-50SR 500kV implanter using multiply charged ion". Ion implantation technology,Page 474, S. Coffa, G. Ferla, E. Rimini – Elsevier Science B.V, 1995.

[10] http://www.filmtronics.com/capabilities/products/diffusants

[11] http://www.spilasers.com/Products/redENERGY_G4.aspx

[12] http://www.scantechlaser.com/laser-welding-machine.html

[13] A. Chowdhury, A. Bahouka, S. Steffens, J. Schneider, J. Dore, F. Mermet, A. Slaoui, Laser annealing of thin film polycrystalline silicon solar cell, EPJ Photovoltaics 4, 45108, 2013. (doi: 10.1051/epjpv/2013019).

[14] Sergey Varlamov, Bonne Eggleston, Jonathon Dore, Daniel Ong, and Rhett Evans, 'Diode-laser processed crystalline silicon solar cells', SPIE, News room, 2013. (doi: 10.1117/2.1201303.004744).

[15] Kuninori Kitahara, Toshitomo Ishii, Junki Suzuki, Takuro Bessyo, and Naoki Watanabe, 'Characterization of Defects and Stress in Polycrystalline Silicon Thin Films on Glass Substrates by Raman Microscopy', International Journal of Spectroscopy, V-2011, Article ID 632139, p-14, 2011. (doi:10.1155/2011/632139).

[16] Shiyang T, Michael F. Morris, Steven J. Morris, Borna Obradovic, Geng Wang, Al F. Tasch and Charles M. Snell, a detailed physical model for ion implant induced damage in silicon, ieee transactions on electron devices, vol. 45, no. 6, June 1998.

[17] J. Dore, D. Ong, S. Varlamov, R. Egan, M. Green, Progress in laser crystallized thin-film polycrystalline silicon solar cells: Intermediate layers, light trapping, and metallization, IEEE Journal of Photovoltaics 4(1), p33-39, 2014. (doi:10.1109/JPHOTOV.2013.2280016).

[18] Tec. S. T. and D. G. S. Chuan, Diffusion profile of spin-on dopant in silicon substrate, Solar energy materials, Vol-19, p237-247, 1989. (doi:10.1016/0165-1633(89)90009-9).

[19] Mathiot, D., A. Lachiq, A. Slaoui, S. Noel, J. C. Muller, and C. Dubois, Phosphorus diffusion from a spin-on doped glass (SOD) source during rapid thermal annealing," Materials Science in Semiconductor Processing, Vol. 1, 231-236, 1998.

[20] Karthik mukhersen, M.Tec thesis, Indian institute of technology Bombay, India, 2014.

[21] L. Oberbeck, Neil J. Curson, T. Hallam, Michelle Y. Simmons, Robert G.Clark, Gerhard Bilger, Measurement of phosphorus segregation in silicon at the atomic-scale using STM, arXiv: cond-mat/0307495v1,10.1063/1.1784881, 2003.

Chapter 7

HIT structured n-i-p diode

7.1 Introduction

In this chapter we have reported the fabrication process of n-i-p hetero junction with intrinsic silicon thin layer (HIT) structure diode on fluorine tin oxide coated alkali free borosilicate glass substrate using hot wire chemical vapour deposition (HWCVD) technique. We have grown the complete device structure including i) n type microcrystalline silicon layer on FTO coated glass, ii) intrinsic polycrystalline silicon one micron thick layer, jjj) hydrogenated amorphous intrinsic silicon layer (a-Si:H) nearly 5 nm thick, and iv) p type a-Si:H layer at the top. We have measured the dark I-V and the illuminated I-V to observe photo response under visible light. Capacitance measurement was performed to evaluate depletion width, carrier concentration near the depletion region.

7.2 Device structure of n-i-p diode

7.2.1 Device structure

3D and 2D structural schematic diagram of n-i-p diodes fabricated is shown in figure 7.1.

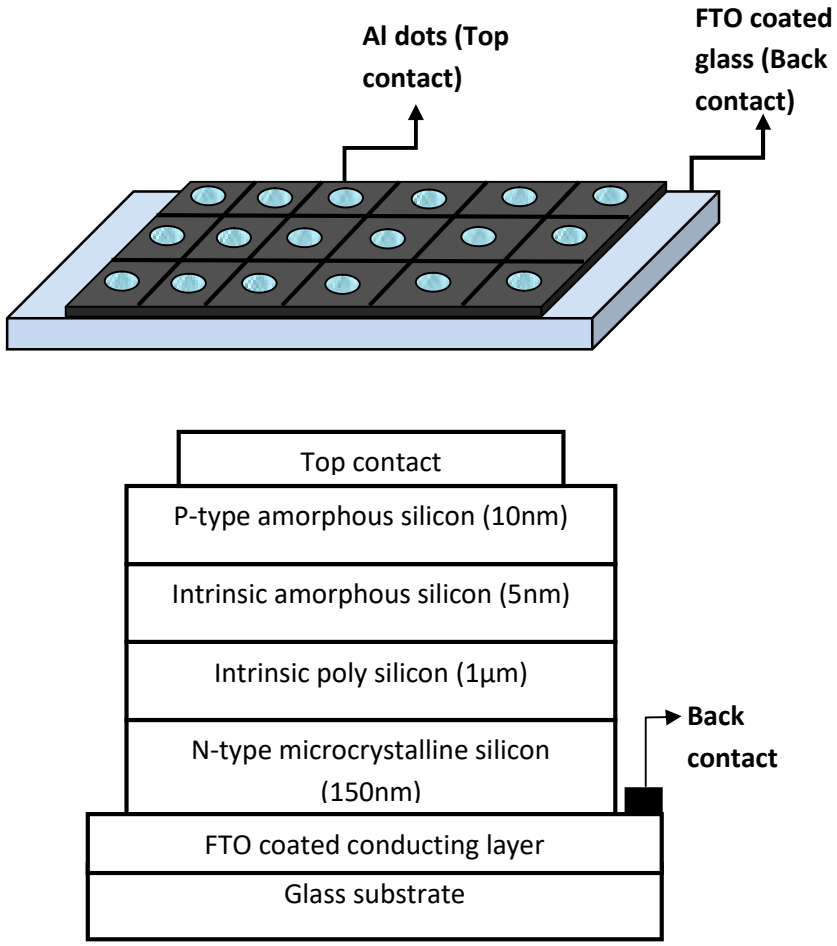

Figure 7.1: 3D and 2D block diagram of HIT structured n-i-p diode

7.2.2 Working principle of the device

In this section we have discussed the operation of n-i-p device along with the band diagram.

7.2.2.1 Schematic device diagram

Well known HIT structure solar cell which combines amorphous silicon and crystalline silicon [1] has been used as guide for our device structure. In our study, we replace the crystalline silicon substrate with intrinsic polycrystalline silicon layer as the base absorber. Highly doped n-type microcrystalline silicon is used as the back contact layer to the base.

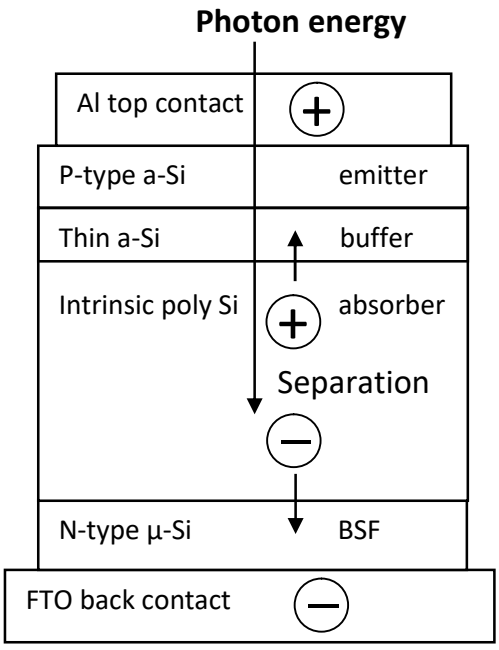

Figure 7.2: Schematic diagram of the operation of n-i-p diode fabricated using HWCVD on FTO coated glass substrate.

Thin (about 5 nm) intrinsic hydrogenated amorphous silicon film is grown on top of the intrinsic polycrystalline to form passivating hetero junction. The top emitter layer is p-type hydrogenated amorphous silicon film as shown in figure 7.1. This combination of thin amorphous silicon layers also acts as good surface passivators [2,3,4].

Absorption of high energy photon and resulting electron hole pair generation occurs in the absorber layer. Separation of electrons and holes occurs due to the internal electric field across the intrinsic absorber region, holes move towards p-type silicon layers and electron move towards n-type silicon layer. The strength of internal electric field depends on the doping concentration of the emitter layer. The higher doping concentration of emitter layer (amorphous p-type silicon film) also allows good ohmic contact with the external metal contact.

7.2.2.2 Schematic band diagram

A schematic of equilibrium band diagram of the device is shown in figure 7.3. The parameters used in drawing this diagram, are given in table 7.1.

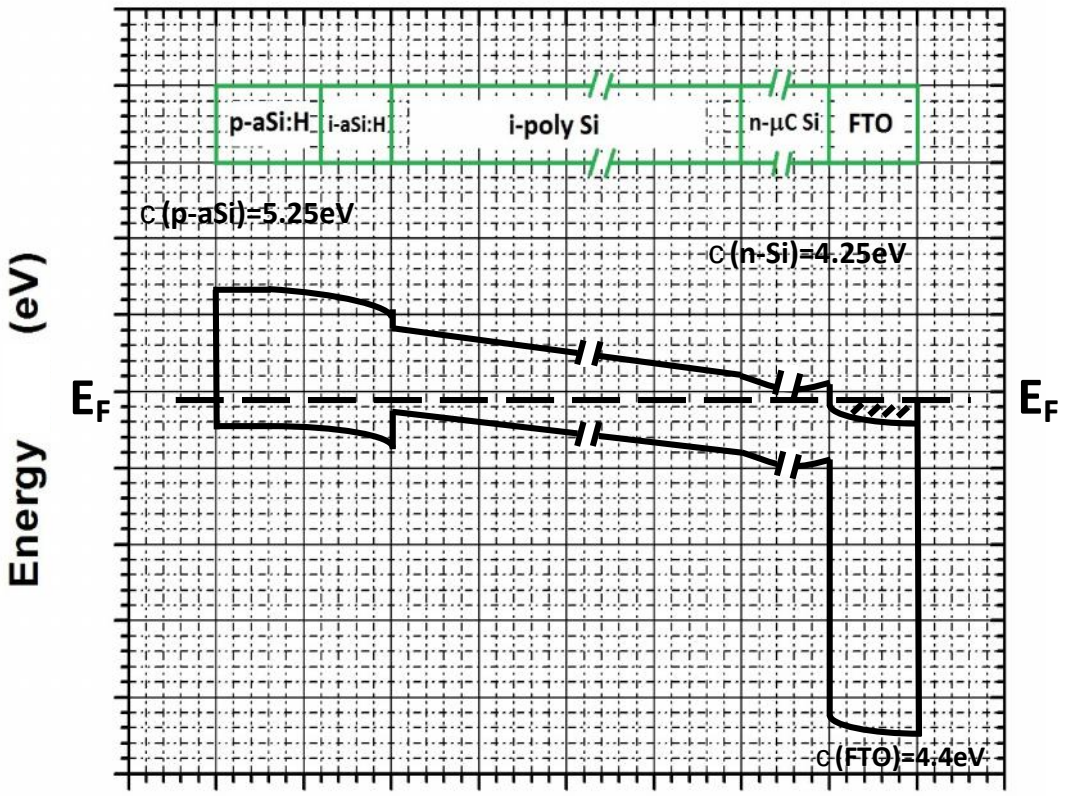

Figure 7.3: Schematic equilibrium band diagram of n-i-p diode fabricated using HWCVD on FTO coated glass substrate.

The a-Si:H has larger band gap than c-Si base, which causes discontinuities in conduction and valence bands at the heterojunction. Thus it acts as a window layer for light and passivates the emitter surface. There is larger band discontinuity in the valence band (0.35 eV) than in the conduction band (0.15 eV). A theoretical simulation indicated that a high discontinuity in the conduction band at the p/i interface prevents electron back diffusion from the absorber layer to the emitter layer and thus reducing loss of minority carriers at the p-type layer [5]. In this sense, the structure is not ideal.

Table 7.1: Parameters used for schematic band diagram [6].

Name	Work function	Reference
FTO	= 4.4 eV	[7]
n-Si:H	= 4.05 + 0.2 (Electron affinity of n-Si + (E_C - E_F) (n-Si)) = 4.25 eV	[8]
E_g (c-Si) ΔE_g (a-Si:H/c-Si) ΔE_C (a-Si:H/c-Si) ΔE_V (a-Si:H/c-Si)	= 1.1 eV = 0.6 eV = 0.15 eV = 0.45 eV	
p-a-Si:H	= E_g (a-Si)1.7eV – (E_F – E_V) = 1.7eV – 0.35eV= 1.35eV = Electron affinity of a-Si + (E_F - E_V) = 3.9 + 1.35 = 5.25 eV	
Aluminium	= 4.08 eV	[9]

7.2.2.3 Role of passivation and emitter layer

The primary function of a passivation layer in a hetero junction is to reduce the defect density at the interface with the absorber layer (which reduces the interface recombination) while admitting a maximum amount of light to the absorber layer [10]. Hydrogenated intrinsic amorphous layer has wider band gap (about 1.7 eV) and is known to passivate the surface of crystalline silicon [8]. Further, its thickness is about 5 nm, so that it allows light to pass without significant loss. We have grown 5 nm thick amorphous buffer layer using H_2:SiH_4=20:1 shown in section 4.3.5, chapter 4. This optimized H_2:SiH_4 ratio allows growing well passivated silicon film [11]. The p type a-Si:H provides the counter doped layer to form the p-i-n diode for photovoltaic action.

7.2.2.4 Role of absorber layer

We have grown one micron thick polycrystalline intrinsic silicon layer used as light absorbing material in our study. As a candidate for light absorbing material this layer has to be sufficiently textured. When the film is around 4-5 micron thick, the surface texture is suitable for light trapping. Film with thickness less than 1.5 micron does not allow necessary surface texturing for light trapping [12,13,14,15]. Optical reflection, transmission and absorption analysis was performed in the section 4.4.8,9,10, chapter 4. Reflectivity is found to be more or less 25% for the absorber layer (intrinsic poly silicon film). This can be further reduced by using a textured back surface field. Well passivated absorber layer also prevents recombination of charge carrier before reaching the contacts, improving the device performance.

7.2.3 Front and back contacts

For contact materials we have used fluorinated tin oxide (SnO_2:F) as back contact with n-type silicon and aluminium (Al) as front contact to p-type amorphous silicon. There are some conditions that the electrode material has to fulfil [16]. The metal contact should have higher optical transmission (85%) in the entire visible wavelength region where the photovoltaic absorber layers are active. Also to have a well conducting layer the metal contact should have low sheet resistance (10 ohm/square) to minimise series resistance losses with the p and n type layers. A rough surface can be used to increase the optical path of the light by scattering, while the morphology should avoid shunting paths, pinholes or local depletion.

In the case of an ohmic contact with top p-type silicon, the workfunction of metal needs to be larger or close to the sum of electron affinity and energy gap of p-type semiconductor. In the case of an ohmic contact with bottom FTO, the work function of FTO needs to be smaller or close to the sum of electron affinity and energy gap of n-type semiconductor. In this sense, it would be better to use metal such as gold which has work function about 5 eV [6,9] for the top contact. We have instead used Al which has work function of about 4.2 eV [9], which is not a good choice. This needs to be changed in future trials. We have considered the FTO work function 4.4 eV [7]. If our FTO layer has this work function, it will act as ohmic contact to the bottom n type Si layer. If however, the FTO work

function increases during the deposition of silicon layers when subjected to high temperatures, the quality of back contact may degrade. This needs to be checked in future trials.

7.3 Fabrication of n-i-p structure diode

7.3.1 Substrate Preparation

FTO coated alkali free borosilicate glass was used as substrate for n-i-p structured diode fabrication. The substrate was dipped in 2 % hydrofluoric acid (HF) for 5 sec for cleaning followed by nitrogen blow drying before loading in HWCVD reaction chamber. We have also used n-type silicon wafer oxidized to 500 nm silicon dioxide layer as a reference substrate.

7.3.2 Fabrication of n-type layer

Thin 150 nm of phosphorous doped microcrystalline silicon layer was deposited at 350°C substrate temperature with tantalum filament temperature 1650°C for 32 minutes. Base pressure was 1 $\times 10^{-6}$ mbar while process pressure was maintained at 6.6×10^{-2} mbar. The microcrystalline silicon films were grown at a gas flow ratio of SiH_4:H_2:PH_3= 2:50:1 sccm to achieve 150 nm thick film.

After this, the sample was transferred to another HWCVD deposition chamber for growing the rest of the structure. This transfer may affect the performance of the device though we have taken necessary precaution not to add any contamination during the transfer process. For making separate devices, a stainless steel mask was used for deposition of the 3 layers above the n type microcrystalline silicon layer. Hard stainless steel 3 mm $\times$ 3mm mask was used to separate all the devices with a 1 mm separation where in one run we can have 18 devices over a 1 cm $\times$ 2 cm substrate area.

7.3.3 Growth of intrinsic poly silicon film

Intrinsic poly crystalline silicon film was grown on top of 150 nm n-type silicon film. Thin 20 nm nucleation layers were grown at 400°C substrate temperature with filament temperature 1900°C along a gas ratio of SiH_4:H_2 = 1:20 for 100 sec. In order to grow thick silicon film, a mixture of SiH_4 and H_2 were used as process gas with a ratio of SiH_4:H_2=5:15 for 20 min [17]. The growth was performed in a ramp run where silane concentration increased gradually from 1 sccm to 5 sccm in four stages shown in table 7.2 steps 2 to 6. In stages 4 to 6, H_2 gas flow was reduced to keep process pressure constant. We have annealed the silicon film at this stage under 20 sccm of H_2 flow for 30 min followed by a H_2 soaking during cooling the sample from growth temperature to a lower temperature of 200°C for another 50 min.

7.3.4 Fabrication of passivating layer

A thin 5 nm layer of amorphous intrinsic poly silicon films were grown at this 200°C for 15 sec using a gas ratio of SiH_4:H_2=1:20. This layer acts as a passivating interface layer between the polycrystalline silicon and amorphous silicon emitter (with reference to chapter 4, section 4.3.5).

7.3.5 Fabrication of p-type layer

Amorphous p-type silicon film was grown on top of amorphous intrinsic thin silicon layer. Amorphous boron doped p-type 10 nm thin silicon layer was grown at 200°C substrate temperature with filament temperature 1900°C for 50 sec. The gas flow for this thickness were kept at a ratio of SiH_4 : H_2 : B_2H_6 = 1:20:2.2 sccm. Process pressure was kept in between 1.2×10^{-1} mbar to 1.3×10^{-1} mbar. Hard stainless steel 3 mm $\times$ 3mm mask was used to separate all the devices with a 1 mm separation where in one run we can have 18 devices over a 1 cm $\times$ 2 cm substrate area.

7.3.6 Process flow chart of the device

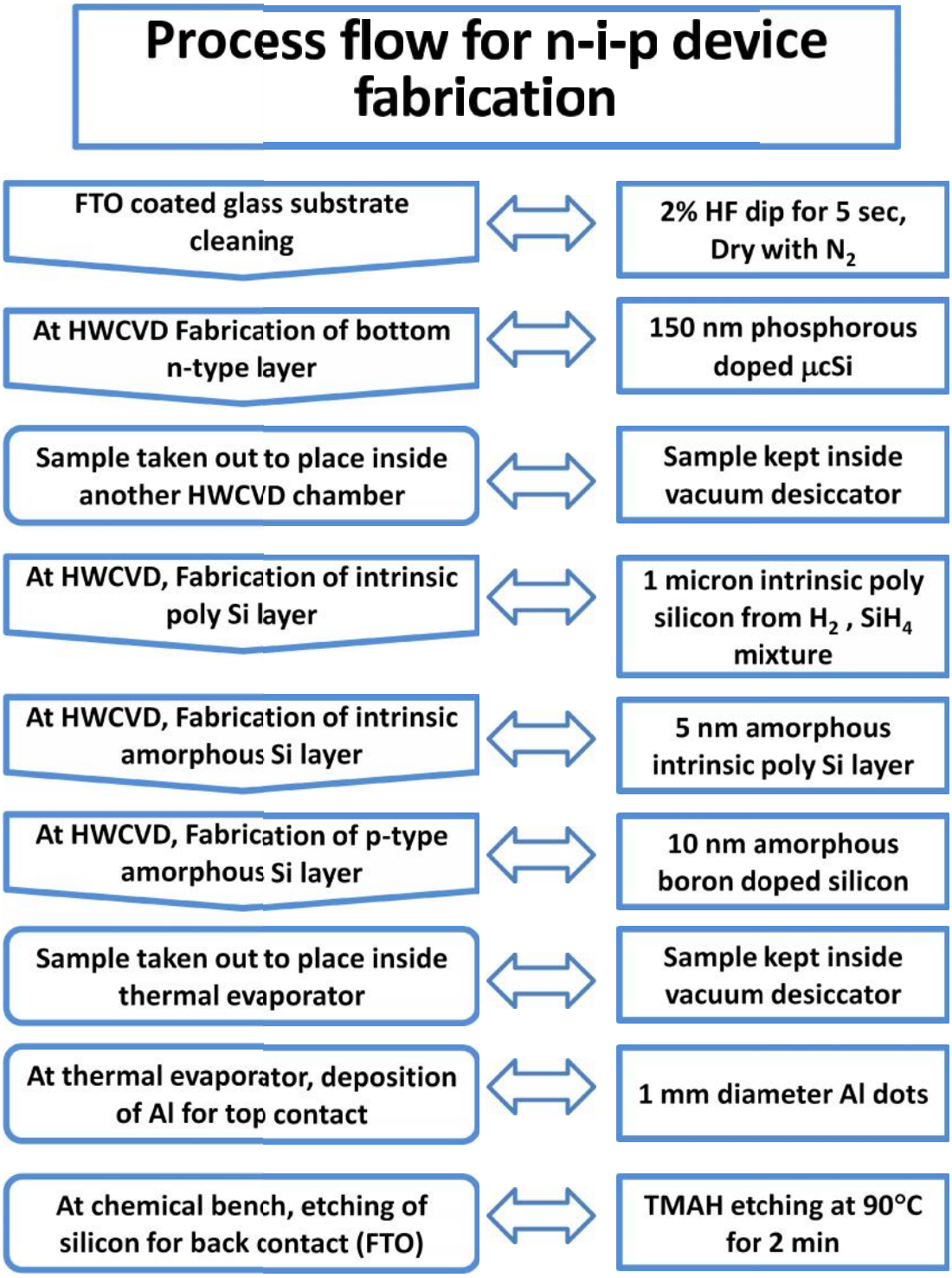

Figure 7.4: Process flow chart for n-i-p structure device fabrication.

7.3.7 Front and back contact

To form back contact, silicon needed to be removed so bottom fluorine tin oxide (FTO) is exposed. We have used chemical etching under fume hood to etch one micron of silicon from FTO coated glass. Details of chemical etching procedure are explained in Appendix II. Etching of silicon layer was confirmed by measuring the conductivity of FTO. For front contact we have used Aluminium (Al) thermal evaporator with a stainless steel mask containing 1 mm diameter circular exposed area which also aligned with the mask that used for the fabrication of the device. This way thin 100 nm Al film was deposited as top contact. We have used indium between tungsten probe and the Al film to avoid pin hole during I-V measurement as a safety precaution.

Table 7.2: Growth parameter of n-i-p hetero junction diode fabrication process using HWCVD on FTO coated glass substrate. (Sample 99_n-i-p_dev)

Step	Process gas pressure mbar	Substrate heater temp. °C	Filament temp. °C	Gas flow ratio sccm	Duration	Thickness nm	Growth Rate A°/Sec
1	6.6×10^{-2}	350	1650	SiH_4:PH_3:H_2=2:1:50	32 min	180	1
2	6.7×10^{-2}	400	1896	SiH_4:H_2=1:20	100 sec	20	2
3	7.3×10^{-2}	700	1886	SiH_4:H_2=1.5:20	100 sec		__
4	6.4×10^{-2}	700	1906	SiH_4:H_2=2:18	100 sec	214	7
5	6.7×10^{-2}	700	1908	SiH_4:H_2=3:17	100 sec		__
6	7.1×10^{-2}	700	1906	SiH_4:H_2=5:15	20 min	805	7
7	5.5×10^{-2}	600	1898	H_2=20	30 min	Passivation	__
8	5.6×10^{-2}	600 to 200	1892	H_2=20	50 min	Cooling	__
9	6.7×10^{-2}	200	1886	SiH_4:H_2=1:20	15 sec	5	2
10	1.2×10^{-2}	200	1868	SiH_4:B_2H_6:H_2=1:2.2:20	50 sec	10	2

7.4 Results

Results represented in this section are concerned with the electrical characterization of n-i-p diode. We have measured dark and one sun illuminated I-V curve for evaluating the photovoltaic performance of the device. We have also taken capacitance measurement under various bias voltages.

7.4.1 Study of dark and illuminated I-V

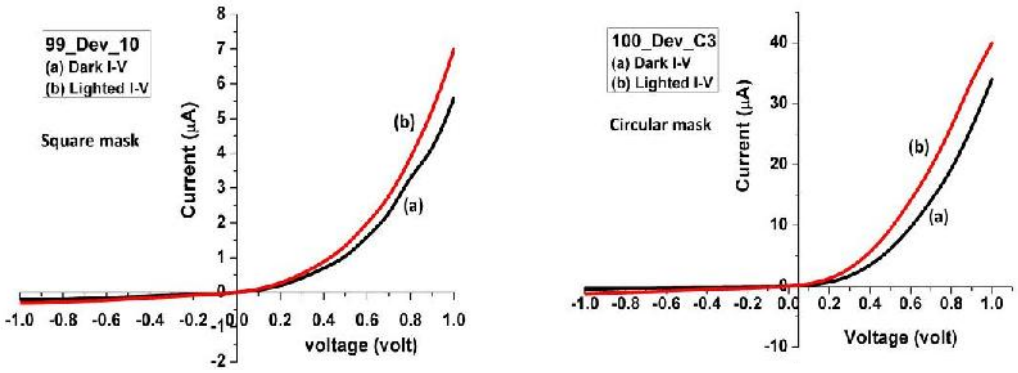

Figure 7.5: Dark and illuminated I-V curve of 99 n-i-p diode with square device 100 n-i-p diode with circular device

Dark (a) and illuminated (b) I-V curves for two devices are shown in Fig 7.5. Although diode like behaviour of the device is observed, the effect of shining light is rather small. In particular, the device does not develop any photovoltage. The effect of light is seen as only a small enhancement of current above the dark current like in a photoconductor. One possibility for the absence of photovoltage is that the region near the junction between the intrinsic silicon layer and a-Si:H / p-type a-Si:H layer is of poor quality and full of defects. This region, which is supposed to separate the photo-generated excess electrons and holes to develop the photovoltage, instead acts as a giant excess carrier killer by recombination such that no separation of electrons and holes occurs. The small enhancement of current under light is likely due to reduction in the resistance of the intrinsic silicon film.

From the dark forward bias I-V, the series resistance is as estimated about 1×10^5 ohm. The small reduction of this dark resistance, as seen from the enhancement of current in lighted I-V, suggests need to further improve the quality of the intrinsic silicon film in the device structure .

The leakage current in both devices are not that significant but on illumination of one sun, photo response is very small. This is related to the intrinsic polycrystalline silicon (light absorber) layer which is only one micron thick. Increase in the thickness of absorber layer will improve the photo response under illumination of visible light. Another possible reason is the top portions of the devices are covered by the Al (work function 4.08 eV) dots, (In our case the devices are 9mm^2, where the areas covered by the Al dots are 0.8 mm^2) perhaps we should have used gold with higher work function (5.1 eV) to reduce the contact resistance.

7.4.2 Study of capacitance

We have measured capacitance for various bias voltage using Agilent 4284A (20Hz to 2MHz) precision LRC meter.

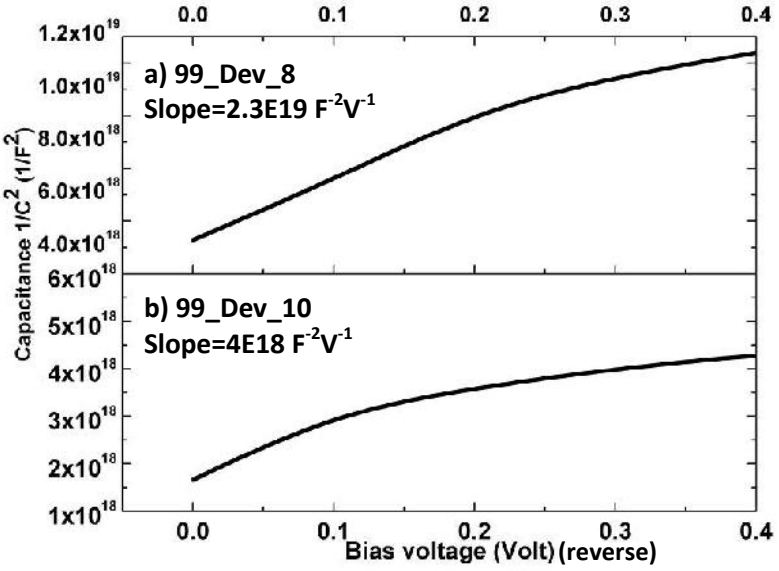

Figure 7.6: Capacitance ($1/C^2$) versus bias voltage curve of n-i-p structure diode.

The C-V measurement is performed with the fact that the width of space charge region under reverse bias of a semiconductor junction depends on applied voltage. The capacitance is determined by superimposing a small ac voltage of frequency 555 Hz on the dc bias voltage.

Table 7.3: Estimation of depletion width and majority carrier concentration from capacitance measurement for n-i-p structure diode.

Sample name	Capacitance at zero bias (F)	Device area (cm^2)	Depletion width (nm)	Slope of $1/C^2$ –V curve (F^{-2}-V^{-1})	Majority carrier concentration (atom-cm^{-3})
99_Dev_8	435×10^{-12}	0.09	847	2.3×10^{19}	2×10^{13}
99_Dev_10	776×10^{-12}	0.09	1200	4×10^{18}	3×10^{14}

We have calculated majority carrier concentration at depletion region, depletion width and capacitance at zero bias are shown in table 7.3. Details of the calculations are given in chapter 3. The n-i-p devices are having larger depletion region which causes the lower majority carrier concentration in this region.

7.5 Discussion

The feasibility of fabrication of n-i-p structured hetero junction with intrinsic thin layer diode on glass using HWCVD is performed. The n-i-p structured hetero junction with intrinsic thin layer silicon diode performances were evaluated from dark and illuminated I-V measurement. Illuminated I-V curve has not been shown much response to light this is because of the light absorber layer is only one micron thick. An initiative was taken to increase the thickness by increasing the growth duration. But this time the film got lifted due to high tensile stress. An increase in hydrogen dilution would have reduced the tensile stress. In that case increased growth pressure in the reaction chamber may have to be taken care off.

7.6 Reference

[1] Sawada T, Terada N, Sadaji T, Baba T, Takahama T, Kenichiro W, Shinya T, Shoichi N. High-efficiency a-Si/c-Si heterojunction solar cell. 1st World Conference on Photovoltaic Energy Conversion. (Hawaii), p1219-1226, Dec 5-9, 1994.

[2] Jensen N, Rau U,Hausner R M, Uppal S, Oberbeck L, Bergmann R B, J. H. WernerJ H, Recombination mechanisms in amorphous silicon/crystalline silicon heterojunction solar cells. J. Appl. Phys. 87: p2639-2645, 2000.

[3] Taguchi M, Kawamoto K, Tsuge S, Baba T, Sakata H, Morizane M, Uchihashi K, Nakamura N, Kiyama S, Oota O, HIT cells high-efficiency crystalline Si cells with novel structure. Prog. Photovoltaics. 8: p503-513, 2000.

[4] N. Jensen, R. M. Hausner, R. B. Bergmann, J. H. Werner, and U. Rau, Optimization and characterization of Amorphous/crystalline silicon heterojunction solar cells. Prog. Photovoltaics. 10: p1-13, 2002.

[5] Cleef M. W. M. van, Rath J K, Rubinelli F A, Werf C H M v d, Schropp R E I, Weg W. Performance of heterojunction p+ microcrystalline silicon n crystalline silicon solar cells. J. Appl. Phys. 82: p6089-6095, 1997.

[6] J. C. Riviere, A review of work function values and measurements by an expert, J. Solid State Surf. Sci. 1, 179, 1969.

[7] M. G. Helander, M. T . Greiner, Z. B. Wang, and W. M. Tang, 'Work function of fluorine doped tin oxide', J. Vac. Sci. Technology. (A), Vol. 29, No. 1, Jan/Feb, 2011.

[8] K. Jakobi, G. Chiarotti (ed.), Work function data 'Electronic and Vibrational Properties', Springer Materials, 1994. (doi. 10.1007/10086058_16).

[9] Skriver, H. L., & Rosengaard, N. M. Surface energy and work function of elemental metals. Physical Review B Condensed Matter, 46(11), p7157-7168. 0.1103/PhysRevB.46.7157, 1992.

[10] McCandless B.E., Hegedus S.S., Proc. of the 22thIEEE Photovoltaic Specialists Conference, p967–972, 1991.

[11] Kim S-K, Lee J C, Park S-J, Kim Y-J, Yoon K H., Effect of hydrogen dilution on intrinsic a-Si:H layer between emitter and Si wafer in silicon heterojunction solar cell. Solar Energy Materials & Solar Cells. 92: p298–301, 2008.

[12] K. Yamamoto, A. Nakajima, T. Suzuki, M. Yoshimi, H. Nishio and M. Izumina: Jpn. J. Appl. Phys. 33, L1751, 1994.

[13] K. Yamamoto, M. Yoshimi, T. Suzuki, Y. Tawada,Y. Okamoto and A. Nakajima: Proc. 2ndWorld Conf. Photovoltaic Solar Energy Conversion, Vienna, p. 1284, 1998.

[14] K. Yamamoto, M. Yoshimi, T. Suzuki, Y. Tawada, Y. Okamoto and A. Nakajima: Appl. Phys.A 69, 179, 1999.

[15] K. Yamamoto, M. Yoshimi, T. Suzuki, Y. Tawada, Y. Okamoto and A. Nakajima: IEEE Trans. Electron Devices 46, 2041, 1999.

[16] Schropp R.E.I., Zeman M., "Amorphous and microcrystalline silicon solar cells", Kluwer Academic Publishers, Boston, 1998.

[17] Gurleen Kaur, M.A. Hossion, Kulasekaran M, B.M. Arora, Synthesis of oriented and passivated polycrystalline silicon films on glass by hot wire chemical vapour deposition, 40th Photovoltaic Specialists Conference, Denver, Colorado, USA. ieee digital library (online) article Details, 6925153, 2014.

Chapter 8

Conclusions and Future Work

8.1 Conclusion

We have demonstrated the viability of growing oriented polycrystalline intrinsic silicon film on several low cost substrates like glass, nickel, TiO_2, sapphire and Si/SiO_2 maintaining a low growth temperature. For application as absorber layer in photovoltaic device, it was envisaged that the film should be polycrystalline with grains as large as possible even if the substrate is amorphous such as glass or Si/SiO_2. Further oriented growth was considered desirable for minimizing grain boundary defects. In order to achieve these objectives, we divided the growth process into three steps. In the first growth step, nucleation of silicon was done at 400°C using dilute mixture of Silane (SiH_4) and hydrogen (H_2). These nuclei had orientation such that they promoted <220> oriented silicon growth on all substrates including glass and Si/SiO_2. An increase in grain size of silicon observed while decreasing the nucleation density (discussed in chapter 4, section 4.4.2) on all five substrates (borosilicate glass, nickel strip, TiO_2 on glass, sapphire and Si/SiO_2) under controlled process pressure of 6.8×10^{-2} mbar with 1 sccm silane in 20 sccm hydrogen. Experimental study with atomic force microscope shows that nucleation density decreases with higher hydrogen dilution (1 sccm silane in 99 sccm hydrogen).

The second step involves the growth of silicon film at 600°C substrate temperature to achieve one micron thick undoped polycrystalline silicon as light absorbing layer for photovoltaic application. In the third step, the grown film is soaked in atomic hydrogen in-situ so as to reduce the number of broken and dangling bonds. This helps to reduce the defects related recombination as well as to improve electrical conductivity.

Resistivity of the as grown undoped silicon films was in the range of 2×10^5 ohm-cm to 2×10^6 ohm-cm with activation energy in the range 0.41 eV to 0.55 eV. As a result of the passivation treatment, we observed photoluminescence as well as photoconductivity response from the undoped silicon films. However, still further improvement is necessary as the PL spectrum showed defects related luminescence emission extending much below the band gap energy (discussed in chapter 4, section 4.4.11).

From XRD measurements, the silicon films are seen to be preferentially <220> oriented. Transmission electron microscope based cross section image shows a complex structure. The growth following the initial nucleation shows structure which is indicative of mixed twinned epitaxial silicon film in the thickness range 20 nm to 200 nm. Beyond this thickness, the growth is oriented columnar polycrystalline, similar to the observation from XRD. This changeover from nearly epitaxial to polycrystalline structure needs more detailed study.

HWCVD growth of polycrystalline and amorphous boron doped p-type silicon film was performed on several substrates as those used for the undoped silicon films. We have maintained a substrate temperature of 600°C for the growth of polycrystalline and 200°C for amorphous silicon film. Highly conducting, uniform thin boron doped amorphous silicon film was grown on glass substrate in order to use as emitter layer in a photovoltaic device.

We have reported two exploratory experiments to convert undoped silicon films to n-type films. The undoped silicon films deposited on glass were used for these experiments. Both the experiments used continuous wave infrared laser for activating the dopant. In the first experiment, a spin-on phosphorus dopant layer was deposited on the undoped silicon layer. The dopant was driven into the film by point focussed laser irradiation scanning the film surface. In the second experiment, the undoped silicon film was subjected to 100keV phosphorus ion implantation. Again the film was laser annealed for activating the dopant. In both the experiments, we were able to establish the synthesis of doped n-type silicon films as seen from lower resistivity and from phosphorus depth profiling from TOF-SIMS measurement.

However, the morphological structure of films had regions of discontinuity. It is possible that the laser irradiation caused melting of silicon film followed by solidification resulting the observed morphology. There was also loss of the <220> orientation observed in the as-prepared films.

There were extensive trials of control of the laser dose to improve the film morphology. However, better control over the laser beam shape is required for device quality films.

Finally, we prepared n-type conducting polycrystalline silicon films on glass by using another HWCVD system equipped with silane and phosphine, which were used in the device experiment.

An initiative was taken to stack three silicon layers in one structure in the form of an n-i-p diode for photovoltaic application. Here we have followed the well known hetero junction with intrinsic thin layer (HIT) structure. The structure was grown using two different HWCVD systems. Initially n-type silicon film was deposited on ITO coated glass. This was followed by deposition of undoped polycrystalline silicon film and p-type doped amorphous film. The electrical characterization of this n-i-p diode structure was performed under dark and illuminated conditions. Although a diode like I-V characteristics was obtained, the device showed very little photo response. We spent fairly large effort in the synthesis of individual layers used in the device. However, for fabricating the device, we spent only a little effort. It is clear that much more effort is necessary to optimise the steps in the device fabrication. This could involve further improvement in the quality of the layers (preferably depositing all the layers in a single HWCVD system or improved handling in the transfer from one HWCVD system to the other), thicker absorbing base layer, as well better control over deposited thicknesses and junctions between the layers.

8.2 Contribution of this thesis

We have established a three stage process of synthesis of (220) oriented poly-Si films at substrate temperatures below 600°C using HWCVD, facilitating the use of low cost substrates such as glass. The three stages of growth are i) nucleation, ii) thin epitaxial growth and iii) oriented columnar thick growth. Since the rate of growth of silicon film as well as the crystalline fraction of HWCVD films vary with chamber pressure and filament temperature, conditions for depositing poly silicon films of one to two microns thickness have been optimized. In most of our work, one micron thick films were synthesised. We introduced a passivation step in the HWCVD growth of undoped silicon films to reduce the defects. The films were soaked in atomic hydrogen and covered with thin layer of undoped a-Si:H which made them photo-conducting, a basic requirement for photosensitive devices.

Therefore, HWCVD synthesized silicon has the potential of providing base material for low cost photovoltaic cells on low cost glass. We have shown growth of similar material on a variety of substrates such as TiO_2 on glass, Nickel, sapphire and Si/SiO_2. Films grown on sapphire and Si/SiO_2 could be useful for field effect transistor devices.

For devices we need n-type and p-type silicon layers in combination with the undoped silicon layer. We have presented the conditions for growing by HWCVD p-type polycrystalline as well as a-Si:H layers by adding diborane along with the precursors SiH_4 and H_2. For synthesis of n-type silicon film, we have made exploratory investigations of converting undoped poly silicon films deposited on glass to n-type doped silicon films by using i) phosphorus containing spin-on dopant and by ii) phosphorus ion implantation.

In both cases, low temperature process laser annealing was used: i) to drive the dopant into silicon in the spin-on dopant case and ii) for defect annealing and dopant activation in the ion-implantation case. Formation of large grain low resistivity n- type silicon islands were observed. As such these films were not device quality, the work gives insight into the interaction between laser irradiation and silicon thin film. Apart from the materials synthesis and materials characterization studies, we have done initial experiments with the synthesis of a p-i-n structure based on the investigations. This structure uses HWCVD for the deposition of microcrystalline n-type silicon film on FTO coated glass with 98% hydrogen dilution, followed by growth of undoped polycrystalline silicon and the top layer is combination of undoped a-Si:H and p-type a-Si:H.

8.3 Challenges during the work

We have faced many challenges during the several phases of our research work. Some of them are discussed here.

It was decided that we should work at temperatures below 600°C and try to work out a synthesis technique for growing defect free large grain silicon films. We chose several substrates based on literature survey and accessibility. Silicon on sapphire had been used earlier for silicon films for transistors. Nickel foil was oriented substrate. Of course glass has been visualized as cheap substrate. TiO_2 as selective contact is currently popular and was also known to be oriented as we obtained from Washington Univ. St. Louis, Missouri, USA.

Some practical difficulties were: It was really difficult to cut sapphire and nickel into small pieces. Shape of sapphire substrate was never uniform and nickel strip have a bending at the edge due to the manual blade cutter.

After many trials and investigations, we did not find much improvement in the grain size or orientation in the silicon films grown on other substrate; hence we have selected glass for device growth. Choice of Si/SiO_2 as substrate was a replacement of glass for X-TEM because of cleavage property and for FTIR measurements since glass does not transmit beyond 2.5 microns. In the HWCVD apparatus, there were two chambers, one for growing p-type silicon and the other for growing undoped silicon. It turned out that there was some small leak in the chamber meant for undoped film growth which degraded the undoped film quality. Trials in reducing the leak were partly successful. So, for most of the experiments we have grown undoped silicon in the chamber meant for growing p-type films. As a result, cleaning the chamber was necessary before growth of undoped silicon to avoid unwanted boron doping. The filament of HWCVD was changed before every process run. For that we have to open the chamber followed by cleaning, heating, flashing and dummy run before process. This way to prepare the HWCVD for a process run, it took almost a week.

In addition to these, there is no provision of monitoring the substrate surface temperature in the growth chamber. We carried out calibration of substrate surface temperature under different conditions of filament temperature and substrate heater. Even so, some departure during thin film growth cannot be ruled out.

The biggest challenge was synthesizing n-type doped silicon film. There was no provision for introducing phosphine in our HWCVD apparatus. So, we tried to use undoped silicon film and convert it to n-type as described. The greatest challenge came from annealing. Thermal annealing required temperature greater than 600°C, not desirable for glass substrate. So we tried laser annealing. But found the dissymmetry of irradiation is very uncertain because of the uncertainty of focus. During laser annealing it was difficult to locate the focusing distance of the laser spot as the laser tool was not equipped with a beam profiler. In this case we had to locate the focusing condition allowing the laser to scan on a small part of the silicon film as dummy process run. With practically no other monitoring of the beam, too loose focus did not provide sufficient annealing and tight focussing caused thin silicon to melt and solidify into island, again undesirable.

We would like to mention another difficulty we faced in the optical measurements and their analysis. Optical measurements were always difficult for smaller substrates using the standard instrument. In most cases we had to reduce the beam diameter of light source for the reflection and transmission spectral measurements. That is not difficult by itself. The difficulty arises in matching the intensity of beams on the reference side and the sample side for both reflectance and transmission measurements. These spectra invariably have interference fringes. By using T/(1-R) obtained from the T and R spectra , it is possible to minimize the interference effect. However cancellation of the interference suffers if there are errors in the absolute magnitudes of T and R determined from experiment, introducing errors in the subsequent analysis. Thus special care is necessary in determining the absolute values of T and R.

8.4 Future work

The successful incorporation of the layers described in this work into an efficient photovoltaic device is, of course, the ultimate goal. The best possible approach would be in future to have a HWCVD cluster tool designed for the fabrication of n-i-p diode without breaking the vacuum. This should help in improving the quality of each layer as well as interfaces between different layers which seem to be of poor quality in our experimental structure. In case a single system for growing the whole device structure is not possible as happened in our case, better methods of handling and transferring samples from one system to another without exposure to atmosphere, by using portable desiccated and sealable chamber, need to be ensured before proceeding for the device work.

First indication of improvement of device will be in its dark I-V characteristics having i) low leakage current and ii) some forward I-V region of diode ideality factor $1<n<2$. Secondly, the device should also have a measurable open circuit photovoltage and short circuit current under light irradiation. We will need to know the thickness of each layer. This may be done by growing the layers on Si/SiO_2 substrate, which can be cleaved and a cross sectional TEM image will give the thickness values, and would require optimization. We will also need to check the conductivity of each layer. We could try and use combination of free carrier absorption and in-plane dc conduction measurements for this purpose.

Further improvement may require increase in the thickness of undoped silicon film from one micron to several microns to increase the light absorption. For this, we have to focus on the growth step thickening of layers. On one hand, thick film has to be grown at a reasonable growth rate. At the same time, film should not be excessively stressed which will cause it to lift from the substrate. Film quality should also be sufficiently good for carrier collection. For this quantum efficiency measurements will be of use. After improvement in the electrical characteristics, loss of light will have to be minimized. This will require anti-reflection coating, and possibly texturization of the substrate. The anti-reflection coating should also serve as efficient current collector.

Regarding the laser irradiation based annealing of films, apart from the control on beam energy, it will be useful to have better control on the focus and have capability to control the shape of the beam, so as to avoid melting of silicon while providing effective diffusion / defect annealing.

Before closing, there is one result of our work which could be of wider significance. While investigating the structure of the silicon film grown on Si/SiO_2 by using X-TEM (Figure 4.4, Chapter 4), we found a region of the grown silicon film (close to the substrate) which was epitaxial or nearly so. This was unexpected since growth is done on SiO_2 which is amorphous. This must have resulted from the initial nuclei getting connected by lateral growth when the substrate temperature was ramped up to 600°C, while the growth rate was still low and was being ramped up. Being a thin region, this part was not observable in the XRD measurements, which showed (220) oriented polycrystalline silicon film. Indeed X-TEM result did show the thick oriented polycrystalline columnar growth as well, seen as (220) oriented polycrystalline film in the XRD measurements. Our above finding came at a very late stage of work, but it will be interesting to explore the conditions responsible for growing epitaxial silicon film on glass more carefully. Furthermore, properties of this material need to be investigated in greater detail and could find application in another device such as field effect transistor.

Appendix I Fabrication tool

A. HWCVD system for polycrystalline silicon film

The three chamber hot wire chemical vapour deposition cluster instrument was design and developed in the centre of excellence in nano technology, Indian Institute of Technology Bombay, Mumbai, India [1,2].

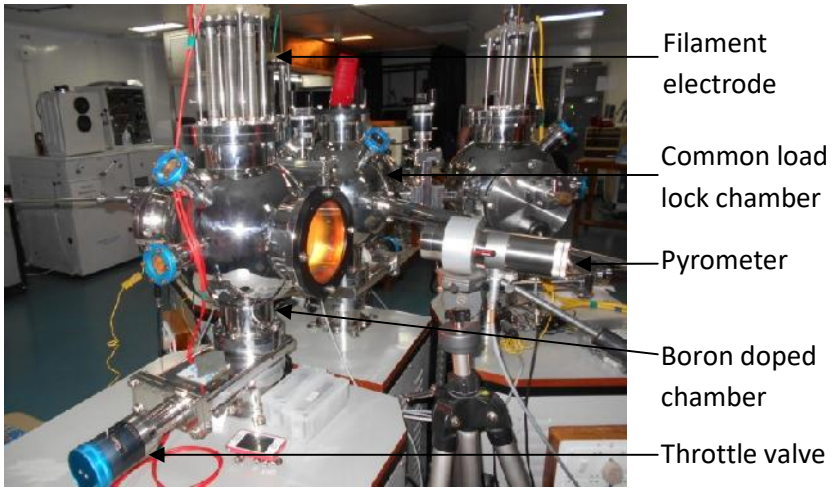

Figure Apparatus 1: Image of HWCVD cluster instrument for the growth of polycrystalline and amorphous silicon film.

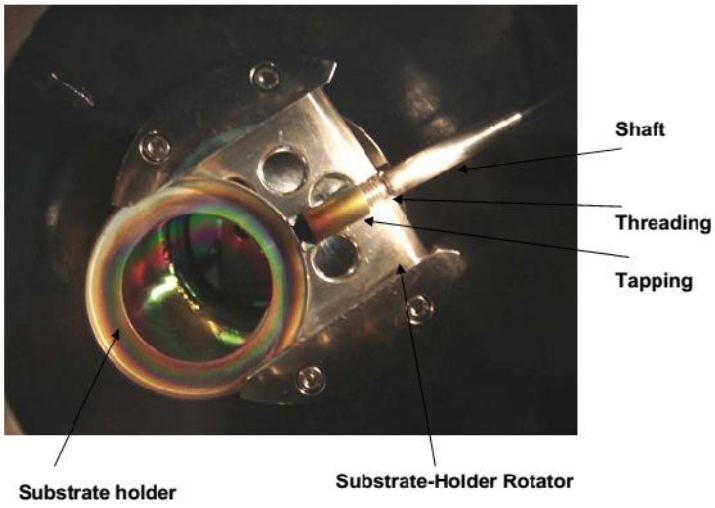

Figure Apparatus 2: Image of substrate holder assembly inside the load lock chamber of HWCVD cluster instrument [2].

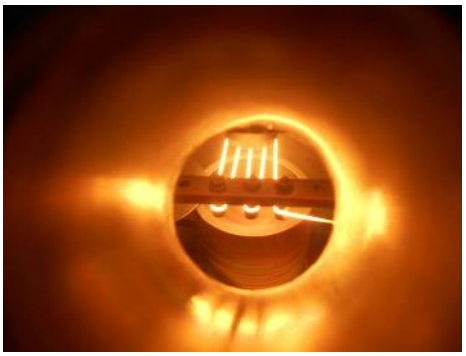

Figure App 3: Image of tungsten filament arrangement in HWCVD reaction chamber

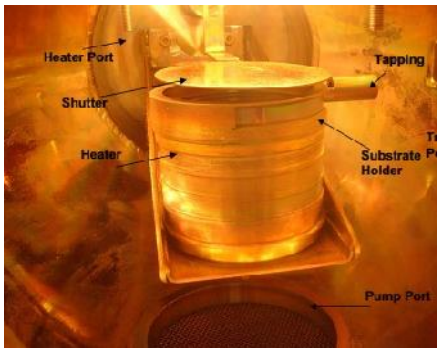

Figure App 4: Image of substrate heater, substrate holder and translatable shutter inside the HWCVD reaction chamber [2].

B. HWCVD system for microcrystalline silicon film

The four chamber hot wire chemical vapour deposition cluster instrument was design and developed by Advanced Process Technology and Pro-Vak established in the semiconductor processing lab, Metallurgical Engineering & Materials Science, Indian Institute of Technology Bombay, Mumbai, India [3,4].

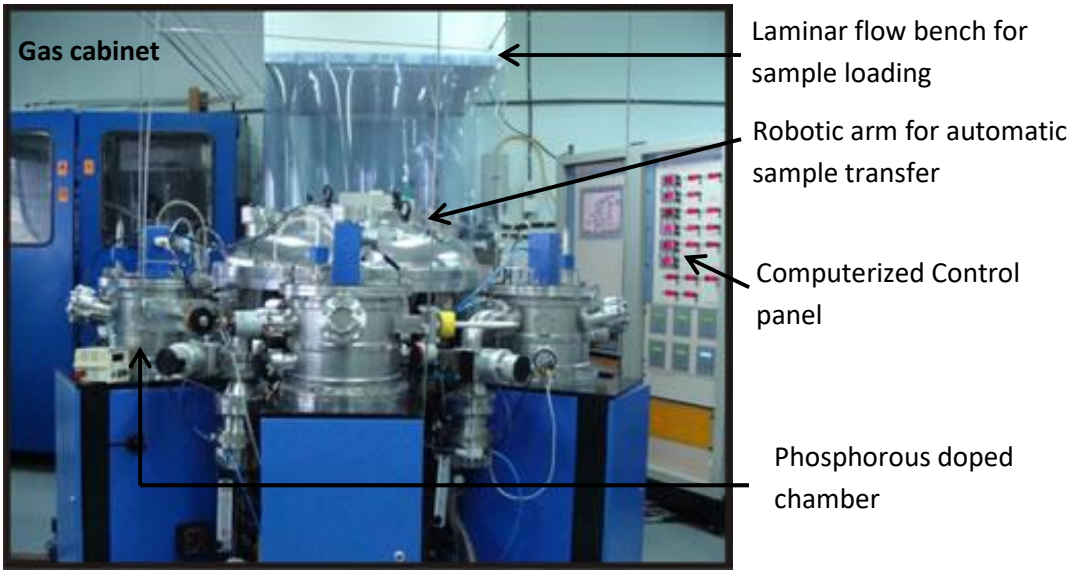

Figure App 5: Image of HWCVD cluster instrument for deposition of microcrystalline silicon film [4].

C. Laser annealing tool

The infrared continuous wave laser doping tool was designed by Scantech laser and the laser source is designed by SPI laser established in National centre of photovoltaic research and education (NCPRE), Indian Institute of Technology Bombay, Mumbai, India [5].

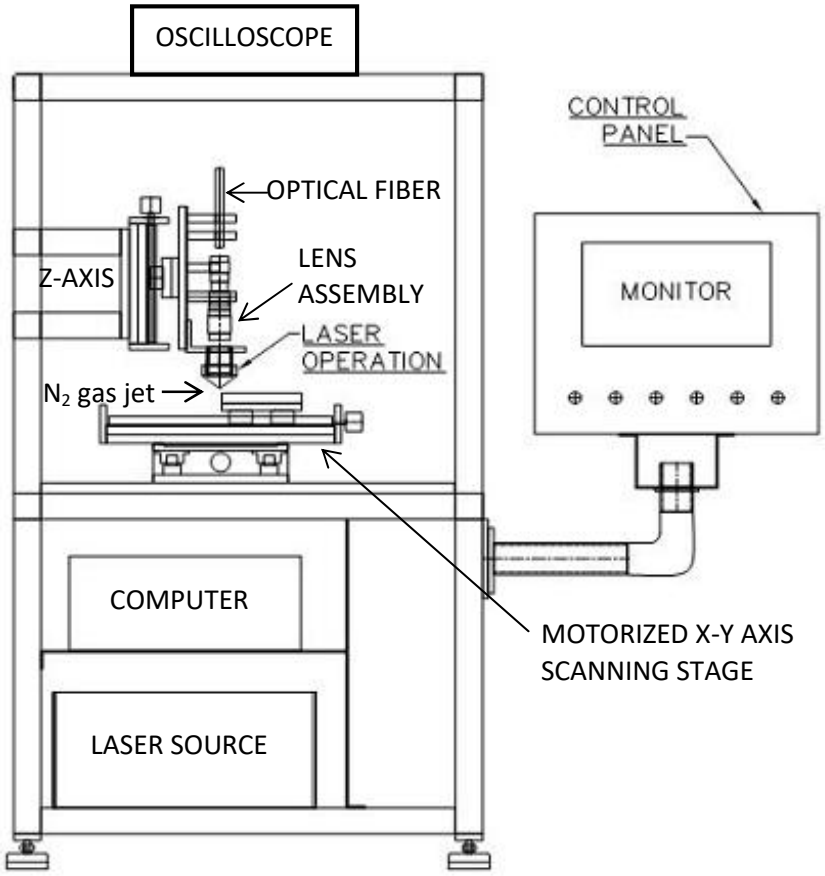

Figure App. 6: Block diagram of infrared continuous wave laser tool for annealing of silicon film [5].

Calculation of laser fluence

We have calculated the laser energy density also known as fluence using the following equations. Sample calculation is also given below [6].

$$Energy\ of\ pulse = peak\ power \times pulse\ duration$$

$$= 0.8W \times 10 \times 10^{-6}\ sec$$

$$Laser\ beam\ spot\ diameter = 10\ \mu m$$

$$Area\ of\ laser\ expose = \pi r^2 = 3.14 \times \left(\frac{10}{2}\right)^2\ \mu m^2 = 78.5 \times 10^{-8}\ cm^2$$

$$Fluence = \frac{Energy\ of\ pulse}{\pi r^2}$$

$$Fluence = \frac{0.8W \times 10 \times 10^{-6}\ sec}{78.5 \times 10^{-8}\ cm^2} = 10.19\ Jcm^{-2}$$

Appendix II Sample preparation

The cleaning and etchant chemical handled under fume hood following the safety and contamination protocols abide by the CEN facility, IITB, Mumbai, India [7].

A. Wafer Cleaning

Contaminants present on the surface of silicon wafers at the start of processing, or accumulated during processing, have to be removed at specific processing steps in order to obtain high performance and high reliability semiconductor devices, and to prevent contamination of process equipment, especially the high temperature oxidation, diffusion, and deposition tubes. The RCA clean is the industry standard for removing contaminants from wafers. Werner Kern developed the basic procedure in 1965 while working for Radio Corporation of America (RCA) [8].

The RCA cleaning procedure has three major steps used sequentially i) Organic Cleaning (removal of insoluble organic contaminants). ii) Oxide Striping (removal of a thin silicon dioxide layer where metallic contaminants may accumulate). iii) Ionic Cleaning (removal of ionic and heavy metal atomic contaminants).

The detail processes are explained as follows.

Organic cleaning (RCA 1)

Step 1: HF soak

192 ml DIW + 8ml HF 49% (30 sec)

Step 2: KOH soak

182ml DIW + 25ml KOH + 50ml H_2O_2 (Heated at 70°C for 12 min)

Step 3: Repeat step '1'

Ionic cleaning (RCA 2)

Step 4: HCl soak

182ml DIW + 25ml HCl + 50ml H_2O_2 (Heated at 70°C for 12 min)

Step 5: Repeat step '1' then dry with 5N purity nitrogen blow inside laminar flow bench.

B. Mask plate cleaning

Stainless steel mask plates were cleaned before putting into the HWCVD reaction chamber during device fabrication.

Step 1: Dip mask plates in 50 ml TCE to be heated at 70°C for 10 min.

Step 2: Dip acetone, ultrasonicate for 10 min.

Step 3: Dip isopropyl alcohol ultrasonicate for 10 min.

Step 4: Rinse with de ionized water

Step 5: Dry with N_2.

C. Substrate preparation

i) Si/SiO_2

For SiO_2, we used n-type two inch Silicon wafer (Resistivity 1-5 ohm-cm, Thickness 275 micron). We performed RCA cleaning of the wafer followed by depositing 500 nm of silicon dioxide in wet oxidation furnace at 1050°C for 55 min. We have used 15 lit/min N_2 flow to keep positive pressure inside the furnace. Wet oxidation was performed under 100 lit/min O_2 and 70 lit/min H_2 gas flow. Thickness measurement was performed using optical reflactometer.

ii) Glass

We have used alkali free borosilicate glass as a substrate for synthesis of phosphorous doped intrinsic poly crystalline silicon film. These glass pieces were one millimetre thick. We performed a 5 sec dip in 2% hydrofluoric acid (HF) (192 ml DIW + 8 ml 48%HF) as a cleaning procedure.

iii) Glass/FTO

We also have used patterned Fluorine tin oxide (FTO) coated glass to have a bottom contact. For pattern FTO we have used a polyimide tape to cover a portion of FTO so that this part is protected during etching process. The rest of the FTO coated glass substrate was covered with a thin layer of zinc powder. By adding some drops of 2M hydrochloric acid (HCl) solution, the FTO-layer was completely removed. The sheet resistance after the HCl treatment increased to larger than 1 MΩ/□.

After pattern, we performed boiling of sample at 70°C in trichloroethylene (TCE) followed by dip in acetone and dip in isopropyl alcohol (IPA) for ten minute with ultrasonic bath.

For cleaning of all the substrates before putting into the reaction chamber we blow 99.999% pure N_2 gas in the laminar flow bench.

D. TMAH etching

Tetra methyl ammonium hydroxide (TMAH) etching performed under fume hood to remove one micron silicon film from FTO coated glass substrate. 30 ml of TMAH were taken in a glass Petri dish and heated on a temperature controlled hot plate at 90°C for 15 minutes. Using a suitable clamp we dip 2 mm of the sample into the solution for 2 minutes. Then dip in de ionized water (DIW) and dried using N_2. Resistance of exposed FTO after etching measured using ohm meter and compared with the resistance of a standard FTO coated on glass substrate. Standard resistance measured for FTO is 30 ohm placing two probes at 1 cm apart, and after etching exposed FTO resistance was 27 ohm. The variation comes from probe contacts and separation.

E. X-TEM sample preparation

We have used intrinsic silicon film grown on Si/SiO_2 substrate to prepare sample for cross section transmission electron microscope (X-TEM) imaging. The sample prepared for X-TEM imaging was performed using a route explained in brief [9,10,11].

Step 1 Deposition of 20 nm Chromium followed by 80 nm gold using thermal evaporator.

Step 2 Cut 4 mm $\times$ 4 mm two pieces of sample using ultrasonic cutter.

Step 3 Stake two pieces of samples facing towards each other. Add two more pieces of silicon wafer of same size on both side of this structure. All the samples were added using epoxy (glue).

Step 4 Cut 2.3 mm diameter and 5mm long cylinder using ultrasonic cutter. Put the cylinder into a brass tube.

Step 5 Fix the cylinder into the holder of a disk cutter and cut 700 microns thick 6 to 7 disks.

Step 6 Using manual grinder and lapping paper (45 microns for lapping and 5 micron for polishing) reduce the thickness of the disk to 100 micrometer.

Step 7 Place this 100 micron thick disk in a dimpling instrument so it makes a dimple around 70 microns depth at the middle of the disk. This dimpled part of the sample became 30 microns thick.

Step 8 The last step of the sample preparation is performed in a precision ion polishing system (PIPS) where the sample is being bombarded by Argon ion with an energy of 5 kV. The ion expose duration to achieve the required thinning depends on the sample material. One can thin the sample as thin as 100 nm which allows electron to pass through the sample for X-TEM imaging.

Appendix III Characterization tool

In this section we have presented the images of several characterization tools those were used in our study.

A. Stylus surface profiler

Stylus surface profiler was used for the measurement of thickness of silicon film. The both instrument is established in Center of Excellence in Nano Technology, Indian Institute of Technology Bombay, Mumbai, India [12].

Figure App 7: Image of Ambios stylus surface profiler for thickness measurement of silicon film.

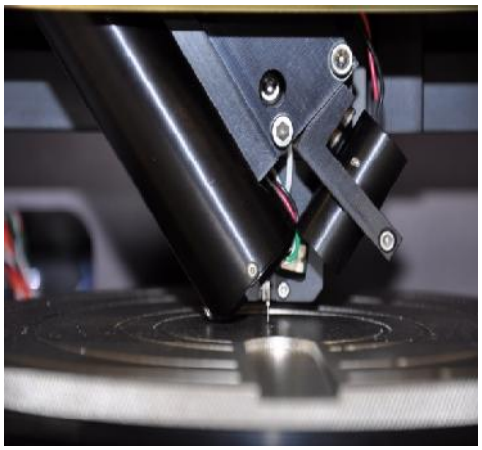

Figure App 8: Image of stylus tip arrangement of Ambios stylus surface profiler.

Figure App 9: Image of DektakXT stylus surface profiler for thickness measurement of silicon film [13].

B. Optical reflectance

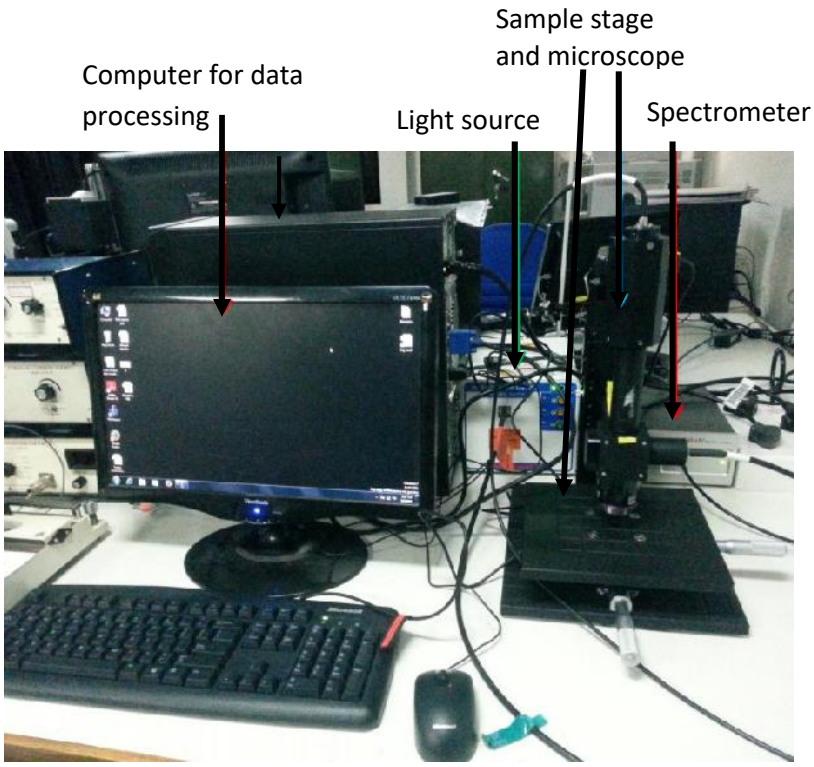

Figure App 10: Image of optical Reflectometer for thickness measurement of silicon dioxide on silicon wafer [12].

Optical Reflectometer was used for the measurement of thickness of silicon dioxide film on silicon wafer. The instrument is established in Centre of Excellence in Nano Technology, Indian Institute of Technology Bombay, Mumbai, India [12].

C. Atomic Force Microscopy (AFM)

Atomic Force Microscope (AFM) was used to observe the nucleation size, shape and density in the early stage of growth of silicon film. The instrument allows us to do surface imaging of silicon film up to nano meter accuracy. The instrument is established in Centre of Excellence in Nano Technology, Indian Institute of Technology Bombay, Mumbai, India [12].

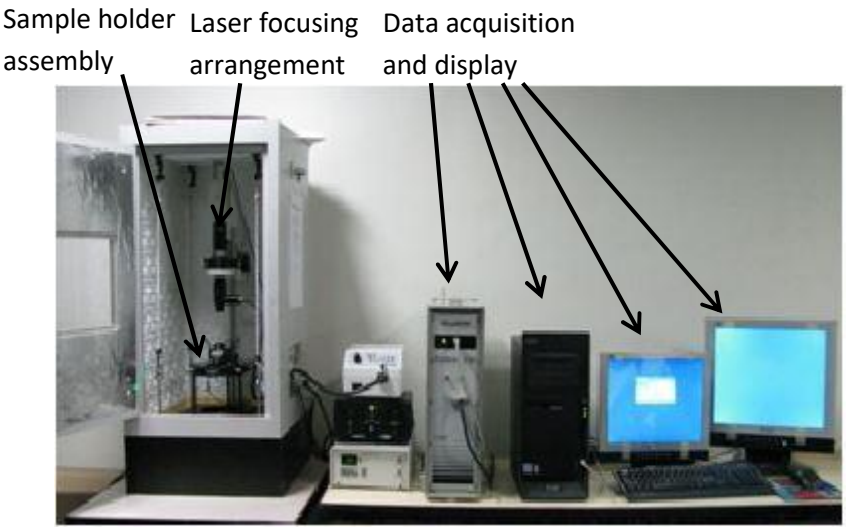

Figure App 11: Image of atomic force microscope for the measurement nucleation density of silicon thin film [12].

D. 3D optical microscope

In our study we have used 3D optical microscope for imaging laser irradiated n-type silicon film on glass substrate. The roughness and surface profiling was performed from image analysis. In this case we have used Zeta 3D microscope from Zeta instrument [14]. The instrument is established in National Centre of Photovoltaic Research and Education, Indian Institute of Technology Bombay, Mumbai, India [15].

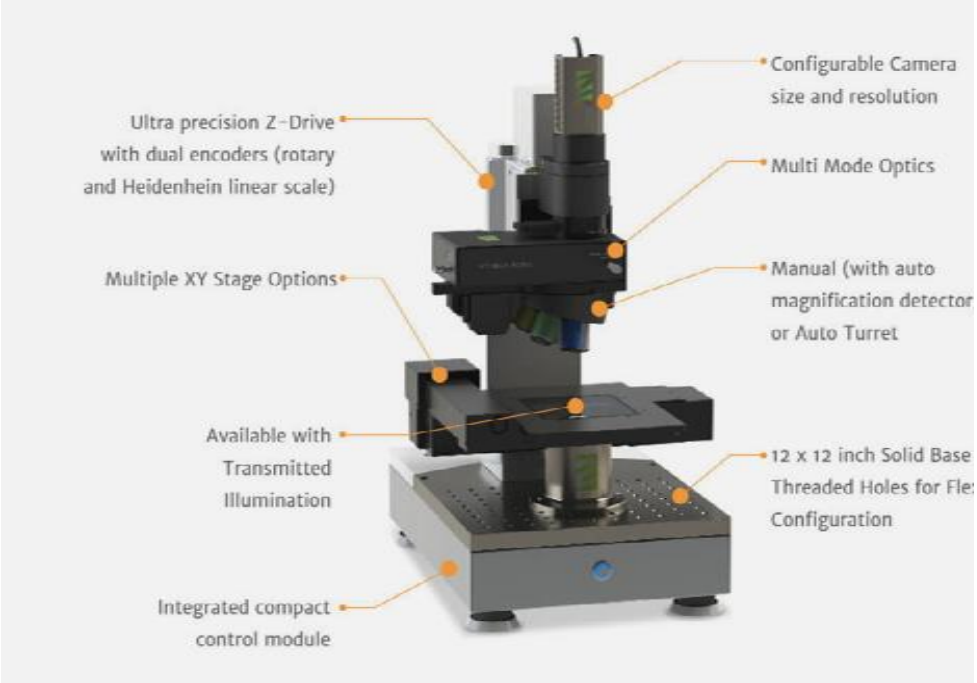

Figure App 12: Image of Zeta 3D optical microscope for the measurement of the roughness of silicon film on glass substrate after laser irradiation [14]

E. 2D optical microscope

Figure App 13: Image of 2D MX61-F Olympus optical microscope [12]

We have used MX61-F Olympus microscope for optical imaging as a primary tool for viewing surface morphology of hot wire CVD grown film as well as laser irradiated film. Also outline of devices after masking was well observed. Formation of cracks due to high tensile stress was also visible under this microscope. The instrument is established in Centre of Excellence in Nano Technology, Indian Institute of Technology Bombay, Mumbai, India [12].

F. SEM & EDS Tool

Topographical observation of silicon film was taken out using Field Emission Gun Scanning Electron Microscope (FEGSEM) from Zeiss Ultra 55 FE-SEM with Oxford EDX system. The instrument is established in National Centre of Photovoltaic Research and Education, Indian Institute of Technology Bombay, Mumbai, India [15].

Figure App 14: Image of scanning electron microscope with oxford energy dispersive x-ray (EDS) unit [15].

G. Raman spectrometer

In our study for evaluation of crystallinity of silicon film, we have used Raman spectrometer from Horiba Scientific [16]. The instrument is established in the Centre for Research in Nanotechnology & Science (CRNTS), Indian Institute of Technology Bombay, Mumbai, India [17].

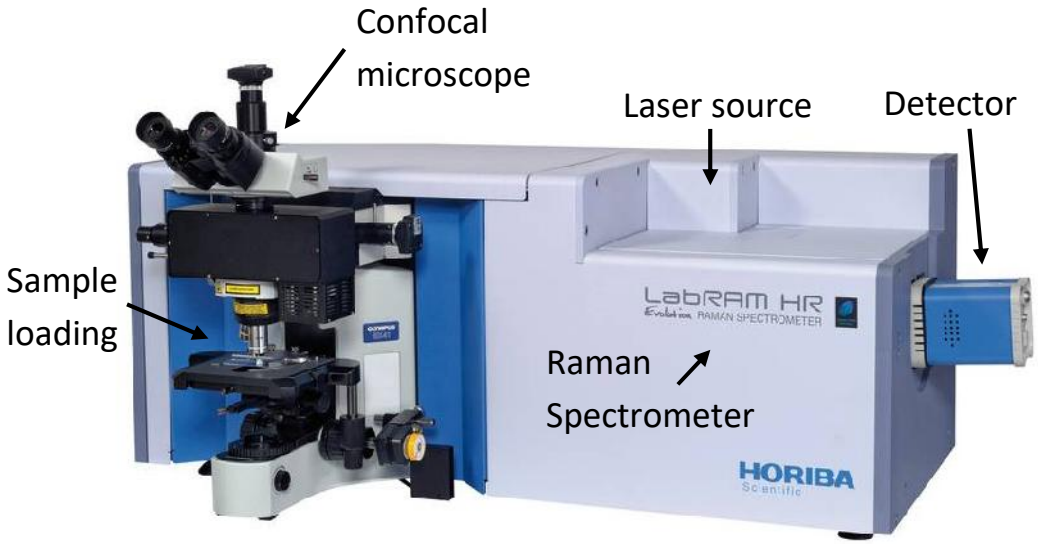

Figure App 15: Image of confocal Raman spectrometer [16]

H. FTIR

Figure App 16: Image of Furrier transform infrared spectrum tool [12].

FTIR imaging was performed using Perkin Elmer spectrum BX-II spectrometer. The instrument is established in Centre of Excellence in Nano Technology, Indian Institute of Technology Bombay, Mumbai, India [12].

I. TOF-SIMS

In our study we have used PHI nano TOF II time of flight secondary ion mass spectrometry (TOF-SIMS) for measurement of phosphorous and boron concentration in silicon film. The instrument is established in Sophisticated Analytical Instrument Facility (SAIF), Indian Institute of Technology Bombay, Mumbai, India [18].

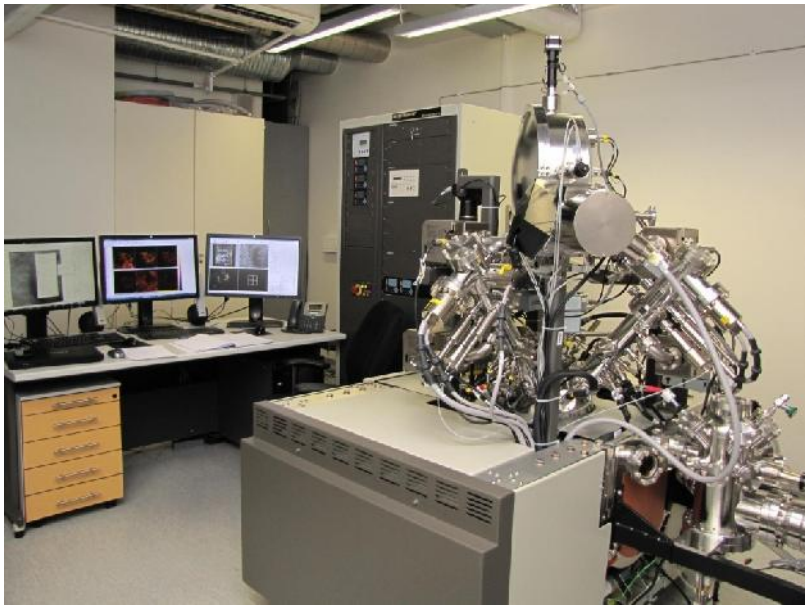

Figure App 17: Image of Time of flight secondary ion mass spectrometry tool [18]

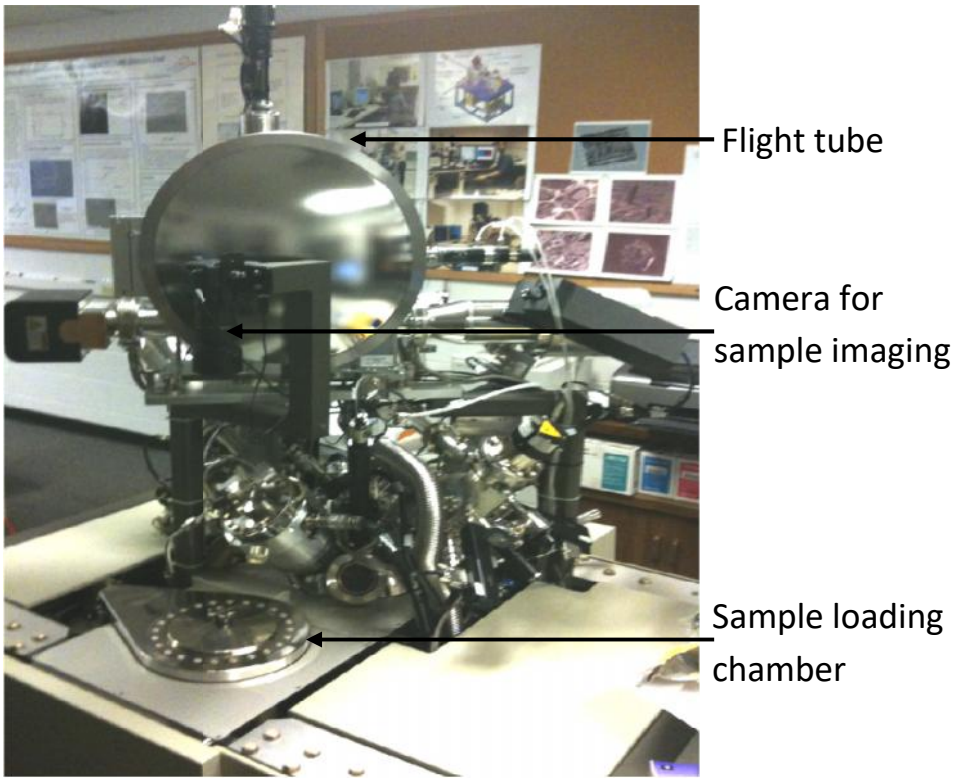

Figure App 18: Image of Time of flight secondary ion mass spectrometry tool [18]

J. UV-VIS-NIR spectrum

In our study we have used a spectrometer from Bentham PVE300 for measuring the reflectance and transmittance of silicon film. The instrument is established in National Centre of Photovoltaic Research and Education, Indian Institute of Technology Bombay, Mumbai, India.

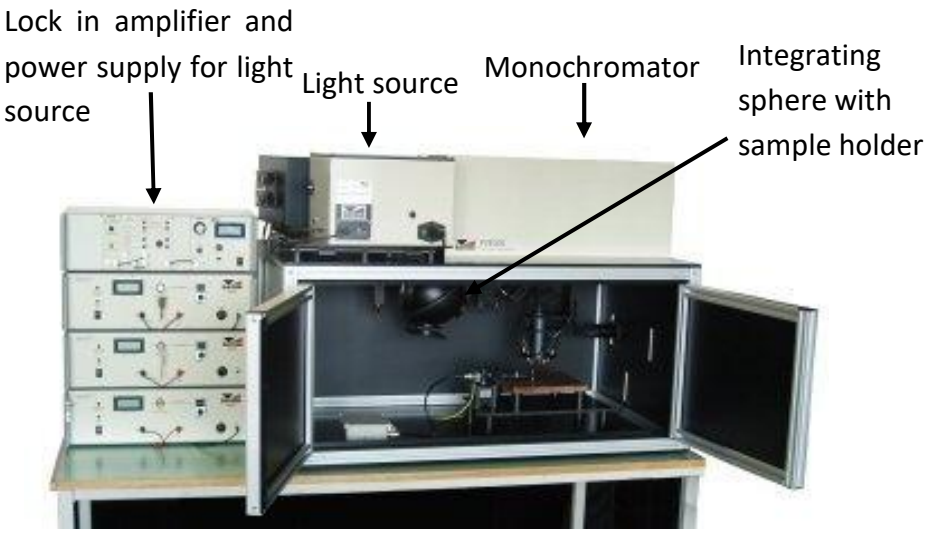

Figure App 19: Image of Bentham PVE300 UV-VIS-NIR spectrometer [15]

K. Four probe instrument

In this study we have used four point probes by Lucas-Signatone to calculate sheet and bulk resistivity of the intrinsic, phosphorous and boron doped silicon film. The instrument is established in National Centre of Photovoltaic Research and Education, Indian Institute of Technology Bombay, Mumbai, India [15].

Figure App 20: Image of Sun four point probe instrument for sheet resistivity measurement [15].

References

[1] Nitin S. Kale, S. Pai, R.Pinto, V. Ramgopal Rao,"Design and Development of Hotwire CVD cluster system for bioMEMS and polymer electronics applications", communicated to The Journal of Vacuum in April, 2007.

[2] Nitin S. Kale, PhD thesis, "Making HWCVD a viable technology alternative for BioMEMS application", Indian Institute of Technology Bombay, Mumbai, India, 2007.

[3] R. O. Dusane, Opportunities for new materials synthesis by hot wire chemical vapor process , Thin Solid Films , vol. 519, no. 14, pp. 4555-4560, 2011, (doi: 10.1016/j.tsf.2011.01.315).

[4] www.met.iitb.ac.in /main. Html ?s= y&sec = research & content = facilities / labs

[5] http://www.ncpre.iitb.ac.in/equipments/eqp/Laser_doping_tool.php

[6] www. ophiropt.com / laser – measurement – instruments / beam- profilers/ knowledge - center/ tutorial- slit- based- profilers / measuring- pulsed- beams

[7] www.cen.iitb.ac.in/cen/index.php

[8] W. Kern and J. Vossen, Eds., Thin Film, Academic Press New York, Ch V-1, 1978.

[9] Transmission Electron Microscopy, A textbook for materials science D.B. Williams, C.B. Carter Plenum Press New York, 1996.

[10] Specimen Preparation for Transmission Electron Microscopy of Materials Microscopy Handbook 03 P.J.Goodhew Oxford University Press, Royal Microscopical Society, 1984

[11] Sample Preparation Handbook for Transmission Electron Microscopy J. Ayache, L. Beaunier , J. Boumendil, G. Ehret, D. Laub Springer, 2010.

[12] www.cen.iitb.ac.in/cen/online_modules/equipmentslist.php

[13] www.bruker.com/products/ surface- analysis/ stylus- profilometry

[14] www.zeta-inst.com/products/true-color-3D-optical-profiler

[15] www.ncpre.iitb.ac.in/equipments/facilities.html

[16] www.horiba.com/ scientific/ products /raman- spectroscopy/ raman- spectrometers / raman- microscopes /hr-evolution /labram-hr-evolution-17309/

[17] www1.iitb.ac.in/~crnts

[18] www.rsic.iitb.ac.in/SIMS.html